DIPLOMARBEIT

Dynamic Simulations of Rolling Element Bearing Cages

ausgeführt zum Zwecke der Erlangung des akademischen Grades eines Diplom-Ingenieurs

unter der Anleitung von

O.Univ.Prof. Dipl.-Ing. Dr.techn. Franz G. Rammerstorfer
Institut für Leichtbau und Struktur-Biomechanik

eingereicht an der Technischen Universität Wien

Fakultät für Maschinenwesen und Betriebswissenschaft

von

Andreas W. Nemetz
Matr.Nr. e0527746
Jheringgasse 14
1150 WIEN

Wien, 24. Jänner 2016

Contents

List of Figures III

List of Tables VI

1 Rolling Bearings 4
- 1.1 Terminology [2],[4] . . . 5
- 1.2 Construction types [2],[4] . . . 6
- 1.3 Cage [2],[4] . . . 7
- 1.4 Angular Contact Ball Bearing [2],[4] . . . 11
- 1.5 Cylindrical Roller Bearings [2],[4] . . . 13
- 1.6 Friction and Lubrication [2],[4] . . . 15
  - 1.6.1 Grease . . . 15
  - 1.6.2 Oil . . . 15

2 BEAST - BEAring Simulation Tool 17

3 ACBB - High Speed Test 19
- 3.1 Analytical Calculations [2],[11] . . . 20
  - 3.1.1 Kinematics of the Angular Contact Ball Bearing . . . 20
- 3.2 Virtual Test [3],[10] . . . 23
  - 3.2.1 Model building . . . 23
  - 3.2.2 Material Parameters . . . 24
  - 3.2.3 Mesh Parameters . . . 25
  - 3.2.4 Model reduction . . . 26
  - 3.2.5 Tribology . . . 27
  - 3.2.6 Boundary conditions . . . 27
  - 3.2.7 Time and Output . . . 30
  - 3.2.8 Solver settings . . . 31
  - 3.2.9 Results of the simulation . . . 32
  - 3.2.10 Kinematics of the bearing . . . 33
  - 3.2.11 Load distribution and contact forces . . . 41
  - 3.2.12 Contact pressure . . . 43
  - 3.2.13 Structural stresses . . . 44
  - 3.2.14 Deformation . . . 50
  - 3.2.15 Frictional moment . . . 51
  - 3.2.16 Modal analysis . . . 52

4 Structural Fatigue 54
- 4.1 Uniaxial fatigue criterion [3] . . . 56
- 4.2 Stress life curve [12] . . . 57

4.3 BEAST structural fatigue damage and life assessment 58

5 ACBB - Dynamic Cage Robustness Test 67
5.1 Virtual Test [3],[10] 68
5.1.1 Model building 68
5.1.2 Material parameters 68
5.1.3 Mesh parameters 68
5.1.4 Model reduction 70
5.1.5 Tribology 70
5.1.6 Boundary conditions 70
5.1.7 Time and Output 72
5.1.8 Solver settings 73
5.1.9 Results of the simulation 73
5.1.10 Kinematics of the bearing 74
5.1.11 Load distribution and contact forces 80
5.1.12 Contact pressure 85
5.1.13 Structural stresses 86
5.2 Structural fatigue 92

6 CRB - Investigation of a CRB under deceleration 94
6.1 Virtual Test [3] 94
6.1.1 Model building 94
6.1.2 Material parameters 95
6.1.3 Tribology 95
6.1.4 Boundary conditions 95
6.1.5 Solver settings 97
6.1.6 Results of the simulation 97
6.1.7 Kinematics of the bearing 98
6.1.8 Contact forces 101
6.1.9 Contact pressure 102

7 Conclusion 104

References VII

List of Figures

1 Bearing Terminology [2] . . . 5
2 Stamped metal cages [2] . . . 8
3 Machined metal cages [2] . . . 8
4 Polymer cages [2] . . . 9
5 Cage guidance [2] . . . 9
6 Single Row Angular Contact Ball Bearing [2] . . . 11
7 Paired mounting of ACBBs [2] . . . 12
8 Standard SKF ACBB cages [2] . . . 12
9 Single Row Cylindrical Roller Bearing (NU design) [2] . . . 13
10 SKF basic designs of Single Row Cylindrical Roller Bearings [2] . . . 14
11 Methods of oil lubrication [2] . . . 15
12 BEAST toolbox [3],[5] . . . 18
13 Cross-section of the testing arrangement . . . 19
14 Simple model of the ACBB . . . 20
15 Exploded View of the ACBB BEAST-model . . . 23
16 Global and refined mesh . . . 26
17 Local coordinate systems of the cage pocket segments . . . 27
18 Schematic presentation of a connection between bodies or coordinate systems [3] . . . 28
19 Start-up phase realized with ramp function . . . 31
20 Assembled Angular Contact Ball Bearing relative to global coordinate system . . . 32
21 Movement of the outer ring . . . 33
22 Amplitude spectra of the movement of the outer ring . . . 34
23 Translational velocity of the center of the outer ring . . . 35
24 Movement of the cage . . . 36
25 Translational velocity of the center of the cage . . . 36
26 Amplitude spectra of the velocity of the center of the cage . . . 37
27 Angular velocity of the cage for case A . . . 38
28 Movement of the cages center of mass for case A . . . 39
29 Velocity of the center of the ball 1 . . . 40
30 Relative kinematics of the cage vs. the balls . . . 40
31 Load distribution for case A . . . 41
32 Contact forces for case A . . . 42
33 Dynamic situation of the bearing elements ball 1 and cage . . . 43
34 Maximum value of contact pressure due to Hertzian contact in the cage pocket . . . 43
35 Contact area in the cage pocket . . . 44
36 v. Mises stresses of the cage for different angular positions . . . 45
37 Cage segment with maximum v. Mises stress . . . 46

38 Arrangement of the used flexible coordinate systems in the cage pockets . 47
39 Flexible coordinate systems at the front side of the cage pocket and dedicated v. Mises stresses 48
40 Flexible coordinate systems at the back side of the cage pocket and dedicated v. Mises stresses 49
41 Deformations of the cage for case A 50
42 Cage segment with maximum deformation 51
43 Power loss during simulation time 52
44 Calculated deformation modes of the lowest six eigen frequencies 52
45 Simplified S-N curve constructed for the cage material [12] 57
46 Location of the influence radii with fatigue calculation activated 59
47 Main results of the structural fatigue calculation for the influence radius 2 60
48 Main results for surface roughness 3,75 μm and residual stress 150 MPa in the cage pockets 61
49 Main results for surface roughness 3.75 μm and residual stress 100 MPa in the cage pockets 62
50 Main results for surface roughness 2.5 μm and residual stress 150 MPa in the cage pockets 62
51 Main results for surface roughness 2.5 μm and residual stress 100 MPa in the cage pockets 63
52 Main results for surface roughness 2.5 μm and residual stress 50 MPa in the cage pockets 63
53 Main results for surface roughness 1.25 μm and residual stress 150 MPa in the cage pockets 64
54 Main results for surface roughness 1.25 μm and residual stress 100 MPa in the cage pockets 64
55 Main results for surface roughness 1.25 μm and residual stress 50 MPa in the cage pockets 65
56 Influence of the residual stress and the surface roughness 66
57 Cross-section of the testing arrangement [13] 67
58 BEAST model with and without outer ring 68
59 Meshed cages 69
60 Arrangement of the flexible coordinate systems used for refinement . . . 69
61 Movement of the outer ring 74
62 Amplitude spectrum of the movement of the outer ring 75
63 Translational velocity of the center of the outer ring 76
64 Amplitude spectrum of the velocity of the outer ring 76
65 Circumferential speed of the cages 77
66 Rotation of the cages around the global y-axis 78
67 Velocity of the center of ball 1 in the loaded bearing 78
68 Relative kinematics of the cage vs. the balls in the loaded bearing 79
69 Velocity of the center of ball 1 in the unloaded bearing 79

70 Relative kinematics of the cage vs. the balls in the unloaded bearing . . . 80
71 Load distribution in the loaded bearing . . . 81
72 Load distribution in the unloaded bearing . . . 82
73 Contact forces in the loaded bearing . . . 83
74 Contact forces in the unloaded bearing . . . 84
75 Dynamic situation for the bearing elements ball 1 and cage in the loaded bearing . . . 84
76 Dynamic situation for the bearing elements ball 1 and cage in the unloaded bearing . . . 85
77 Maximum value of contact pressure due to Hertzian contact in the cage pocket in the loaded bearing . . . 85
78 Maximum value of contact pressure due to Hertzian contact in the cage pocket in the unloaded bearing . . . 86
79 Flexible coordinate systems at the front side of the cage pocket and dedicated v. Mises stresses for the loaded bearing . . . 87
80 Flexible coordinate systems at the back side of the cage pocket and dedicated v. Mises stresses for the loaded bearing . . . 88
81 Flexible coordinate systems at the front side of the cage pocket and dedicated v. Mises stresses for the unloaded bearing . . . 90
82 Flexible coordinate systems at the back side of the cage pocket and dedicated v. Mises stresses for the unloaded bearing . . . 91
83 Location of the influence radii with fatigue calculation activated (cage in random position - not the position with extreme stresses) . . . 92
84 Calculated Maximum Damage Factors in the influence radii of the loaded bearing . . . 92
85 Calculated Maximum Damage Factors in the influence radii of the unloaded bearing . . . 93
86 BEAST model of the NU226ECM and the simplified cage . . . 94
87 Rotational velocity of the inner ring . . . 97
88 Movement of the geometric center of the inner ring . . . 98
89 Movement of the geometric center of the cage . . . 99
90 Rotational speed of the cage . . . 100
91 Velocity of the rolling element(s) and velocity of the cage . . . 101
92 Components of the contact forces in the global coordinate system . . . 101
93 Magnitude of the contact forces in the global coordinate system . . . 102
94 Maximum value of contact pressure due to Hertzian contact in the cage pocket . . . 103

List of Tables

1 Bearing Terminology [2] 5
2 Parameters of the Angular Contact Ball Bearing 7313 [2] 22
3 Calculated values of the Angular Contact Ball Bearing 7313 22
4 Material Parameters used in BEAST 24
5 Lubricant Parameters used in BEAST 25
6 Operation conditions for the simulation 32
7 Calculated critical operating conditions 53
8 Life time of the cage for different parameters 65
9 Operation conditions for the simulation 73
10 Operation conditions for the simulation 98

Danksagung

Bedanken möchte ich mich bei all jenen, die zur Entstehung dieser Arbeit beigetragen haben.

Im Besonderen möchte ich mich bedanken,

bei meinen Eltern, die mich in jeder Hinsicht unterstützt und mir das Studium ermöglicht haben,

bei meinem Betreuer bei der SKF Österreich AG, Dipl.-Ing. Rudolf Hauleitner, für seine intensive fachliche Unterstützung und Hilfsbereitschaft,

bei dem Leiter des SKF Österreich AG Development Centre in Steyr, Dipl.-Ing. Thomas Forster, der mir die Bearbeitung dieses spannenden Themas anvertraute,

bei meinem Betreuer am Institut für Leichtbau und Struktur-Biomechanik der TU Wien, o.Univ.Prof. Dipl.-Ing. Dr.techn. Franz Rammerstorfer für seine fachlichen Anregungen und Beratungen und

bei meinen Freunden und Geschwistern, die mich stets auf meinem Weg begleitet haben und somit die Studienzeit auf vielfältige Weise bereichert haben.

Abstract

In this work, the results of dynamic simulations of rolling element bearings are presented and discussed. The focus is set on investigating the performance of the cage. Two variants of rolling element bearings are investigated, which are the Single Row Angular Contact Ball Bearing and the Single Row Cylindrical Roller Bearing. Overall, three simulations are included in this documentation with the goal to get information about the cage performance at high rotating speed, increased clearance and/or strong deceleration.

In order to reduce the complexity of this document, only machined brass cages are investigated. The used software is a SKF simulation software for multi-body systems called BEAring Simulation Tool (BEAST). This tool offers the possibility to perform dynamic simulations of multi-body systems with occurring contacts. It is also able to handle flexible bodies and combines multi-body systems with stress calculation.

The main goal of this work is to test the practicability of the software package BEAST. For this reason, also tests performed by the global test centre in Steyr were simulated. A further focus is set on fatigue calculation. The sensitivity of the results with respect to parameters, like surface roughness and residual stress due to manufacturing, are investigated.

The main conclusion of this diploma thesis is, that the used software tool BEAST is useful for supplementing real tests and to get an idea of the occurring forces within the bearing and the life time of the cage in the investigated case.

Kurzfassung

In dieser Diplomarbeit werden die Ergebnisse dynamischer Simulationen von Wälzlagern betrachtet und diskutiert. Es wurden dazu zwei verschiedene Bauarten von Wälzlagern betrachtet. Diese sind das einreihige Schrägkugellager und das einreihige Zylinderrollenlager. Insgesamt beinhaltet diese Arbeit drei verschiedene Simulationen mit dem Ziel, Informationen über das Verhalten des Käfigs bei verschiedenen Betriebsbedingungen, wie hohe Drehzahlen, erhöhte axiale Lagerluft und/oder starke Verzögerung zu erhalten.

Zur Sicherstellung einer angemessenen Übersichtlichkeit bzw. eines angemessenen Umfangs der Arbeit wurden nur Messing-Käfige betrachtet. Die verwendete Software ist eine von SKF entwickelte Mehrkörpersimulationssoftware mit dem Namen `BEAST`. Diese Software ist konzipiert, Mehrkörperprobleme mit auftretenden Kontakten zu behandeln. Sie ist außerdem in der Lage, flexible Körper in das Modell zu integrieren und kombiniert so die Mehrkörpersimulation mit Spannungsberechnungen.

Das Hauptziel dieser Diplomarbeit besteht darin, die verwendete Software `BEAST` auf ihre praktische Anwendbarkeit zu testen. Deshalb wurden bewusst Betriebsbedingungen gewählt, die bereits auf Versuchsanordnungen getestet wurden. Ein weiterer Fokus lag bei der Schädigungsrechnung und darin, wie verschiedene Parameter, zum Beispiel die Oberflächenrauhigkeit oder Eigenspannungen, das Ergebnis beeinflussen.

Die wesentliche Schlussfolgerung, die aus dieser Arbeit gezogen werden kann, ist die Erkenntnis, dass die Software `BEAST` ein gutes Instrument ist, um Tests, die an Prüfständen gemacht wurden, zu ergänzen und Kräfte, die im Inneren des Lagers auftreten, zu quantifizieren. Sie ist ebenfalls in der Lage, Anhaltspunkte über die Lebensdauer des Käfigs für die entsprechenden Betriebsbedingungen zu geben.

1 Rolling Bearings

Rolling element bearings are standard machine elements which are available for nearly every usual application. Costumers can choose the suitable bearing by knowing the occurring loads and speeds and the available space. There are also analytical calculation tools available, such as the ISO 281 [1] or the SKF rating life [2] to pre-calculate the life time of a bearing used for standard applications. However, in some cases special solutions for bearing are required. In this case, an analytical calculation tool is reaching its limits. To pre-estimate the life time and behaviour of the bearing used in such special applications, more powerful calculation tools are necessary. The multi-body simulation program BEAST [3], developed by SKF is such a tool and therefore used to investigate rolling bearings in a virtual way.

1.1 Terminology [2],[4]

This section gives a short introduction in the terminology for rolling bearings used in this work. In Figure 1 and Table 1 all relevant components are described.

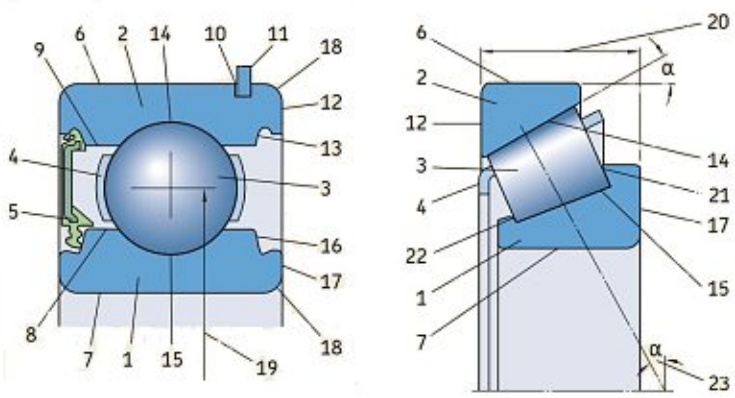

Figure 1: Bearing Terminology [2]

1	Inner ring	13	Recess for capping device
2	Outer ring	14	Outer ring raceway
3	Rolling element	15	Inner ring raceway
4	Cage	16	Recess for capping device
5	Capping device	17	Inner ring side face
6	Outer ring outside surface	18	Chamfer
7	Inner ring bore	19	Bearing pitch circle diameter
8	Inner ring shoulder surface	20	Total bearing width
9	Outer ring shoulder surface	21	Guide flange
10	Snap ring groove	22	Retaining flange
11	Snap ring	23	Contact angle
12	Outer ring side face		

Table 1: Bearing Terminology [2]

1.2 Construction types [2],[4]

To be able to handle the huge variation of operating conditions, developers designed various construction types of rolling bearings. There are different aspects to classify the different types. Possible differentiators are:

- Geometry of the used rolling elements
- Direction of the forces that can be taken up.

In general a rolling bearing consists of rolling elements, rings, the cage and the lubrication. All of this elements are briefly described in the following passages. Because of the focus on cages in this work, this element will be described in detail in the following section 1.3.

Rolling elements are simple geometric bodies such as balls, cylinders or cones. They enable the relative movement and transfer the forces between the inner and the outer ring.

Rings
Depending on the position of the ring, the race - which transfer the forces to the rolling elements - is located in the inner or outer side of the ring.

Lubricant
The lubrication is an important component of a rolling element bearing. Main task of the lubricant is to form a lubricating film to avoid the contact of the surfaces of the race and the rolling element and to reduce friction.

1.3 Cage [2],[4]

Nearly every rolling element bearing is equipped with a cage. Sole exception is the full complement bearing. The principal function of the cage as part of a rolling element bearing is to keep the rolling elements at a proper distance from each other to avoid contact between them and to prescribe the general movement of the rolling elements relative to the rings. Without a cage, the rolling elements would be able to get in contact with each other. The relative velocity in the contact zone would be two times the relative circumferential speed of a single rolling element and the friction would cause high temperatures, wear and damage. Keeping the rolling elements evenly spaced also optimises the load distribution and enables quiet and uniform operation. On the other hand, the velocity of a rolling element depends on the position within the bearing. In the loaded zone the velocity of the rolling element is determined by the relative movement of the rings and in the unloaded zone it mostly depends on the forces caused by contact between the rolling element and the cage and also gravity forces or forces of inertia. This means that the cage and the rolling elements are driven alternating by each other. Cages are mechanically stressed by frictional, strain and inertial forces. Certain lubricants or additives can also cause chemical stresses. Therefore, the design and material of a cage has a significant influence on the suitability of a rolling bearing for a particular application. Most of the cages used in practice are made of either metal, brass or polymer. In this work, machined brass cages are investigated.
Metal cages can be classified into the main groups due to the manufacturing process:

- stamped metal cages
- machined metal cages

Stamped metal cages are mostly made of sheet steel, but also sheet brass cages are available. The benefits of this cage type are the lightweight and the provided space inside the bearing to optimize the effects of the lubricant. Figure 2 shows some standard metal sheet cages, which are (from left to right):

- ribbon-type cage
- riveted cage
- snap-type cage
- window-type cage

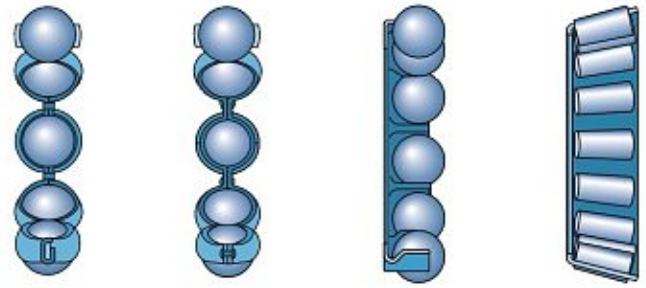

Figure 2: Stamped metal cages [2]

Machined metal cages are available in different designs (Figure 3, from left to right):

- two-piece machined riveted metal cage
- two-piece machined metal cage with integral rivets
- one-piece machined window-type metal cage
- double prong-type machined metal cage

Used materials for machined metal cages are brass, steel or light alloy. This sort of cages permit higher speeds and they are typically used, when forces other than pure rotational forces are superimposed on the cage.

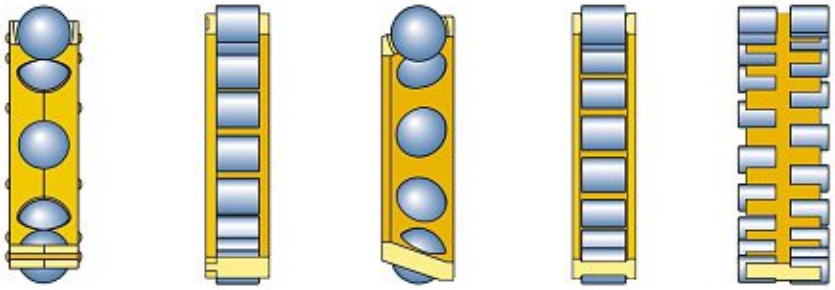

Figure 3: Machined metal cages [2]

Polymer cages are often injection moulded and they are characterized by a favourable combination of strength and weight. Due to the good sliding properties of the polymer on lubricated steel, little friction is produced. Because of this, frictional heat and wear in the bearing are minimized. Low density also minimize the forces of inertia of the

cage. The excellent properties under poor lubrication conditions ensure good emergency running properties. Following standard polymer cages are available (Figure 4, from left to right):

- polymer window-type cage
- polymer snap-type cage

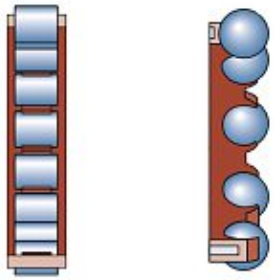

Figure 4: Polymer cages [2]

Cage guidance is absolutely essential to ensure a smooth run of the cage. The guidance can be realized in different ways. The cage can be radially centered on (Figure 5, from left to right):

- the rolling elements
- the inner ring
- the outer ring

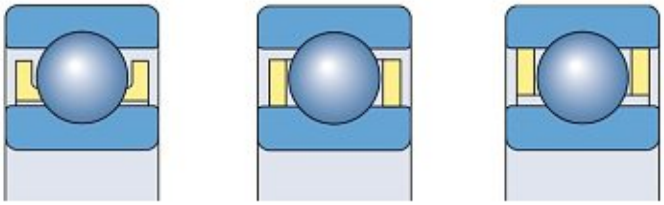

Figure 5: Cage guidance [2]

Stamped metal cages are typically guided by the rolling elements, but machined cages can be produced in any variant.

Rolling element guided cages permit the lubricant to enter the bearing easily.
Ring guided cages provide more precise guidance and are therefore suitable for applications with high speed, frequent and/or rapid accelerations. For this arrangement a sufficient supply of lubricant for the guiding surface has to be assured.

Cage materials

As mentioned before, several materials are used in cage manufacturing. According to the SKF General Catalogue [2], the following cage materials are used in SKF rolling bearings:

- Sheet steel cages are mainly made of continuously hot rolled low carbon steel in accordance with EN10111. In stainless steel bearings, cages made of X5CrNi18-10 are used.
- Sheet brass cages are mainly made of brass in accordance with EN 1652.
- Machined steel cages are normally made of non-alloyed structural S355GT (St52) type steel in accordance with EN 10 025:1990 + A:1993.
- Machined brass cages are made of CW612N or wrought brass in accordance with EN 1652.
- Polymer cages are mostly made of Polyamide 66, Polyamide 46, Polyetheretherketone or Phenolic resin.

1.4 Angular Contact Ball Bearing [2],[4]

Single Row Angular Contact Ball Bearings (ACBB) are designed to accommodate combined loads (Figure 6). The angle between the line joining the points of contact of the ball and the raceways and a line perpendicular to the bearing axis is called contact angle. The carrying capacity for axial loads is increasing with this angle. Because of the geometry, the angular contact ball bearing can accommodate axial loads in one direction only. For this reason it is normally adjusted against a second bearing. If two bearings mounted in random order, but immediately adjacent to each other, they have to be special manufactured to obtain a given internal clearance or preload. Paired mounting (Figure 7) is used when the load carrying capacity of a single bearing is inadequate or when combined axial loads act in both directions.

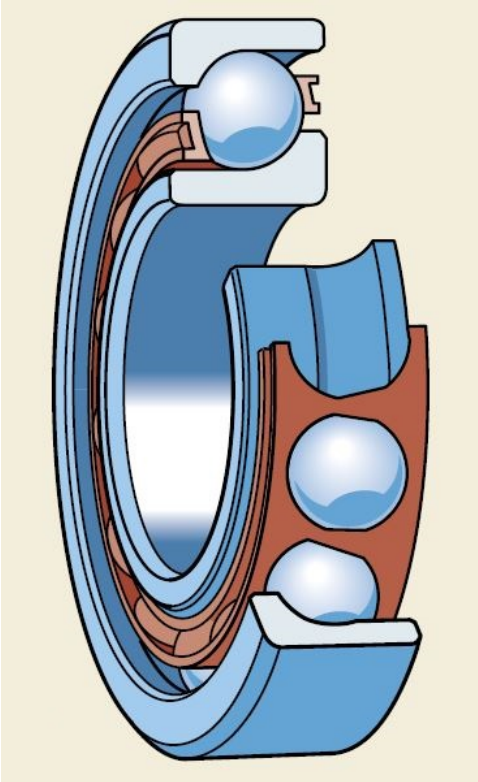

Figure 6: Single Row Angular Contact Ball Bearing [2]

Internal clearance in Single Row Angular Contact Ball Bearings is only obtained after mounting and is depending on adjustment against a second bearing.

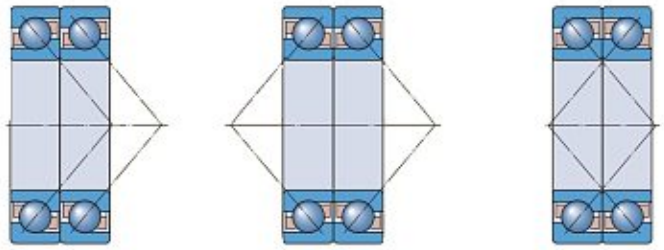

Figure 7: Paired mounting of ACBBs [2]

Standard cages for Angular Contact Ball Bearings manufactured by SKF are (Figure 8):

- injection moulded window-type cage of glass fibre reinforced polyamide 6,6
- injection moulded window-type cage of polyetheretherketone (PEEK)
- pressed window-type brass cage
- machined window-type brass cage

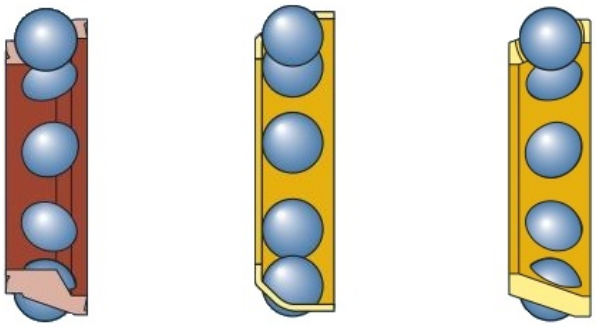

Figure 8: Standard SKF ACBB cages [2]

Additionally to the Single Row Angular Contact Ball Bearing, also Double Row Angular Contact Ball Bearings and Four-Point Contact Ball Bearings are available variants of ACBBs.

1.5 Cylindrical Roller Bearings [2],[4]

Single Row Cylindrical Roller Bearings (Figure 9) are suitable for heavy radial loads. They are available in many designs and the majority is equipped with a cage to reduce loss. Full complement roller bearings are also available to handle very heavy loads in combination with moderate speeds.

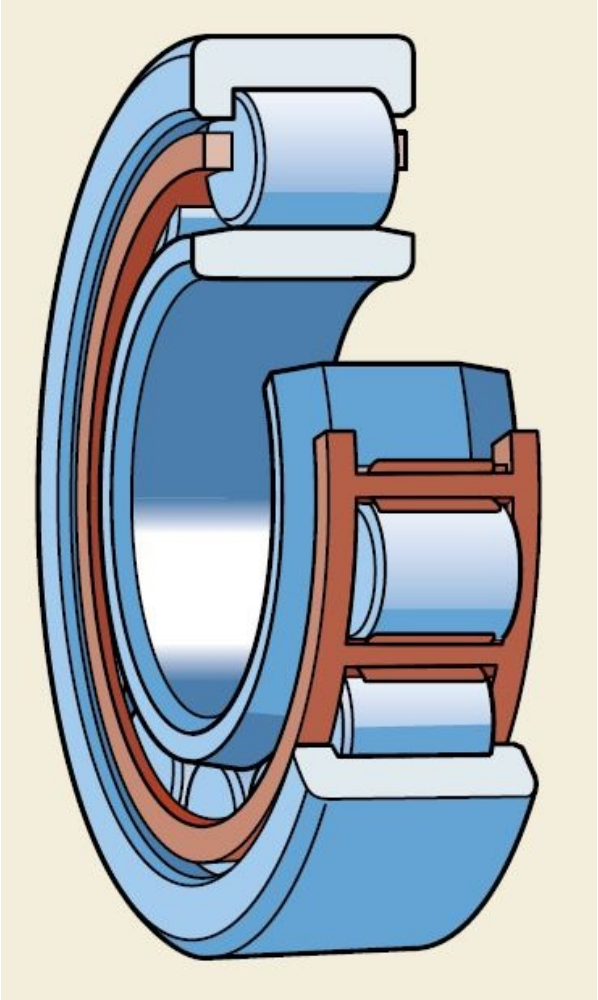

Figure 9: Single Row Cylindrical Roller Bearing (NU design) [2]

Cylindrical Roller Bearings are seperable and the basic bearing design can be classified by the configuration of the flanges in the rings. The main designs are (Figure 10, from left to right):

- NU design

- N design
- NJ design
- NUP design

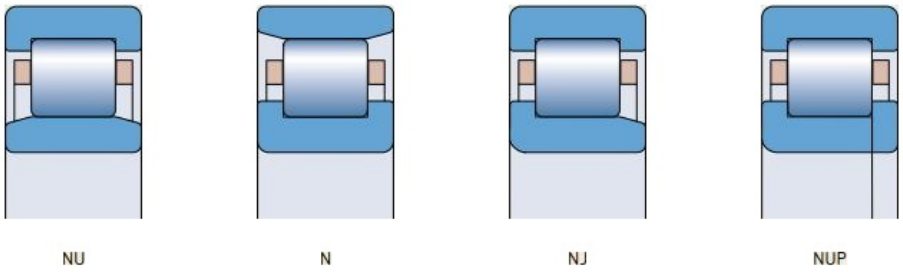

Figure 10: SKF basic designs of Single Row Cylindrical Roller Bearings [2]

NU design roller bearings can accommodate axial displacement because of the two integral flanges on the outer ring and no flanges on the inner ring.

N design roller bearings can accommodate axial displacement because of the two integral flanges on the inner ring and no flanges on the outer ring.

NJ design roller bearings are used to locate the shaft axially in one direction and they are therefore able to accommodate axial displacement in one direction only because of the integral flanges on the outer ring and one flange on the inner ring.

NUP design roller bearings are used to locate the shaft axially in both directions. They are designed with two integral flanges on the outer ring and one integral flange and one non-integral flange on the inner ring.

1.6 Friction and Lubrication [2],[4]

To ensure that the rolling bearing performs reliable, the machine element must be adequately lubricated. The main function of the lubricant is to prevent direct contact between the surfaces of the individual parts of the rolling element bearing. It also reduces wear and helps to avoid corrosion. A rolling element bearing can be lubricated by different media depending on the operating conditions and other factors. Grease and oils in different qualities with different properties are in use but also special lubricants - for example solid lubricants - are available.
As a result of mechanical work, ageing, contamination and other environmental influences, the lubricant changes its lubricating properties and it is therefore necessary to renew and/or filter the medium in regular intervals.

1.6.1 Grease

Under normal operating conditions, in the majority of applications grease can be used to lubricate the rolling bearing. It has the advantage over oil that it is more easily retained in the bearing arrangement and it also contributes to sealing the arrangement against contaminants.

1.6.2 Oil

When speeds or operating temperatures are too extreme to use grease, oil is used for rolling bearing lubrication. Another benefit of oil is the ability for removing heat generated by friction or other phenomena from the bearing position by circulation of the lubricant in a closed circuit. For practical reasons oil lubrication is also used when adjacent components are lubricated with oil.

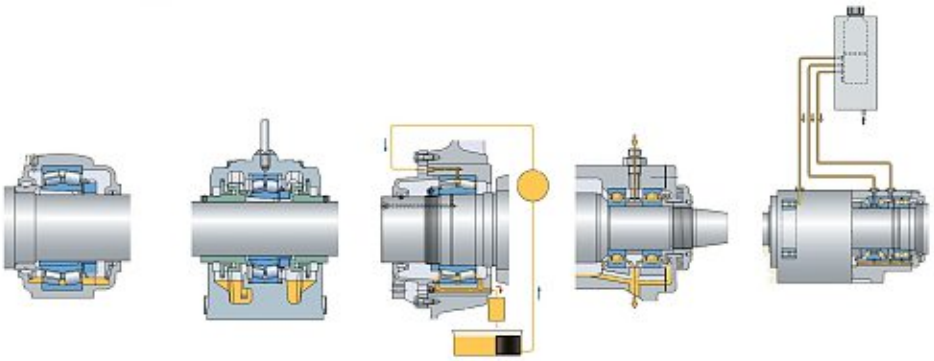

Figure 11: Methods of oil lubrication [2]

Many different methods of oil lubrication are established, for example (Figure 11):

- Oil bath
- Oil pick-up ring
- Circulating oil
- Oil jet
- Oil spot
- Oil mist

2 BEAST - BEAring Simulation Tool

The BEAring Simulation Tool (BEAST) is an advanced program for 3-dimensional simulations of dynamic multi-body systems specialized in detailed contact calculations. As proprietary SKF software, it is applied on all types of bearings and many other machine elements where contacts are important. BEAST enables studies of internal motions and forces in a bearing under given loading conditions. The model is fully 3-dimensional and all components have six or more degrees of freedom. It simultaneously solves the dynamics of the multi-body system, the structural deformations of the bodies, the thermal state and the local contact conditions including lubrication. So it is a virtual test rig for development and advanced applied engineering and helps SKF engineers building knowledge about their products and is also used for optimizing product design.

BEAST is actually the collective name of a number of tools or computer programs that are used to perform analysis of bearings. The most important tools are visualized in Figure 12 and described below [5]:

Beauty is an advanced 3D graphical tool designed for setting up the model and simulation parameters in the input files and visualizing the output files. Some of the features of the tool include animating the simulated sequence from different viewpoints, visualization of force vectors and surface associated data (such as pressure distribution). The visual representation of the simulation results in BEAUTY in an easily understandable way contributes to a quicker interpretation of the result and popularity of the complete toolbox among the users.

ViewBeast is specially designed for 2D plot presentation and analysis. In addition to the basic functionality, i.e., curve plotting, different operations on the simulation results are possible. For example, the user can apply Fourier transforms to a variable or specify his/her own function on several variables.

RunBeast is a remote simulation interface system. The tool provides a user-friendly interface for submitting a simulation on a remote computation server which is often a parallel computer.

BEAST is the main simulation program. It reads in a model specification from input files, performs the simulation and generates a set of output files containing the results.

Out2In is a small utility that allows generation of new input files from the simulation output files. In this way the user is given a chance to interrupt the simulation, modify some parameters, and continue the simulation from the moment where the previous run was terminated. This means that the results of one simulation can be used as the initial conditions for another.

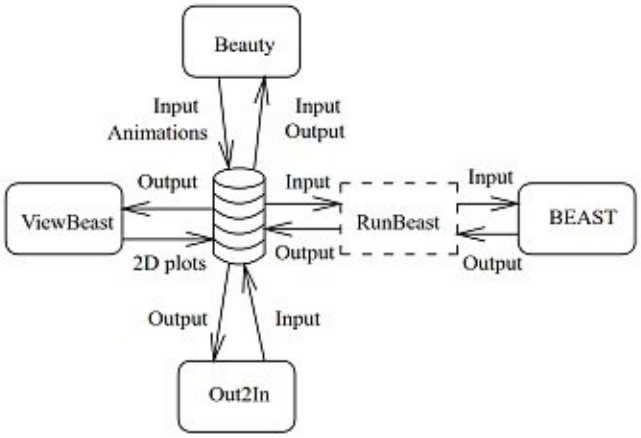

Figure 12: BEAST toolbox [3],[5]

A detailed overview of the structure of a `BEAST` model, the friction and contact model and the fatigue calculation can be found in [3].

3 ACBB - High Speed Test

The High Speed Test was done to investigate the running performance of machined brass cages in severe operating conditions with high speed (and high temperature) and to verify the values for limiting speed ratings. The test was executed on a suitable test rig with two Single Row Angular Contact Ball Bearings 7313, as shown in Figure 13. Each bearing was tested under combined load of typical compressor application conditions.

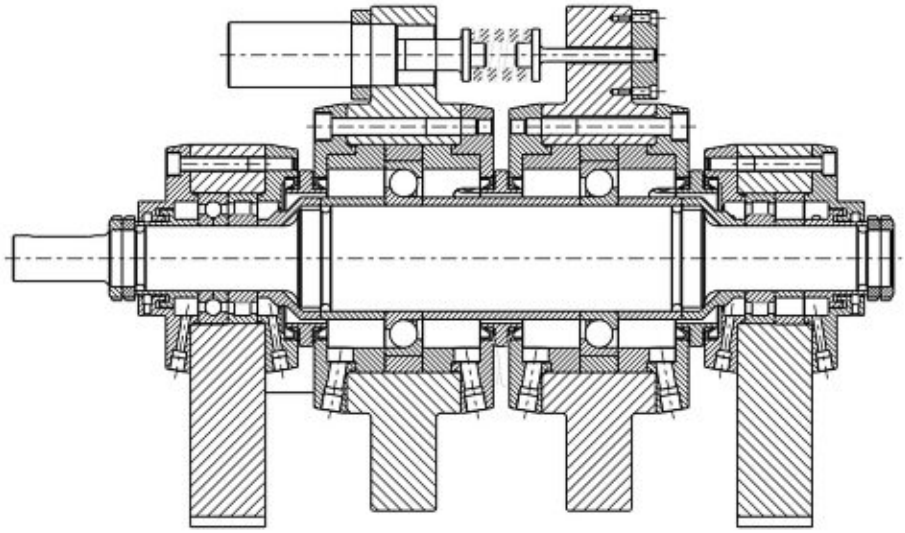

Figure 13: Cross-section of the testing arrangement

This test was executed by SKF. Since the measurement of a rotating bearing can be difficult, also a multi-body simulation with similar operating conditions was performed in section 3.2. The goal of the simulation is to get a better insight in the inner forces and the interplay of the components of the investigated Single Row Angular Contact Ball Bearing.

3.1 Analytical Calculations [2],[11]

Before starting a complex simulation, some analytical calculations have been performed. On the one hand these results can be used as a reference for the simulation and on the other hand, also some basic information can be gathered in this way.

3.1.1 Kinematics of the Angular Contact Ball Bearing

In this section, we take a look at the kinematics of the ACBB and use simple models to quantify the determined movement of its components.

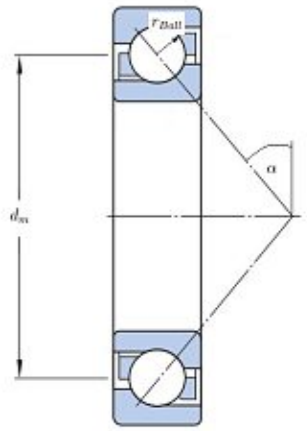

Figure 14: Simple model of the ACBB

From a simple model of the ACBB (Figure 14) , we obtain the following equations describing the geometry of the bearing:

$$R_{OR,contact} = \frac{d_m}{2} + r_{Ball} \cdot \cos\alpha \tag{1}$$

$$R_{IR,contact} = \frac{d_m}{2} - r_{Ball} \cdot \cos\alpha, \tag{2}$$

where $R_{OR,contact}$ and $R_{IR,contact}$ are the radii of the two contact points between the raceways of the inner ring respectively the outer ring and the ball. The line between these

two points represent the direction of the forces transferred between the rings. It is skew with an angle of α around the vertical axis of the bearing. The investigated ACBB has a specific angle - called contact angle - of $\alpha = \alpha_0 = 40°$.

For a rotating inner ring and a stationary outer ring we can describe the kinematics of the components of the bearing in the following way:

At first we want to investigate the circumferential velocity of the point at the inner ring at which contact with the ball occurs. Using the well known equation for circular motion and the radius given in equation (2), we get

$$v_{IR,contact} = R_{IR,contact} \cdot \omega_{IR} = \omega_{IR} \cdot \left(\frac{d_m}{2} - r_{Ball} \cdot \cos \alpha \right). \tag{3}$$

In a next step we want to quantify the velocity of the cage at a point at the pitch circle. Since this velocity is given through the arithmetic mean of the velocities of the circumferential speed of the contact points of both rings, we obtain

$$v_{cage} = \frac{v_{IR,contact} + v_{OR,contact}}{2} = \frac{v_{IR,contact}}{2} = \frac{\omega_{IR}}{2} \cdot \left(\frac{d_m}{2} - r_{Ball} \cdot \cos \alpha \right). \tag{4}$$

Since in this simplified model no slipping between the ball and the raceways appears, the velocity of the ball in the contact point has to be equal to the velocity of the same point on the inner ring:

$$v_{Ball,contact} = \omega_{IR} \cdot \left(\frac{d_m}{2} - r_{Ball} \cdot \cos \alpha \right). \tag{5}$$

Considering this simplification the angular velocity of the ball can be described as follows:

$$\omega_{Ball} = -\frac{\omega_{IR}}{2} \cdot \left(\frac{d_m}{2 \cdot r_{Ball}} - \frac{2 \cdot r_{Ball} \cdot \cos^2 \alpha}{d_m} \right). \tag{6}$$

As a last step, we use the equation

$$\omega_{Cage} = \frac{2 \cdot v_{cage}}{d_m} \tag{7}$$

to obtain the angular velocity of the cage.

For the Angular Contact Ball Bearing 7313 we use the parameters given in Table 2 and obtain the kinematic values presented in Table 3.

Parameter	Symbol	Value	Unit
Pitch circle diameter	d_m	102.5	mm
Radius of the ball	r_{Ball}	12.30	mm
Contact angle	α	40	°
Angular velocity of the inner ring	ω_{IR}	141.67	1/s

Table 2: Parameters of the Angular Contact Ball Bearing 7313 [2]

Parameter	Symbol	Value	Unit
Radius on the outer ring	$R_{OR,contact}$	60.67	mm
Radius on the inner ring	$R_{IR,contact}$	41.83	mm
Velocity on the inner ring	$v_{IR,contact}$	5.93	m/s
Velocity of the cage	v_{cage}	2.96	m/s
Angular velocity of the ball	ω_{Ball}	-212.01	1/s
Angular velocity of the cage	ω_{Cage}	57.76	1/s

Table 3: Calculated values of the Angular Contact Ball Bearing 7313

3.2 Virtual Test [3],[10]

In this section, a general way for building a model of the Single Row Angular Contact Ball Bearing 7313 is described. Since it is not possible to describe every detail in an exact way, the main aim of the remarks in this section is to give a short guideline for building models in BEAST and also to provide the necessary background information to interpret the results presented in the following section 3.2.9.

3.2.1 Model building

The High Speed Test was simulated in the virtual test rig BEAST. The model (Figure 15) consists of 15 bodies (outer ring, inner ring, 12 balls and the machined cage) and lubricant (oil). In order to investigate the state of stress of the machined brass cage, this body is modeled as a flexible body but all other bodies are rigid. The contact forces acting between the bodies (rigid and/or flexible) are calculated in BEAST (as described in [7]).

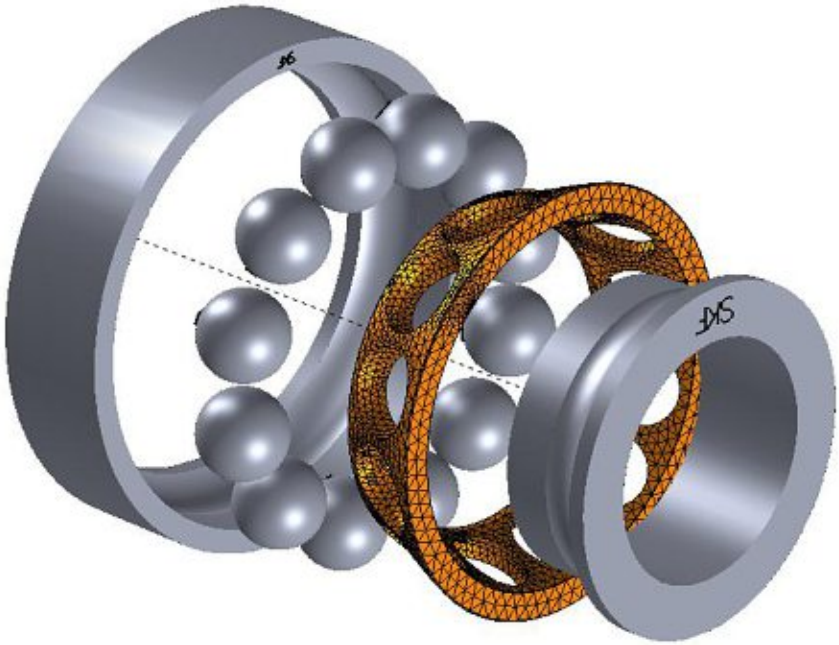

Figure 15: Exploded View of the ACBB BEAST-model

3.2.2 Material Parameters

The material parameters can be defined at body level. There are several materials predefined in BEAST and grouped in the following material types:

- Steels
- Metal alloys
- Plastics
- Ceramics

Both of the rings and the balls of the Angular Contact Ball Bearing are made of steel. The cage is a machined brass cage. The material parameters of the bodies used in the simulation are given in Table 4. All of these parameters can be manipulated by the user at body-level to define any user specific material.

	Rings/Balls	Cage	Unit
Material	Steel	Brass	
E-modulus	2.03e+11	8.87e+10	Pa
Poisson ratio	0.29	0.34	
Density	7.79e+3	8.42e+3	kg/m^3
Thermal conductivity	46.6	117.5	W/(m*C)
Thermal expansion	1.26e-5	2.08e-5	1/C
Specific heat	475	380	J/(kg*C)
Friction damping coefficient	0.0224	0.0432	
Hardness	7.35525e+9	1.000314e+9	Pa
Sigma yield	1.725e+9	1.425e+8	Pa
Ultimate tensile strength	2.28e+9	3.91e+8	Pa
Structural fatigue limit due to bending	9.4e+8	7.58e+7	Pa
Threshold stress intensity factor range	5.5e+6	7.8e+6	Pa*m$^{(1/2)}$

Table 4: Material Parameters used in BEAST

A rolling element bearing not only consists of bodies but also of a lubricant medium such as for example oil or grease. As the lubricant is part of the rolling element bearing respectively the model, the lubricant has to be selected or manipulated on model level.

The bearing investigated in the simulation is oil lubricated (Shell Turbo T68) with the lubricant parameters given in Table 5.

Kinematic viscosity at temperature 1	6.8e-5	$[m^2/s]$
Temperature 1	40	[C]
Kinematic viscosity at temperature 2	8.6e-6	$[m^2/s]$
Temperature 2	100	[C]
Density at atmospheric pressure	876	$[kg/m^3]$
Pressure viscosity coeff. at temp. 1 and atm. pressure	2.3e-8	[1/Pa]
Temp. 1 in the pressure visc. coeff. calculation	20	[C]
Pressure visc. coeff. at temp. 2 and atm. pressure	1.62e-8	[1/Pa]
Temp. 2 in the pressure visc. coeff. calculation	80	[C]
Temp. at which lub. density at atm. pressure is given	0	[C]
Density temperature coeff. at atm. pressure	0	$[kg/(m^3 * C)]$
Surface tension coefficient	0.05	[N/m]
Specific heat capacity at temperature 1	1.886e+3	[J/(kg*K)]
Temp. 1 at which the spec. heat capacity is given	20	[C]
Coeff. for spec. heat temp. dependency at given temp.	0.0011996	[J/(kg*K*K)]
Thermal conductivity	0.117	[W/(m*C)]
limiting shear stress at zero pressure	2.e+6	[Pa]
Constant in Roelands viscosity formular	1.98e+8	[Pa]

Table 5: Lubricant Parameters used in BEAST

3.2.3 Mesh Parameters

Flexible bodies have to be discretized in order to be able to perform FE-calculations. The mesh parameters can be found and manipulated on body level.

BEAST uses a global parameter to quantify the global mesh size of the body (cage) and a parameter for the desired maximum deviation of the mesh from the body. For the present simulation a mesh size of 4 mm and a deviation factor of 0.1 mm were chosen. In order to get more accurate results, especially for the stresses in the investigated cage pocket, mesh refinement was carried out at areas of interest in the cage pockets. Figure 16 shows the meshed cage and also a section of the cage including cage pocket 1 and cage pocket 2 with the refined mesh.

To be able to perform mesh refinement, the user has to define flexible coordinate systems at the point where a finer mesh is desired. The center of such a flexible coordinate system is equivalent to the center of a sphere with arbitrary radius, called influence radius. This influence sphere defines the area in which refinement is performed.

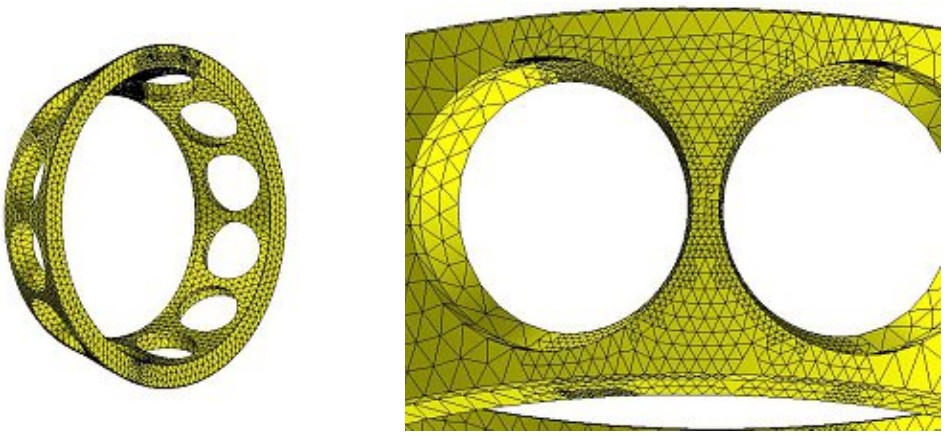

Figure 16: Global and refined mesh

3.2.4 Model reduction

On body level, each body can be defined either as a rigid body or a flexible body. To specify an elasitc body in BEAST, the user has to activate elastic and thermal shapes. The BEAST Users Manual [3] gives a detailed overview of how to model elastic bodies in BEAST.

In the present model the global parameters for the elastic shapes of the cage are set as follows:

- Cut off frequency is set to $1e10$ Hz. The frequencies above this limit are removed.
- Eigenmode shapes are activated. The type of constraints from active static mode shapes which is used in the eigenmodes computation is set to all constraints from static mode shapes.
- The maximum number of eigenmodes excluding the rigid body modes is set to 60.
- Centrifugal shapes with respect to the axes of inertia are included in the reduction.
- Static deformation and static load mode shapes are included in the reduction. The type of constraints from active mode shapes is set to: Free load modes and constrained deformation modes.

Information about the used mode shapes in BEAST (eigenmode shapes, centrifugal shapes, static deformation shapes and static load mode shapes) can be found in [3].

Additionally to the global settings of the elastic body, also the parameters for the contact surface segments have to be defined. As static mode shapes are activated on the global

level, they can be defined for each contact segment. In this model static load mode shapes are used for the set of cage pocket segments (sC, sCB) and their order is set to three for the u-direction and two for the v-direction. In Figure 17, the local coordinate systems for the two cage pocket segments (sC, sCB) are pictured.

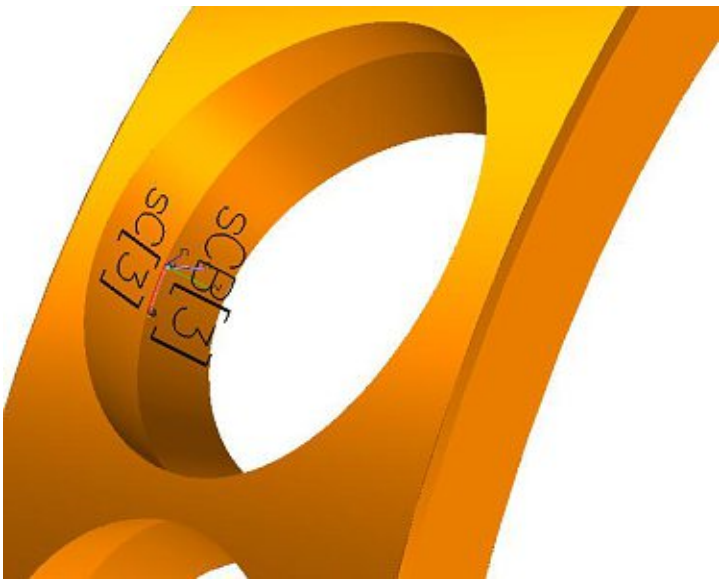

Figure 17: Local coordinate systems of the cage pocket segments

3.2.5 Tribology

In order to get a good tribology model, the parameters for surface roughness and lubricant film thickness in the contact surfaces have to be set in a proper way. The surface roughness of the cage pocket surfaces is set to 1.25 μm and the initial lubricant film thickness is set to 1.0 μm. The raceways of the rings are modeled with the default values for surface roughness (0.1 μm) and lubricant film thickness (1.0 μm) and the value of the surface roughness of the rolling elements are similar to the one for the raceways (0.1 μm).

3.2.6 Boundary conditions

The boundary conditions are applied to the components of the bearing in form of ties. Each tie is a relation between bodies or a body and a coordinate system (Figure 18). In this way bodies can be fixed in any degree of freedom or prescribed motions or forces can be applied.

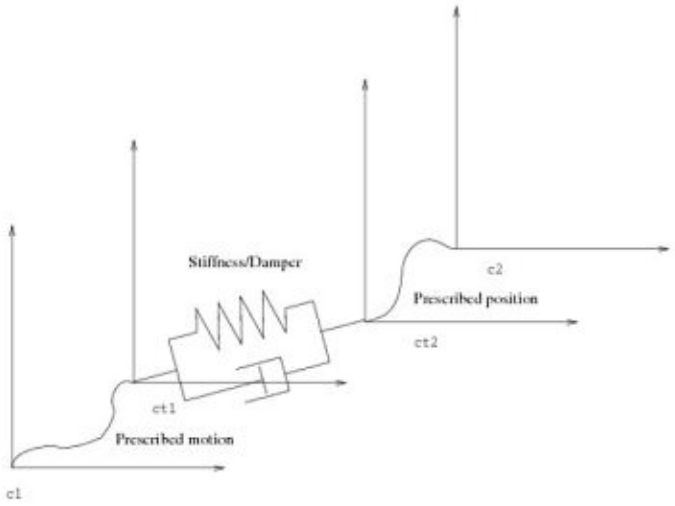

Figure 18: Schematic presentation of a connection between bodies or coordinate systems [3]

As a tie is a three-dimensional connection, it contains stiffness and damping parameters. The spring and damper tie (SD) between the coordinate systems make it possible to model all different load cases with the same set of equations. The only difference are the numerical values for the spring and damper characteristics. The springs and dampers are given as a set of linear stiffness and damping matrices. If the spring is very stiff, the motion of the coordinate system and the bearing component will in practise be the same. This is used when a prescribed motion is wanted. In order to achieve a fixed connection, one can model ties with extreme high stiffness parameters (-10^{12}, -10^{10}).

Five connections are integrated in the model. These are the connection between the cB-coordinate system and the inner ring (cB:bIR) with a SD-tie and the one between the cB-coordinate system and the outer ring (cB:bOR) with a SD-tie and a Load-tie and the three contact sets between the inner ring and the balls (bIR:bW), the outer ring and the balls (bOR:bW) and the cage and the balls (bC:bW). The stiffness and damping matrices for the two SD-ties are given below:

cB:bIR - SD-tie

- stiffness matrix - relative translation (in [N/m]):

$$\begin{bmatrix} -1e12 & 0 & 0 \\ 0 & -1e12 & 0 \\ 0 & 0 & -1e12 \end{bmatrix}$$

- damping matrix - relative translation (in [Ns/m]):

$$\begin{bmatrix} -1e10 & 0 & 0 \\ 0 & -1e10 & 0 \\ 0 & 0 & -1e10 \end{bmatrix}$$

- stiffness matrix - relative rotation (in [Nm]):

$$\begin{bmatrix} -1e10 & 0 & 0 \\ 0 & -1e10 & 0 \\ 0 & 0 & -1e10 \end{bmatrix}$$

- damping matrix - relative rotation (in [Nms]):

$$\begin{bmatrix} -1e8 & 0 & 0 \\ 0 & -1e8 & 0 \\ 0 & 0 & -1e8 \end{bmatrix}$$

cB:bOR - SD-tie

- stiffness matrix - relative translation (in [N/m]):

$$\begin{bmatrix} 0 & 0 & 0 \\ 0 & 0 & 0 \\ 0 & 0 & 0 \end{bmatrix}$$

- damping matrix - relative translation (in [Ns/m]):

$$\begin{bmatrix} 0 & 0 & 0 \\ 0 & 0 & 0 \\ 0 & 0 & 0 \end{bmatrix}$$

- stiffness matrix - relative rotation (in [Nm]):

$$\begin{bmatrix} -1e10 & 0 & 0 \\ 0 & -1e10 & 0 \\ 0 & 0 & -1e10 \end{bmatrix}$$

- damping matrix - relative rotation (in [Nms]):

$$\begin{bmatrix} -1e8 & 0 & 0 \\ 0 & -1e8 & 0 \\ 0 & 0 & -1e8 \end{bmatrix}$$

The tie between the outer ring and the environment forces the outer ring to stay free of rotation around all three axis. It is therefore only free to move translational in all three directions.

The loads are applied on the outer ring with a Load-tie in form of a ramp function as pictured in Figure 19.

3.2.7 Time and Output

When we use the variable ω_{max} for the maximum angular velocity of the inner ring, we can calculate a characteristic time for the simulation, which represents the time of a single revolution of the inner ring:

$$t_{rot} = \frac{2\pi}{\omega_{max}}. \tag{8}$$

The chosen entire simulation time is as long as it takes the inner ring with maximum speed to perform 30 rotations

$$t_{sim} = 30 \cdot t_{rot} = 30\frac{2\pi}{\omega_{max}}. \tag{9}$$

To realize a smooth start-up of the simulation, the forces and the speed of the inner ring applied in form of a ramp function as given in Figure 19. The values of the forces and the speed started from zero and reached their final values after $t = 10 \cdot t_{rot}$. In order to reduce the needed disc space, only data from the steady-state is written out. The start time for writing out data is here defined as

$$t_{write} = 20 \cdot t_{rot} = 20\frac{2\pi}{\omega_{max}}. \tag{10}$$

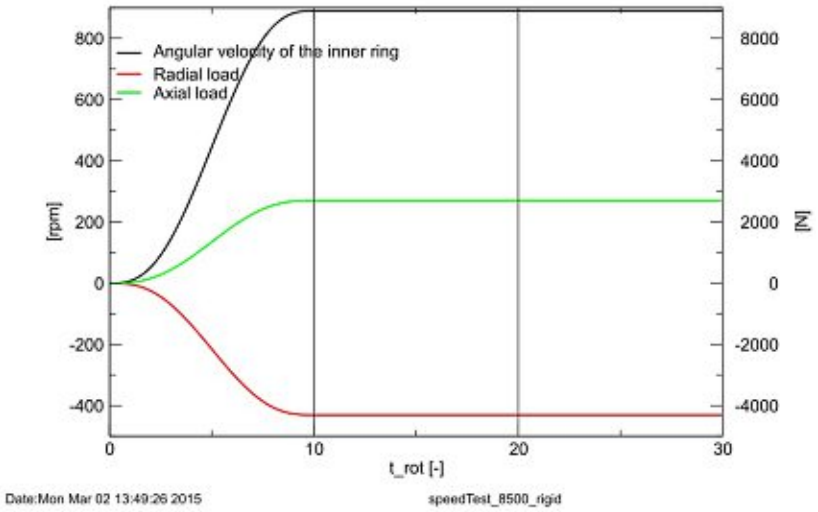

Figure 19: Start-up phase realized with ramp function

3.2.8 Solver settings

In the actual BEAST version, three solvers are implemented [3]. The user can choose between the following solvers:

- CVODE
- IDA
- SE.

According to the guidelines provided by the BEAST-developers, the SE solver has been used for the actual simulation of the ACBB.

Setting the MaxTimeStep variable correctly prevents the solver to become unstable. When solver settings become too rough and the maximum time-step is not suitably small, the error can increase enormously. To guarantee the stability of the SE solver, the time step has to be smaller than the smallest time period corresponding to the largest eigen-frequency of the discretised mechanical system.

3.2.9 Results of the simulation

Two simulations were performed. The first simulation (case A) is investigated in this section and the second one (case B) is a simulation with extreme load and speed parameters, which is the basis for fatigue calculation performed in the following section 4. The operating conditions used in the simulations are given in Table 6 with respect to the global coordinate system. That means that the axial load is acting on the outer ring in the positive global z-direction and the radial load is also acting on the outer ring in direction of the negative global x-direction. In this work, the results for case A are discussed in a detailed way.

	A	B
Speed	8 500 rpm	14 000 rpm
Axial load	2 700 N	7 150 N
Radial load	-4 310 N	-5 000 N

Table 6: Operation conditions for the simulation

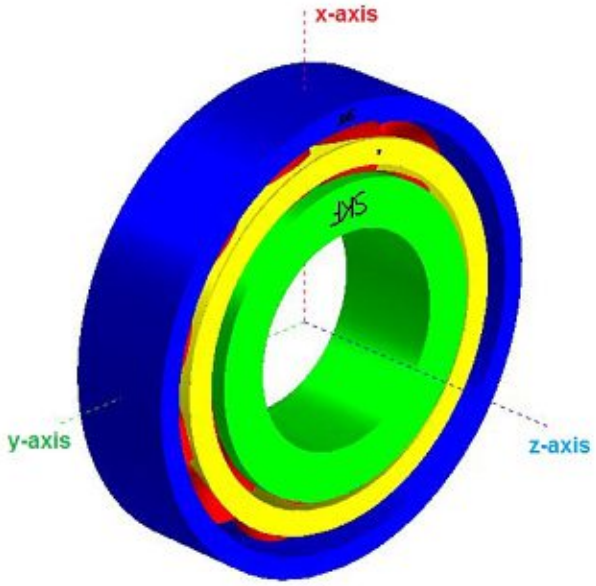

Figure 20: Assembled Angular Contact Ball Bearing relative to global coordinate system

Kinematics of the bearing elements, the stress distribution and the deformation of the cage are investigated. The operating conditions defined for case B are used to test the fatigue calculation tool implemented in BEAST. As mentioned before, only steady state data was written out. In order to get a good insight in the behavior of the cage, the last three cage rotations were analyzed.

3.2.10 Kinematics of the bearing

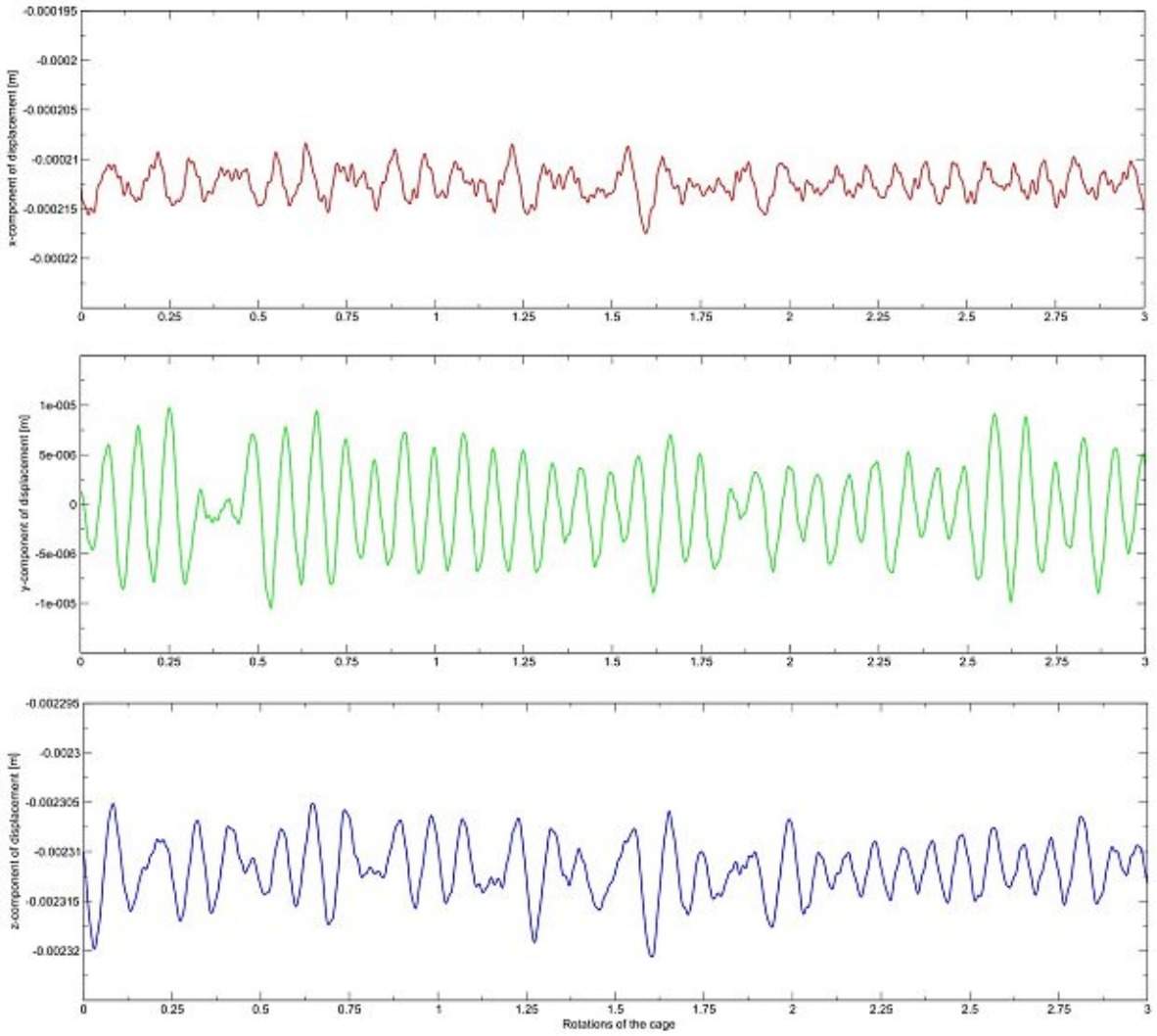

Figure 21: Movement of the outer ring

Movement of the rings

As a first step the movement of the rings should be investigated. In section 3.2.6 the boundary conditions for both of the rings are defined. Only these two bearing components are connected with the environment. The inner ring is fixed on a virtual and cylindrical shaft (modeled as a rotating coordinate system) which rotates around its axis. Since the movement of the shaft is predetermined as a rotation around the x-axis only, the inner ring is also rotating only around this axis. This means that the inner ring is not able to perform a translation in the x, y or z direction. Because of the internal clearance of the bearing and the forces acting on the outer ring, this element has to be able to move, otherwise the applied force will not act. In this model the outer ring is able to perform a translation in the x, y and z direction but all rotations are locked.

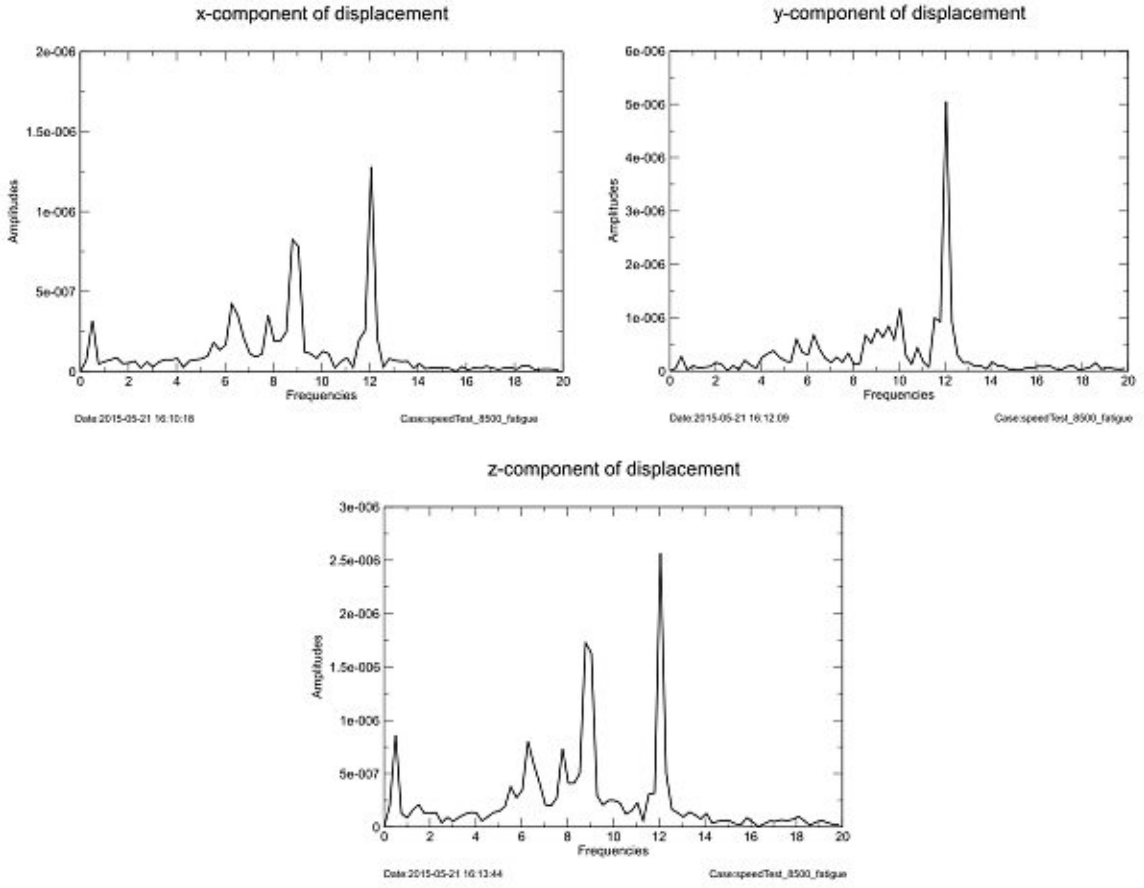

Figure 22: Amplitude spectra of the movement of the outer ring

Figure 21 shows the displacement of the geometric center of the outer ring as a function of the rotation of the cage calculated in the simulation. According to this result a periodicity of 1/12 cage rotations can be identified. Performing a Fourier transformation (Figure 22) confirms this characteristic. This behavior is caused by the relative movement of the 12 balls versus the still standing outer ring during one revolution of the cage. The offset is a result of the deviation from the nominal start position of the element because the relative position of the outer ring is a result of the actual operating conditions.

In the simulation the maximum peak-to-peak value of the movement of the outer ring in the z-direction is approximately 15 μm (Figure 21).

Another result that should be investigated is the translational velocity of the geometric center of the outer ring, which is shown in Figure 23. All tree components are alternating between positive and negative velocity with a maximum speed of approximately 0.04 m/s. Since the bearing is equipped with 12 balls, there can be identified 12 periods per rotation of the cage, especially for the y-component of the velocity. The vibration of the outer ring is therefore linked with the number of balls.

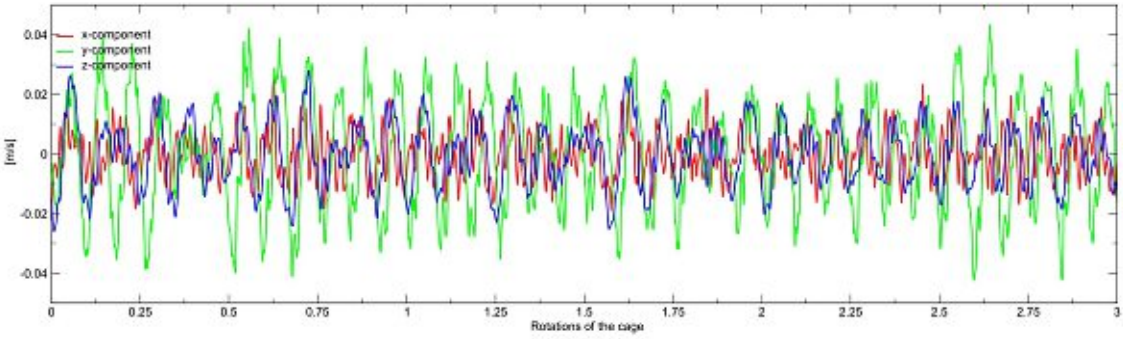

Figure 23: Translational velocity of the center of the outer ring

Movement of the cage

In the ACBB 7313 used in this model, a machined brass cage is included which is guided by the rolling elements. Therefore contact between the rings and the cage should not appear. The position of the cage relative to the global coordinate system is illustrated in Figure 24 and the velocities of the center of the cage with respect to the global coordinate system are plotted in Figure 25.

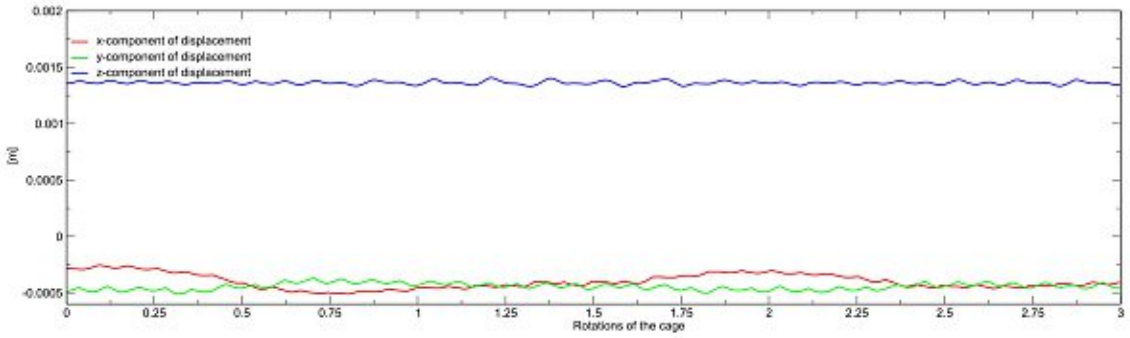

Figure 24: Movement of the cage

Similar to the results of the outer ring, also here the offset in Figure 24 is a result of the deviation from the nominal start position caused by the load.

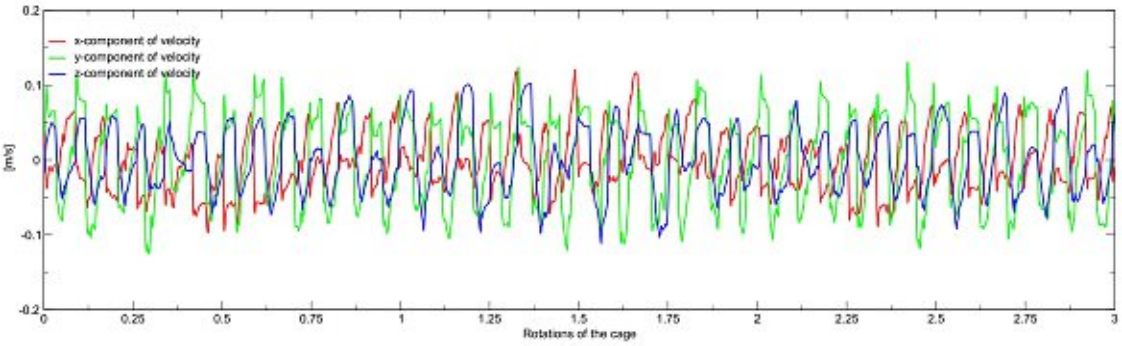

Figure 25: Translational velocity of the center of the cage

A way to get better information about the frequency of the translational velocity of the center of the cage is to perform a Fourier transformation to obtain the amplitude spectra.

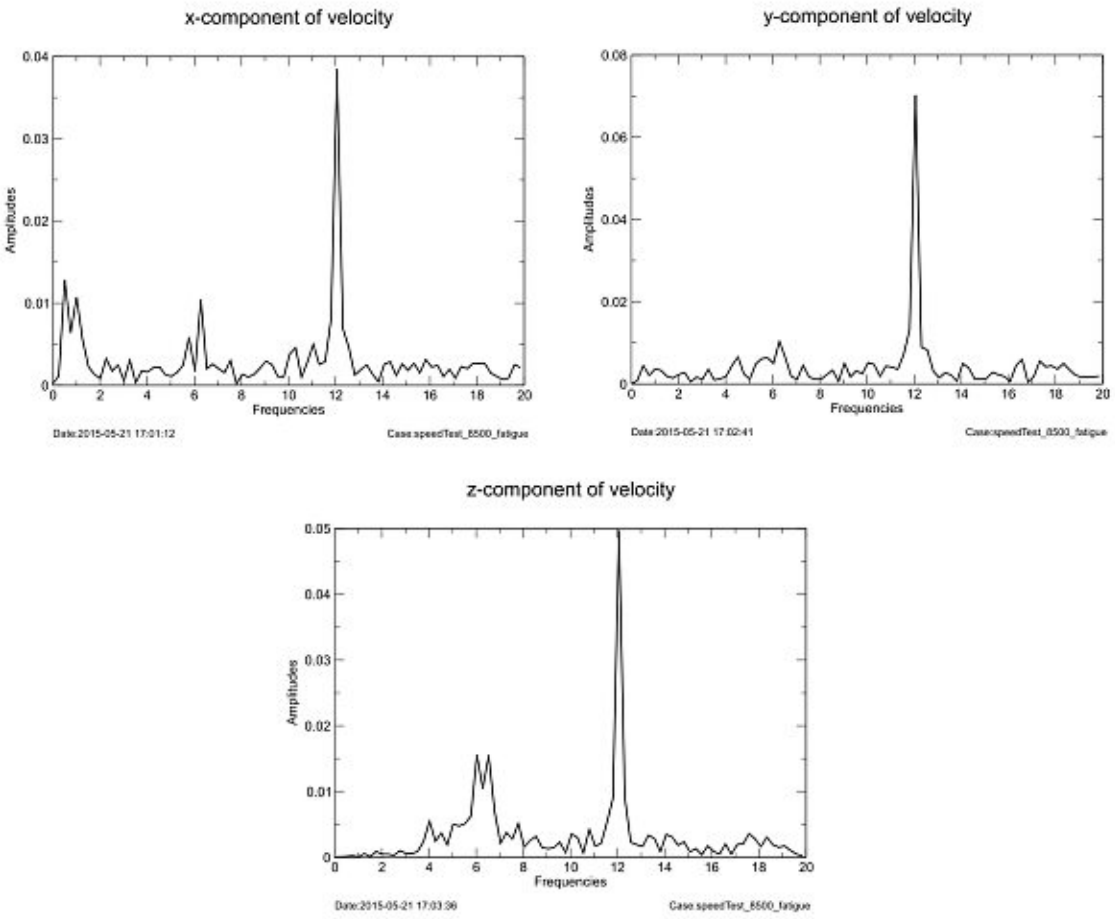

Figure 26: Amplitude spectra of the velocity of the center of the cage

In Figure 26 the results of such an analysis are shown and we can see that the velocity has a main frequency (cage rotations) of 12 corresponding to the number of balls in the bearing.

Because of the constant angular velocity of the inner ring and the interdependency with the 12 balls, we expect a non constant but periodic characteristic of the angular velocity of the cage.

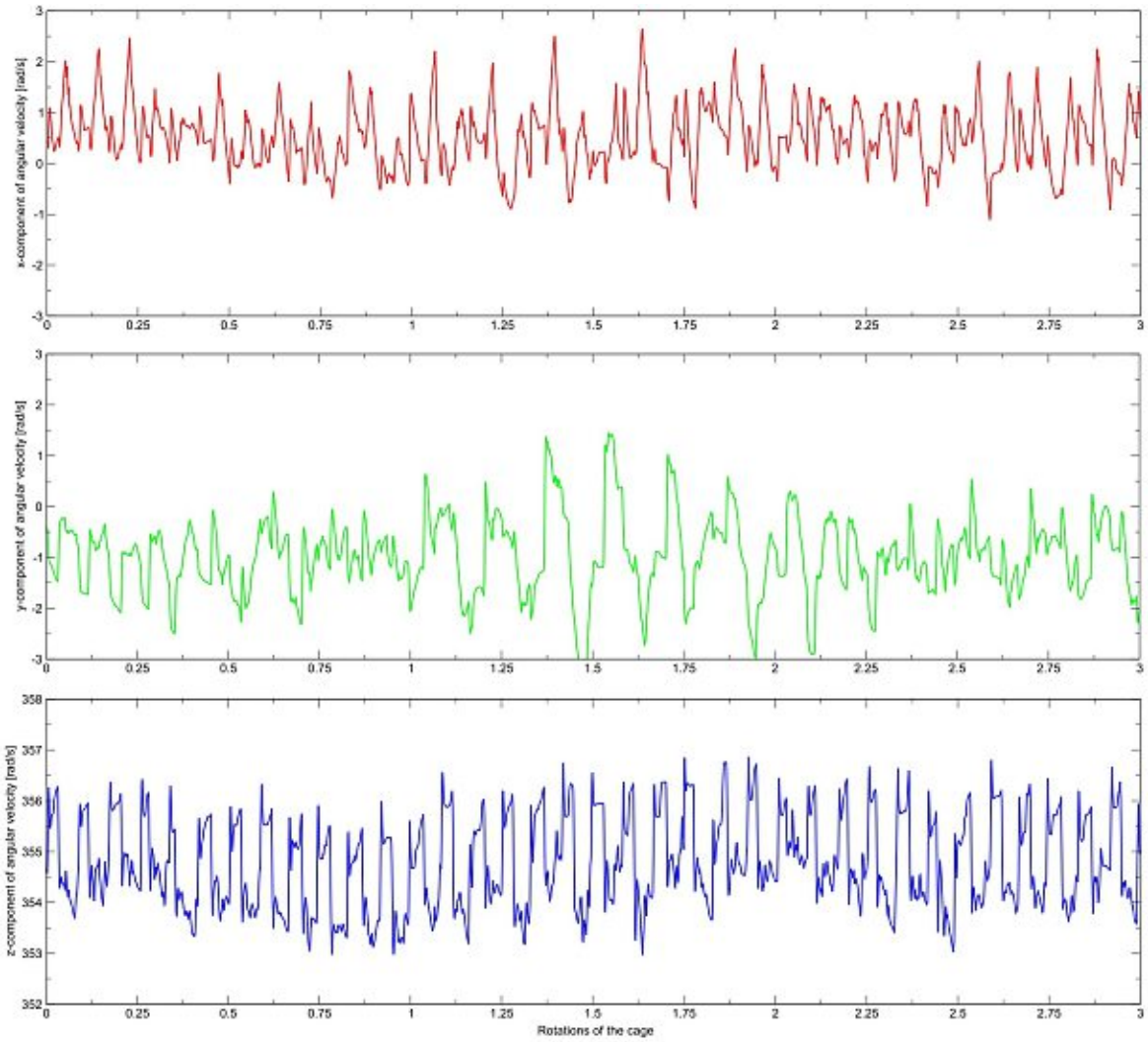

Figure 27: Angular velocity of the cage for case A

In Figure 27 the angular velocities of the cage for all three global coordinate directions are pictured. The cage mainly rotates around the global z-axis, but also movement around the other axis occur. The orientation of the total vector of the angular velocity is for this reason not identical with the global z-axis but differ sightly in the other directions. This means that the cage is not exactly vertical orientated but a little bit skew.

Picture 20 shows the global coordinate system (cB) and the nominal position of the bearing relative to it.

The mean value of the z-component of the angular velocity of the cage is 354.84 rad/s

or 56.47 1/s. To check the plausibility of this result, we use the analytical result from Table 3, which was 57.76 1/s. If we consider that no slipping effects are included in the analytical calculation, but in the simulation, the result seems to be reliable.

The difference between the maximum and the minimum value of the angular velocity of the cage in the z-direction during simulation time is 4.04 rad/s.

In Figure 28, the movement of the geometric center of the cage in the three relevant planes is given. The possibility of the cage to move in these planes and the quantity of these movements depends on the internal clearance of the bearing and the cage pocket geometry, respectively the clearance between the ball and the cage pocket. In this ACBB the area in which the center of mass of the cage can move is very small.

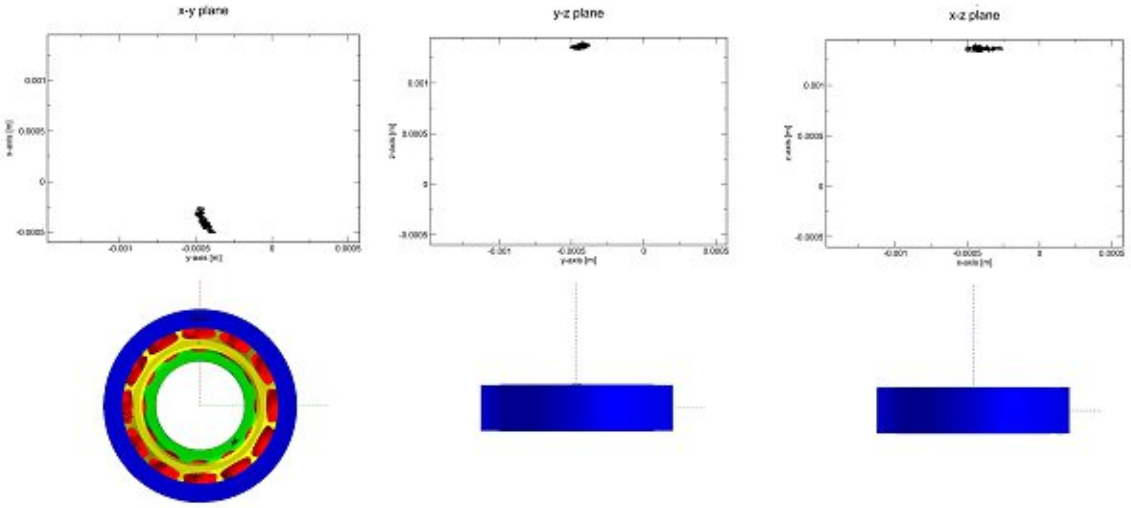

Figure 28: Movement of the cages center of mass for case A

Movement of the ball

To investigate the relative movement of the ball 1 versus the cage, the magnitude of the velocity of the center of mass of the ball 1 was plotted in Figure 29 as a function of the rotational position of the cage. During every rotation we can clearly identify a period of acceleration followed by a period of breaking. This means that in these periods the cage effects the ball.

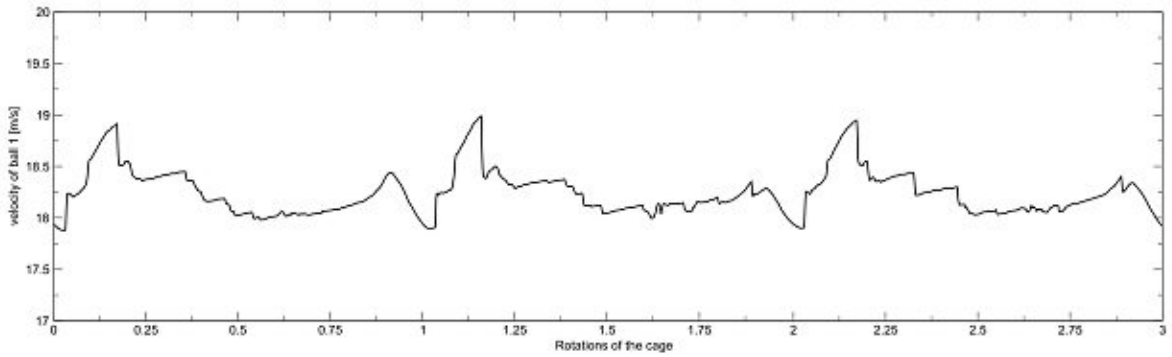

Figure 29: Velocity of the center of the ball 1

To get an idea of the relative kinematics of the two components effecting each other, Figure 30 recapitulates the issues of this section by visualizing the correlation between the speed of the cage and the speed of the 12 included balls.

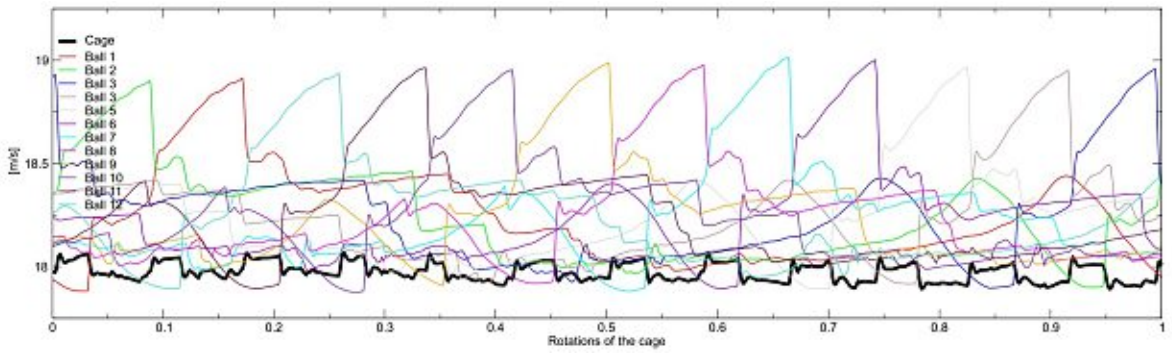

Figure 30: Relative kinematics of the cage vs. the balls

During one rotation every ball undergoes an abrupt acceleration and a prompt slow-down. This sudden changes in velocity are indicators for occurring contact between the ball and the cage. Because of this contact, forces are acting between the bodies. On the other hand also the velocity of the cage is influenced by the balls. As one can also see in Figure 30 the cage is accelerated and braked 12 times per rotation. This means that the cage get excited 12 times per rotation. As we will see in section 3.2.16 this leads to an excitation frequency which can be dangerous if it is identical with an eigen-frequency of the cage.

3.2.11 Load distribution and contact forces

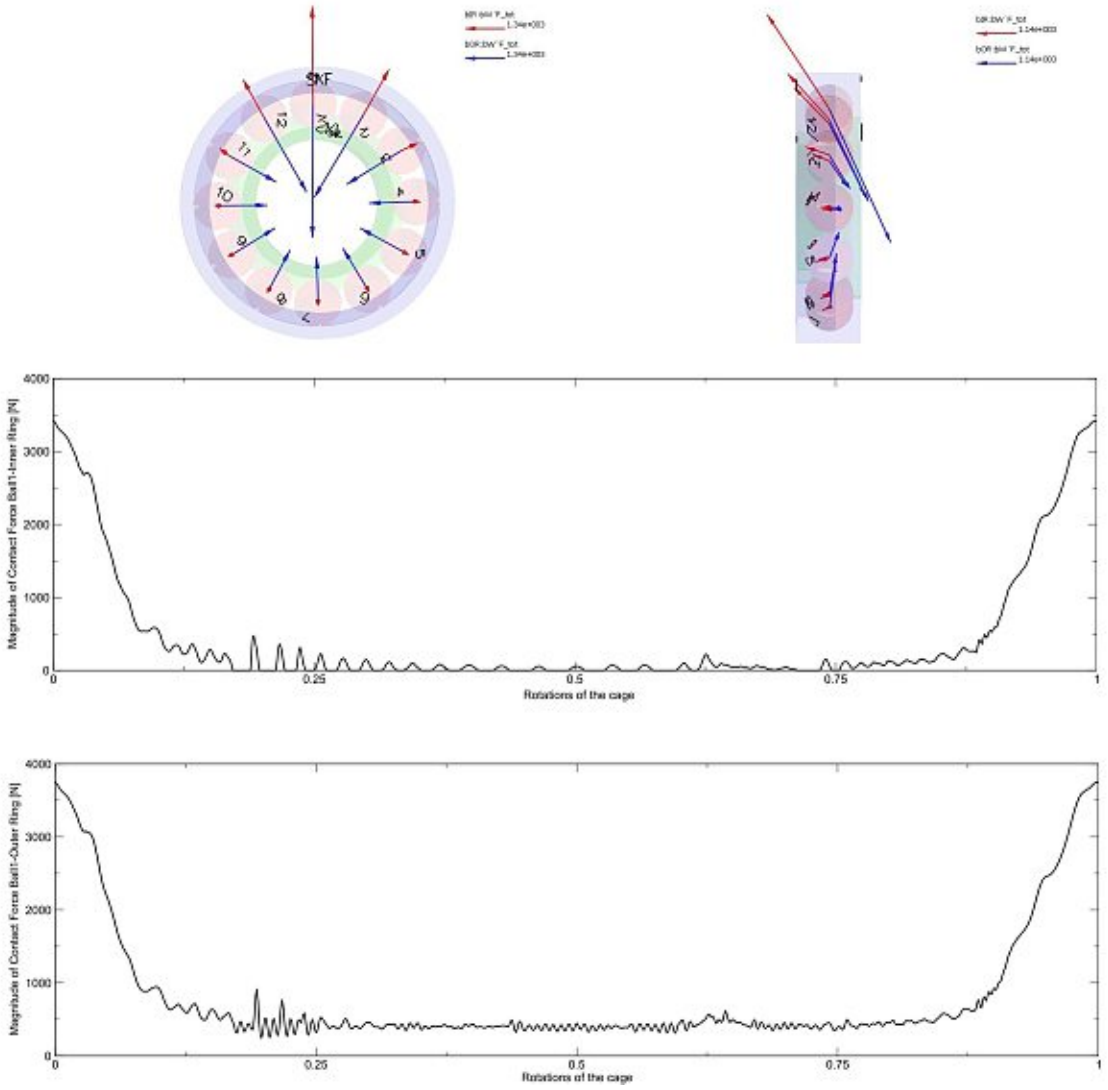

Figure 31: Load distribution for case A

During one revolution, every ball is alternating between the loaded and the unloaded zone. Figure 31 illustrates the force distribution for the simulated load case, from which the loaded zone can be identified. Since the external forces acting on the outer ring directed in the negative x-direction and the positive z-direction the maximum load appears on the top side of the bearing. In the loaded zone the balls are maximum loaded and their velocity is higher than the speed of the cage. In the unloaded zone the relative

kinematic status is inverse. This leads to a contact force which acts alternating between the ball and the front respectively the back surface of the cage pocket. According to Figure 33 we see that the maximum force occurs when the considered ball 1 is on the top position of the bearing. The contact force between the inner ring and the ball 1 nearly disappears when the ball 1 reaches an angle of $\frac{\pi}{4}$ rad relative to the global coordinate system. A similar situation can be observed for the force acting between the ball 1 and the outer ring, but here the force do not reach a value near zero, because the force of inertia of ball 1 is acting on the outer ring.

In Figure 32 we see the three components of the contact force and also the magnitude of the force acting between the ball 1 and the associated cage pocket during one rotation of the cage. The used coordinate system is the global system.

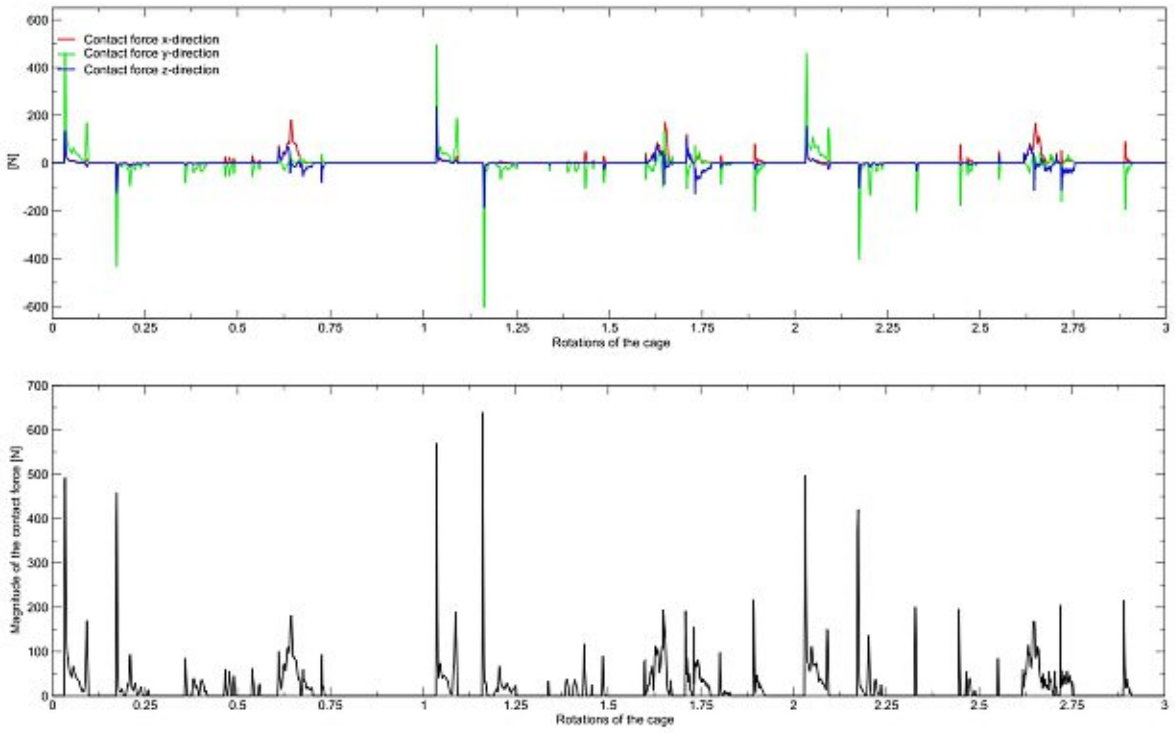

Figure 32: Contact forces for case A

To get the context to the results of the kinematic investigations, Figure 33 combines the technical expertises made so far. Every significant change of the velocity of the ball 1 corresponds to a peak of the contact force acting between the cage pocket 1 and the ball 1.

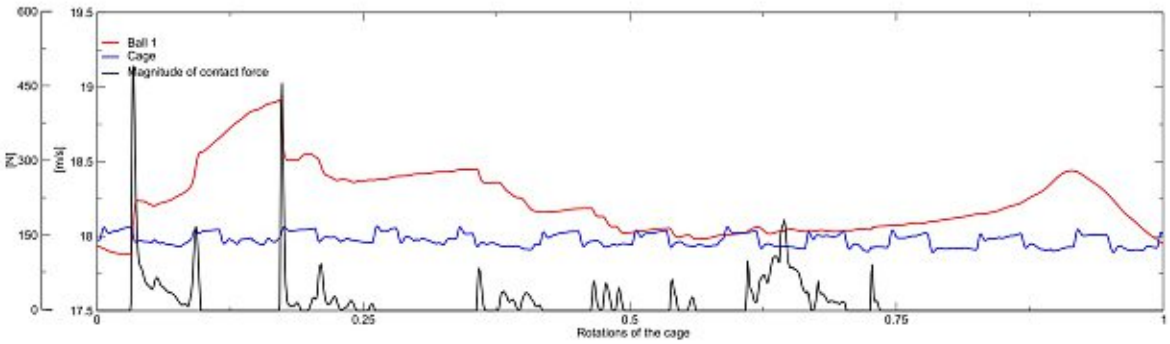

Figure 33: Dynamic situation of the bearing elements ball 1 and cage

3.2.12 Contact pressure

The contact forces cause local pressures in the cage pockets. The maximum magnitude of this contact pressure caused by Hertzian contact between the ball 1 and the cage pocket 1 is plotted in Figure 34. This plot does not include information about the exact location of the maximum pressure due to Hertzian contact. To identify the location of the maximum pressure, we have to take a look at the structural stresses, which is done in the following section 3.2.13. The local maximum pressure reaches values of around 1e9 Pa, which is much higher than the yield stress of the cage material.

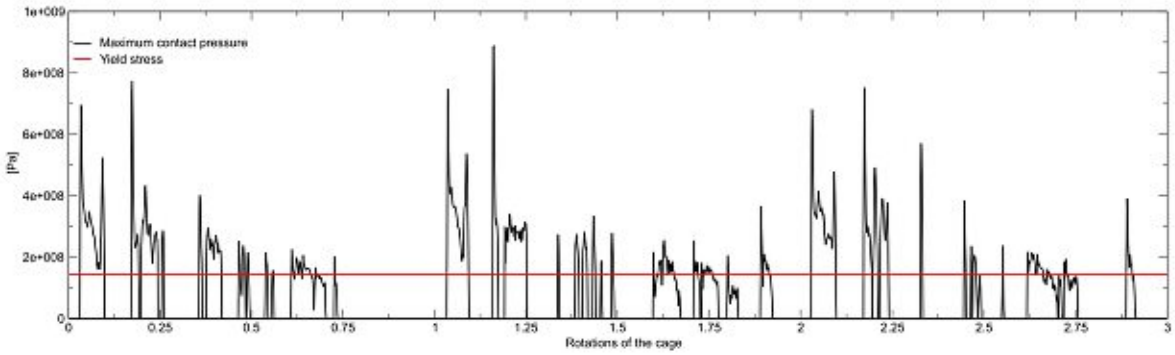

Figure 34: Maximum value of contact pressure due to Hertzian contact in the cage pocket

In Figure 35 the size of the contact area for cage pocket 1 is plotted as a function of the angular position of the cage. This plot also does not include information about the

location. But according to this result, we can see that there is no permanent contact between the ball and the cage pocket.

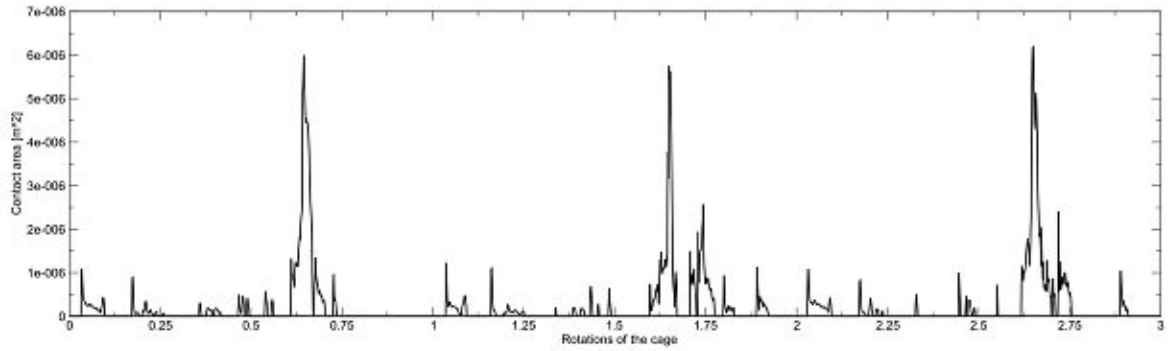

Figure 35: Contact area in the cage pocket

3.2.13 Structural stresses

In the post-processor BEAUTY, the results of the simulation can be visualized in form of an animation. With this tool, the user is able to monitor the behavior of the bearing and its components during the whole simulation time for which data was written out. In this case, the last 10 rotations of the inner ring can be analyzed with this software tool in a user defined resolution.

The v. Mises stresses of the cage can be visualized at every time step. Since the cage is symmetric around the z-axis with a symmetry angle of $\frac{\pi}{6}$ rad, only an angle of $\frac{\pi}{6}$ rad is investigated here to get a general idea of the distribution of the v. Mises stresses on the cage surfaces during rotation. Figure 36 shows the v. Mises stresses for four different time steps corresponding to the rotational angles of 0 rad, $\frac{\pi}{24}$ rad, $\frac{\pi}{12}$ rad and $\frac{\pi}{8}$ rad. It can be seen that the maximum stress appears on the front side respectively back side of the cage pocket. With this first result the global stresses of the cage are investigated and a more detailed analysis will be performed as a next step.

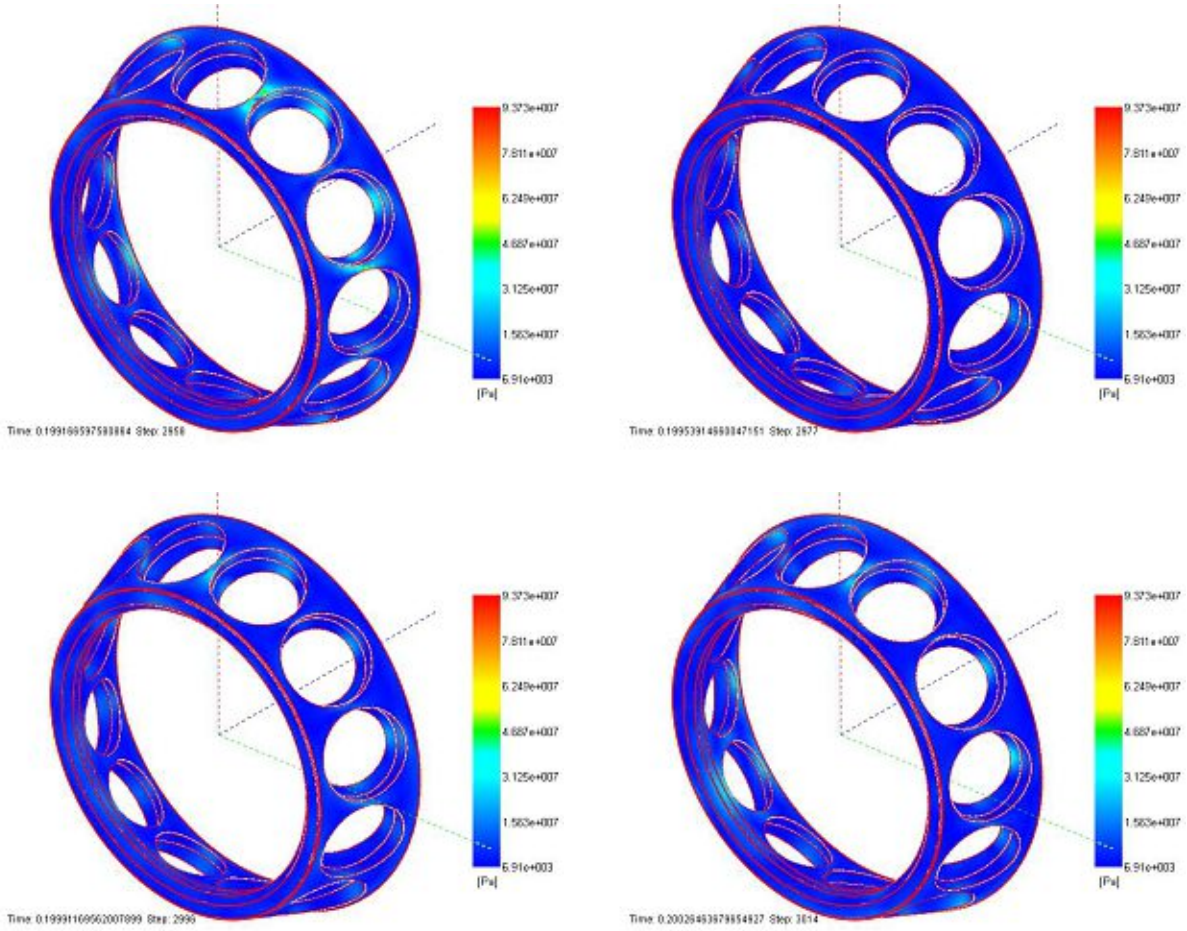

Figure 36: v. Mises stresses of the cage for different angular positions

The post-processor BEAUTY is suitable to search for the maximum v. Mises stresses and their location during one revolution of the cage. Since the mesh is refined in the section between cage pocket 1 and cage pocket 2 (Figure 16) only, the maximum v. Mises stresses are searched in this segment of the cage. Figure 37 shows the stress-plot of the refined cage segment. The maximum v. Mises stress occurs at an angular position of the cage of $\frac{28\pi}{15}$ rad relative to the global coordinate system and it has a value of 78 MPa. In addition to this result also the side ring of the cage is effected by higher stresses.

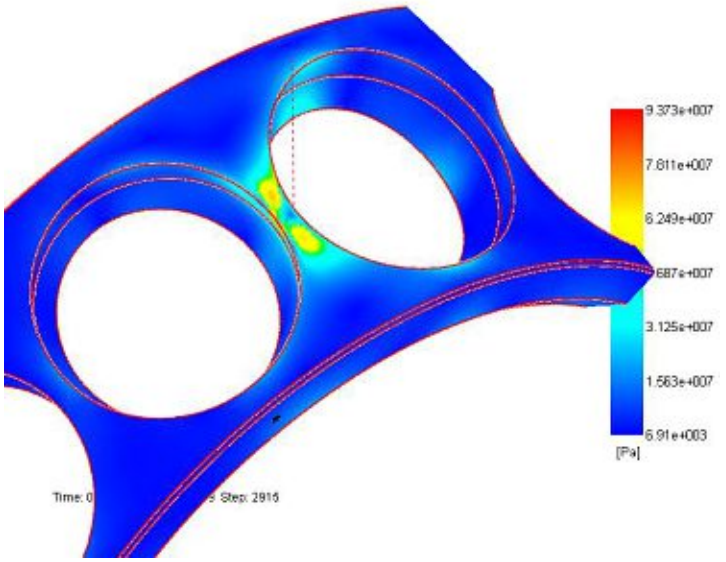

Figure 37: Cage segment with maximum v. Mises stress

Another useful post-processor software tool included in the BEAST toolbox is ViewBEAST. This program allows the user to plot a big number of results obtained from simulation. All the plots presented in the previous sections 3.2.10-3.2.12 were also generated with the software tool ViewBEAST, but to be able to plot structural stresses as a function of time or position, the user has to define so called flexible coordinate systems which define the center of an influence radius in the model. The influence radius is a user defined spherical volume in which parameters are measured and written out. These flexible coordinate systems are connected to the body, so the distances of the center of the flexible coordinate system relative to the bodies center of mass are constant. In these flexible coordinate systems the user can define a sphere with arbitrary radius. BEAST then writes out the average of the output parameters from all of the nodes included in the sphere or from nodes on surfaces only, depending on the settings the user defined in the pre-processor BEAUTY. Because of this, the user has to place the flexible coordinate systems with care and choose a proper radius to get accurate results. In this model, $2 \cdot (5 \cdot 19) = 190$ influence radii are defined on the front surface of pocket 1 respectively on the back surface of pocket 2. Figure 38 shows the arrangement of the influence radii used in the model. The influence radii are also necessary to tell BEAST where refinement of the mesh is wanted. In this simulation a radius of 1 mm was chosen as a compromise of accuracy, included nodes and output-data.

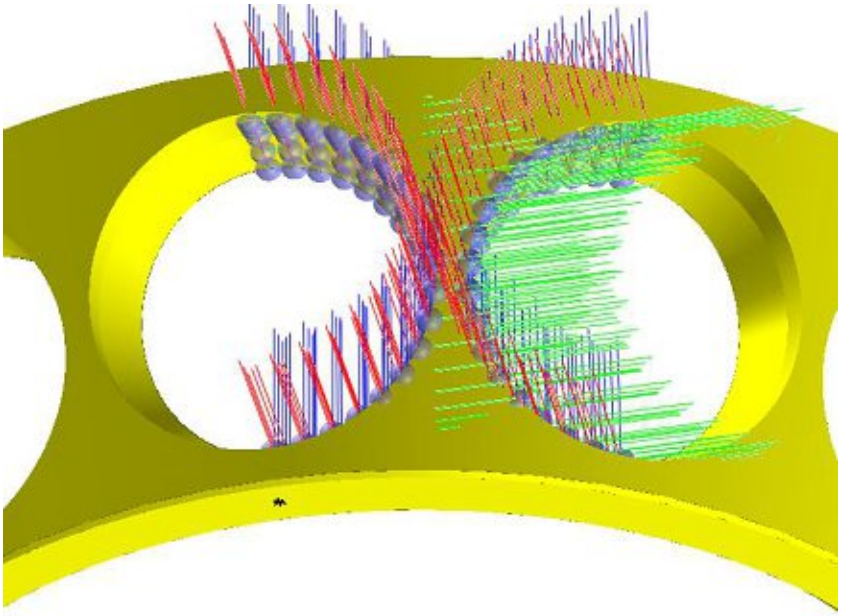

Figure 38: Arrangement of the used flexible coordinate systems in the cage pockets

In Figure 39 and Figure 40 the scalar structural stress value according to v. Mises effective stress

$$\sigma_V = \sqrt{3J_2} \tag{11}$$

with the second deviatoric stress invariant

$$J_2 = \frac{(\sigma_{11} - \sigma_{22})^2 + (\sigma_{22} - \sigma_{33})^2 + (\sigma_{33} - \sigma_{11})^2}{6} + \sigma_{12}^2 + \sigma_{23}^2 + \sigma_{31}^2 \tag{12}$$

is pictured next to the associated flexible coordinate system. The time respectively position dependent structural stresses are plotted for ten different flexible coordinate systems, including the one with the highest stress demands. Five flexible coordinate systems are located at the front side of cage pocket 1 and the other five coordinate systems are located at the back side of cage pocket 2. Every influence radius has a radius of 1 mm and all nodes inside this sphere and on the surface of the cage are used to calculate a mean value of the v. Mises stresses.

Acoording to Figures 39-40, the maximum v. Mises stress occurs at the back side of the cage pocket with a value of 8e7 Pa.

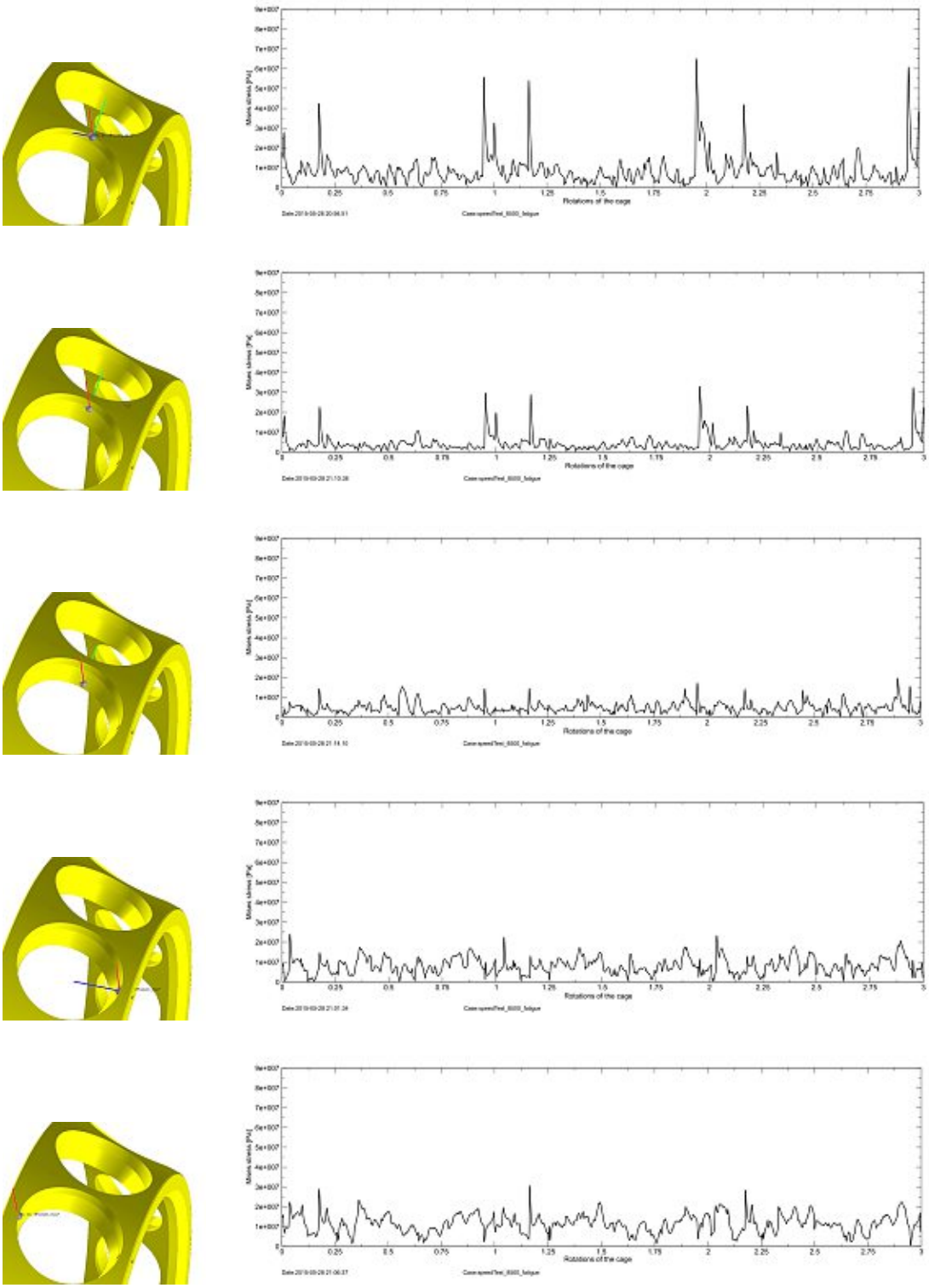

Figure 39: Flexible coordinate systems at the front side of the cage pocket and dedicated v. Mises stresses

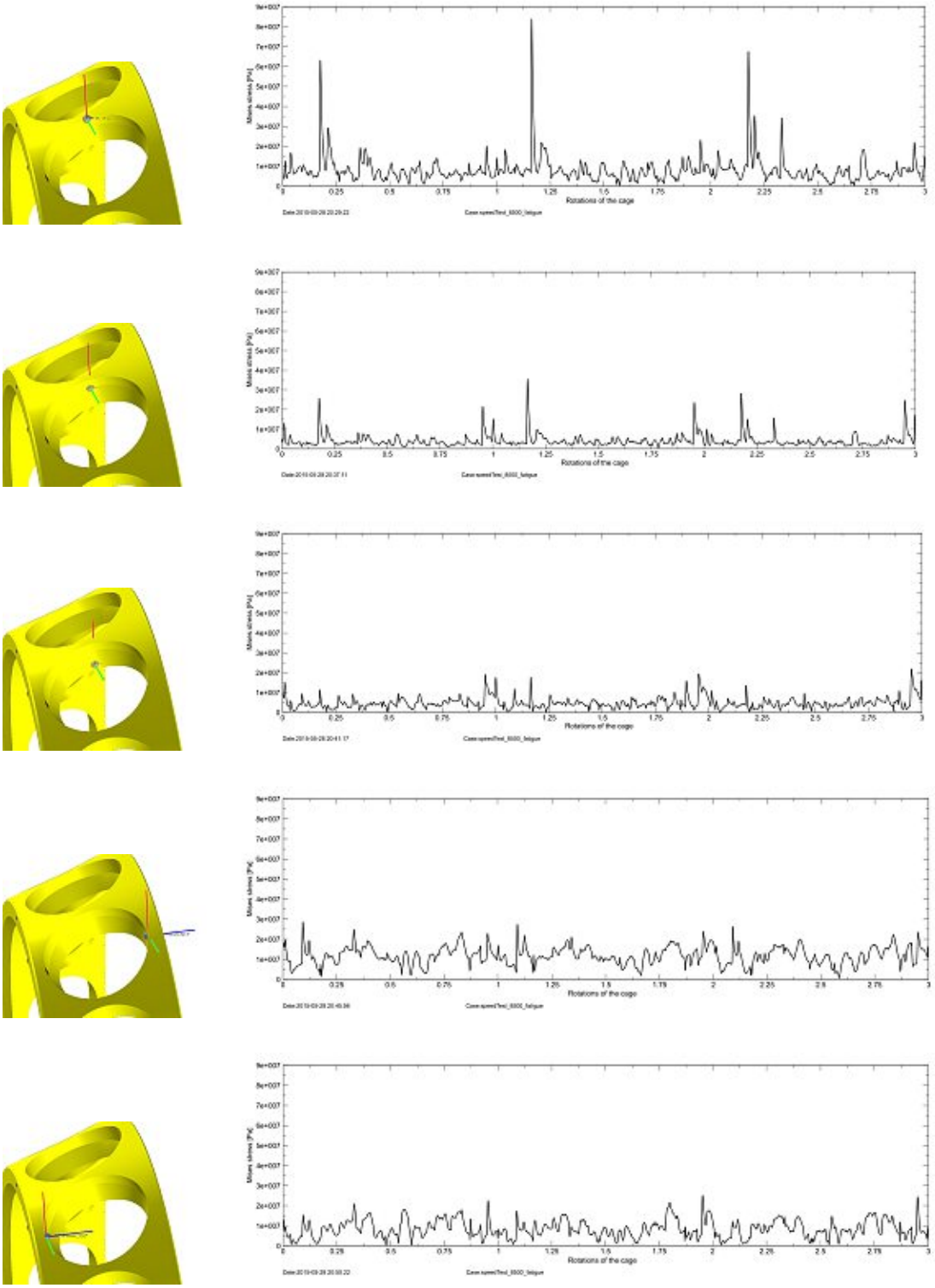

Figure 40: Flexible coordinate systems at the back side of the cage pocket and dedicated v. Mises stresses

3.2.14 Deformation

The post-processor BEAUTY provides different possibilities to present the absolute deformations in a visual way. The deformation can be magnified in a range of values between 1-10000. Another way to visualize the deformations is to use a color bar similar to the one used in section 3.2.13 to visualize the global stresses. In Figure 41 the absolute deformations of the cage are presented for four different time steps - similar to the one in Figure 36 - in both ways and also in a combined version. The chosen magnify is 250. From this illustration one can see that the deformation is a very dynamic process. The cage gets widened several times per rotation.

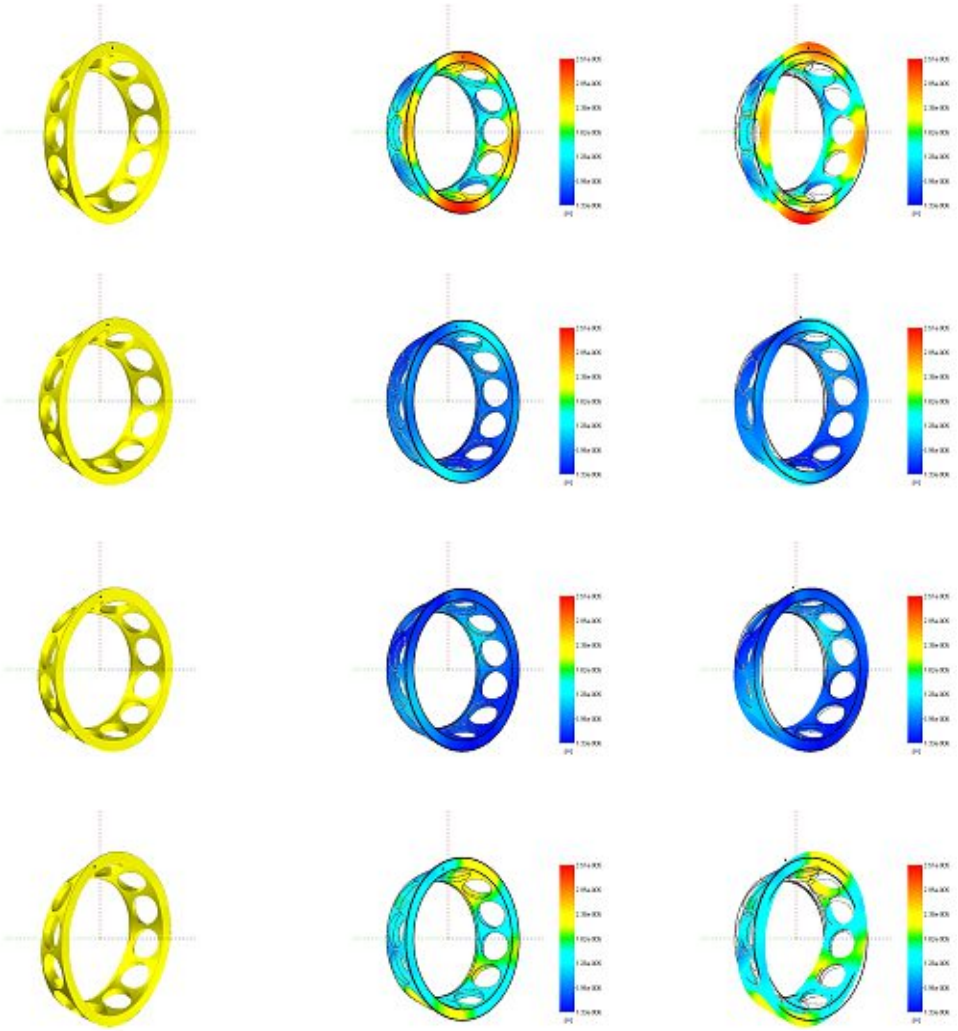

Figure 41: Deformations of the cage for case A

More interesting than the global deformation is the local deformation in the refined part of the cage between cage pockets 1 and 2. In Figure 42 the most extreme deformation occurring during a whole rotation of the cage is shown. The chosen magnify is 250 and the position is identical with the one in Figure 37 where the v. Mises stresses are investigated.

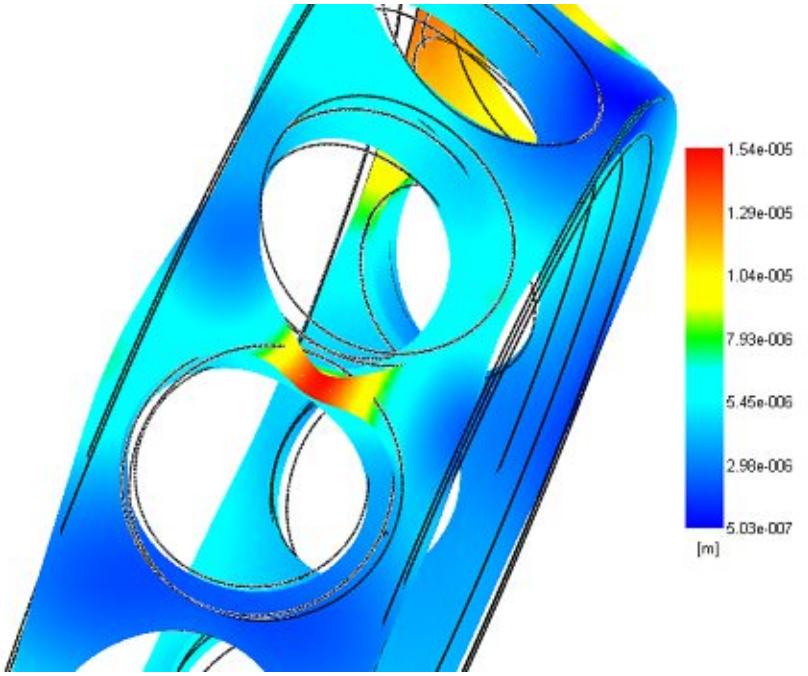

Figure 42: Cage segment with maximum deformation

3.2.15 Frictional moment

Rolling bearings are joints which connect rotating parts and transfer forces. Because of contacting elements in the bearing, viscous effects of the lubricant and other physical phenomena, there will always be a power loss. In order to be able to estimate the dissipated energy in a bearing, the frictional moment can be calculated in BEAST. Since the energy is transformed in heat, this frictional moment is also interesting for thermal observations. Figure 43 shows the total power loss in the bearing which is in the range of -1415 W - -1340 W.

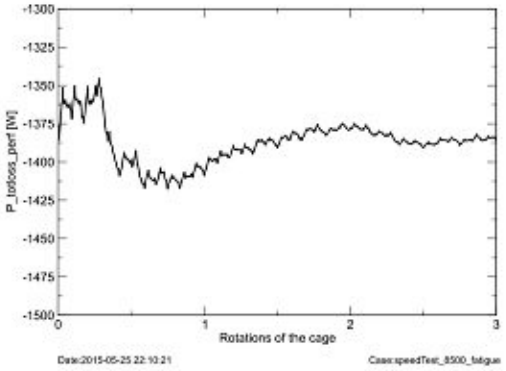

Figure 43: Power loss during simulation time

3.2.16 Modal analysis

In the multi body simulation tool BEAST a modal analysis for the flexible components can be performed. This analysis is useful to detect the critical frequencies which should be avoid during operation. In Figure 44 the natural vibration modes of the cage according to the first six eigenfrequencies are given.

Figure 44: Calculated deformation modes of the lowest six eigen frequencies

With these results one can convey worst case operating conditions in which strong vibration may appear.

According to Figure 30 the cage is effected by 12 impacts caused by the balls during one cage rotation. For this reason a critical rotational speed of the cage can be calculated by the following equation

$$\omega_{cage_{krit}} = \frac{\omega_{krit}}{n_{balls}}, \tag{13}$$

where $\omega_{cage_{krit}}$ is the critical angular velocity of the cage, ω_{krit} is the calculated eigenfrequency and n_{balls} is the number of the balls.

Because the angular velocity of the inner ring is the input parameter in BEAST, the estimation

$$\omega_{IR_{krit}} = \frac{2 \cdot d_m}{d_m - 2 \cdot r_{Ball} \cdot \cos\alpha} \cdot \omega_{cage_{krit}} = 2.5 \cdot \omega_{cage_{krit}} \tag{14}$$

can be used to calculate a critical operation angular velocity of the bearing. In Table 7 the approximated values of the critical angular velocities for the six eigenfrequencies are given.

eigen-frequency	crit. ang. velocity of the cage	crit. ang. velocity of the inner ring
921.17 Hz	4605.85 rpm	11514.63 rpm
921.23 Hz	4606.15 rpm	11515.38 rpm
1300.29 Hz	6501.45 rpm	16253.63 rpm
1301.28 Hz	6506.40 rpm	16266.00 rpm
2561.02 Hz	12805.10 rpm	32012.75 rpm
2561.54 Hz	12807.70 rpm	32019.25 rpm

Table 7: Calculated critical operating conditions

All of these critical angular velocities are higher than the operating velocity. This means that none of these frequencies has to be passed when accelerating the bearing or in the running out phase of the bearing.

4 Structural Fatigue

In BEAST a new approach to high cycle fatigue was developed. The method is able to deal with random stress signals calculated in any influence radius. However a good quality of the fatigue damage calculation requires also accurate material data, which is not always available. For this reason it is difficult to predict the life time of a component by simulation only. In order to test the performance of BEAST, a fatigue calculation was performed and presented in this section.

A possible approach to describe the physical nature of the high cycle fatigue damage is to hypothesize that it is generally governed by the shear stress amplitude combined with the normal stress acting on a plane.

BEAST uses the user defined flexible coordinate systems to calculate fatigue. The stress history in these influence radii is decomposed in stress reversals. The algorithm detect half or full reversals and the associated fatigue damage is accumulated in the investigated influence radius. Also a maximum fatigue damage factor is updated in the specific influence radius.

The output of the fatigue calculation - the fatigue damage - is a unit-less value. It can be interpreted as equal 1/N, where N is the total number of reversals that a point of the body can withstand without crack nucleation. High cycle fatigue means that the mechanical component withstands 10^3 load cycles before fatigue failure occurs. The total damage d after k reversals can then be calculated with the Miners rule

$$d = \sum_{i}^{k} \frac{1}{N_i}, \tag{15}$$

where N_i is the number of reversals that the point can withstand for the load amplitude i.

A further output parameter is the maximum damage factor. This indicator is defined as the ratio of the maximum equivalent stress amplitude to the fatigue stress limit of the material. For materials which feature an endurance limit (e.g. steels), a maximum damage factor lower 1 means a theoretically infinite life in this fatigue model.

In the actual BEAST Version 12.0, four different fatigue models are included, which are:

- the Sines' criterion [3],[12],
- the Findley's criterion [3],[12],

- the Dang Van's criterion [3],[12] and
- the Uniaxial fatigue criterion [3].

The main difference between the fatigue models is the method of the computation of the fatigue damage respectively the maximum damage factor.

In this work only the uniaxial damage criterion is used. For this reason a short overview of the mathematical background is also given in this work in order to get an idea of how the input parameters influence the results.

4.1 Uniaxial fatigue criterion [3]

The equivalent stress amplitude for uni-axial stress states for this model is computed in the following way:

$$\beta_U = \frac{\Delta\sigma_I}{2} K_r \left(1 - \frac{K_r \overline{\sigma_I} + \sigma_{res}}{\sigma_{UTS}}\right)^{-1}, \tag{16}$$

where $\frac{\Delta\sigma_I}{2}$ is the amplitude of the reversal of the maximum principal stress, $\overline{\sigma_I}$ is the mean value of the maximum principal stress during one reversal, σ_{res} is the residual stress on the surface, σ_{UTS} is the ultimate tensile stress of the material and K_r is the notch sensitivity factor which is computed in the following way:

$$K_r = \sqrt{\frac{a_0}{a_0 + R_a} + \frac{4a_0}{R}}. \tag{17}$$

In equation (17) the variable R_a describes the surface roughness and R is the minimum local radius of curvature. a_0 is the so called intrinsic crack size which is defined as

$$a_0 = \frac{1}{\pi}\left(\frac{\Delta K_{th}}{1.12\sigma_{lim}}\right). \tag{18}$$

As can be seen in equation (18), the intrinsic crack size is a function of the endurance limit σ_{lim} and the threshold stress intensity factor range ΔK_{th} which are both input parameters.

4.2 Stress life curve [12]

To be able to calculate fatigue of the cage, an accurate material law is needed. The Basquin type S-N curve is a graph computed from the material properties. It pictures the number of load cycles till failure as a function of the stress amplitude. Usually this curve is obtained by bending experiments with zero mean stress on polished specimens. With the structural fatigue limit due to bending σ_{lim} and the ultimate tensile strength σ_{UTS} of the cage material given in Table 4 the S-N curve shown in Figure 45 was generated and used for fatigue calculation. Since it is very difficult to get reliable material parameters, the results of a fatigue simulation should always be observed in a critical way.

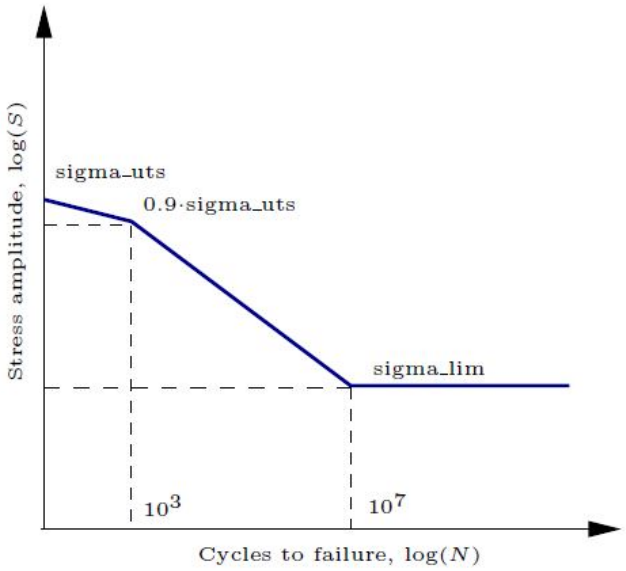

Figure 45: Simplified S-N curve constructed for the cage material [12]

4.3 BEAST structural fatigue damage and life assessment

To perform a structural fatigue damage calculation of the cage of the Angular Contact Ball Bearing 7313, the model from section 3.2 is used as basis for the input file but was adapted in the following way: The angular velocity of the inner ring was increased to a value of 14000 rpm and also the forces were adjusted to a higher numerical value. The axial load in this simulation is set to 7150 N and the radial one is 5000 N. Both forces are acting on the outer ring. With these extreme parameters, a critical dynamic situation should be reproduced in the simulation.

In the equations (16)-(18) material parameters, tribologic parameters and also a residual stress value occur. The material parameters are given in Table 4 but to set the tribologic parameters and the residual stress value, some careful considerations are necessary. Since the production of the cage influence the inherent stress condition, this value is different depending on the manufacturing method. In this simulation we consider a cage with milled cage pockets. This process generates a positive residual stress in circumferential direction, which means that the residual stress component in the cage pocket is a tensile stress. Since it is very hard to measure the exact value, a range of 50 MPa to 150 MPa is used to include this effect. In the BEAST model the residual stress is defined at the surfaces of the cage pockets and the two surfaces on the outer side respectively the inner side of the cage, because these surfaces are relevant for the used influence radii (Figure 46). The surface roughness influences the notch sensitivity factor (8). This value is also set in a bandwidth of 1.25 μm, which is the specification of the producer, to an increased value of 3.75 μm at surface elements like the cage pocket surfaces, which are machined in a careful way, to investigate the influence of the surface roughness. For all other surfaces a roughness of 5 μm was chosen. The reason for the higher values of the surface roughness used in the simulation is, that normally the surface roughness is seen as a global parameter. This means that the local roughness can maybe differ from this specification. The residual stress and the surface roughness can be edited in BEAUTY individually for every surface.

In order to get an idea of the influence of the two varied parameters - surface roughness and residual stress due to manufacturing - nine simulations were performed. The case with the surface roughness parameter of 3.75 μm and a residual stress of 50 MPa is reviewed in a detailed way. In Figures 47-55 the main results of all performed simulations are represented. From these results the positive or negative influence of the quality of the surface in the cage pockets and the residual stress due to manufacturing technology can be derived and a good relative comparison is possible.

As a first step of the fatigue assessment a pilot run was performed. The results of

this first run help to identify the areas in which fatigue may occur and where the influence radii, in which fatigue calculations are performed, should be placed. Referring to the results of the pilot run, the ten used influence radii were located at the front side of cage pocket 1 in the area of the edge of the cage pocket and the outer surface of the cage, as shown in Figure 46.

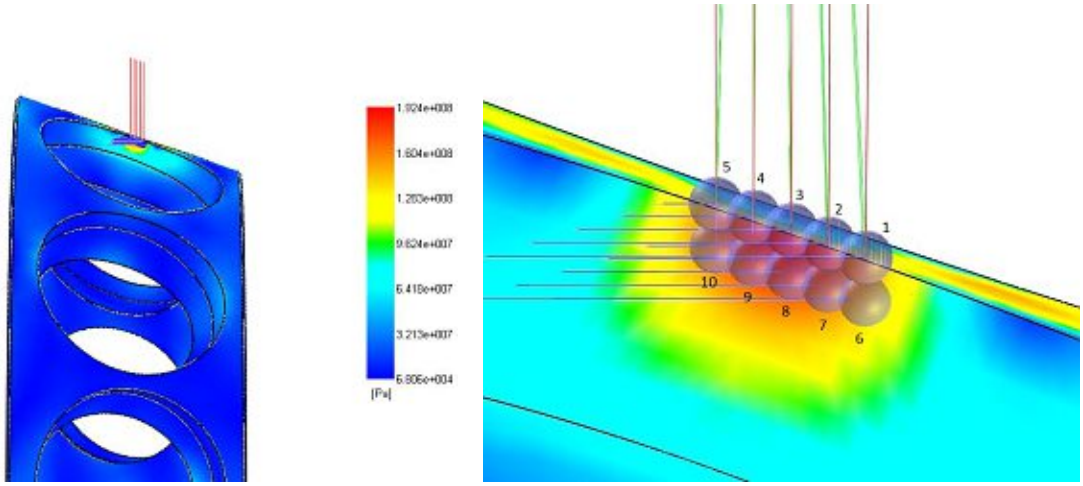

Figure 46: Location of the influence radii with fatigue calculation activated

To be able to investigate the area of interest, ten influence radii with a radius of 0.3 mm were used. The chosen radius is a compromise of accuracy and number of included nodes.

With this updated input-file the simulation including a fatigue assessment was started. The total simulation time was set to $t_{sim} = 35 \cdot t_{rot}$. Because the transient start-up phase should not be considered in the fatigue calculation, the start time for writing out data was set to $20 \cdot t_{rot}$ because after this period of time, the dynamic system reaches an approximately stationary state. This means that a time interval of $15 \cdot t_{rot} = 15 \cdot \frac{2\pi}{\omega_{max}} = 0.0643$ s is used to determine structural fatigue. Within this time interval the algorithm searches for sub-intervals in which stress reversals of the specific stress factor β (16) occur. After every detected stress reversal, all of the damage factors are updated.

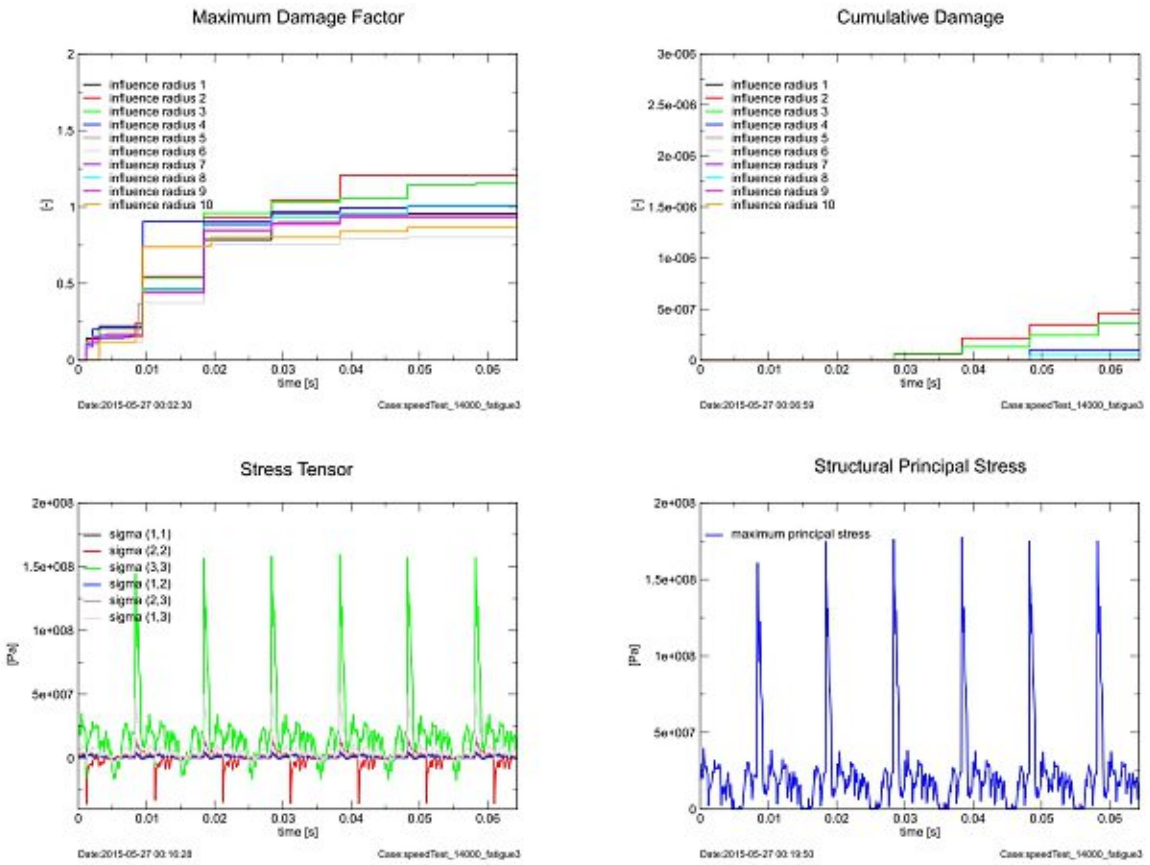

Figure 47: Main results of the structural fatigue calculation for the influence radius 2

Figure 47 gives an overview of the results of the fatigue calculation performed in influence radius 2 (Figure 46). The maximum damage factor is the maximum equivalent stress, computed by the uniaxial fatigue criterion, normalized on σ_{lim} of the material. When this value exceed the threshold, defined as 1, the load causes damage and the cumulative damage factor is increasing. For the actual model with a cage pocket surface roughness of 3.75 μm and a residual stress of 50 MPa, the cumulative damage reaches a value of 4.625e-7 after the simulation time $15 \cdot t_{rot} = 0.0643$ s in influence radius 2. According to the theory of the uniaxial fatigue damage criterion implemented in BEAST, the cage is predicted to fail at a point, when the accumulated damage reaches the value 1. In order to prognosticate the absolute fatigue life time of the cage of this Angular Contact Ball Bearing, loaded with the given operating conditions, the following formula can be used, if it can be assumed that the damage accumulated in the investigated time is similar to the damage accumulated during any other time interval of equal length during the

component life time:

$$\frac{d}{t} = \frac{1}{T}. \tag{19}$$

In this extrapolation, the variable d is the cumulative damage according to the uniaxial fatigue criterion, t is the simulation time relevant for fatigue calculation and T is the time at which the component respectively the cage is predicted to fail at the investigated point.

Using the results given in Figure 47 with a cumulative damage of $d_{end} = 4.625e-7$ after a time period of 0.0643 s, we obtain that the cage is predicted to fail after a total running time of $T = \frac{15 \cdot t_{rot}}{d_{end}} = \frac{0.0643s}{4.625e-7} = 139027$ s. This is a time period of approximately 39 hours or 1.5 days.

To get a better understanding of the influence of the surface roughness on the cage pocket surfaces and the residual stress, in the following, the results of the fatigue calculation of the eight other simulations are presented. Setting the surface roughness of the cage pocket surfaces to a value of 3.75 μm and the residual stress to 150 MPa, the calculated value of the cumulative damage at the end time of the simulation is $d_{end} = 2.055e-6$. In this case, influence radius 3 is placed at the critical location concerning fatigue. Using equation (19) with simulation time $t = 15 \cdot t_{rot} = 15 \cdot 4.2857e-3$ s= 0.0643 s we obtain a component life time of 31290 s, which is approximately 9 hours (Figure 48).

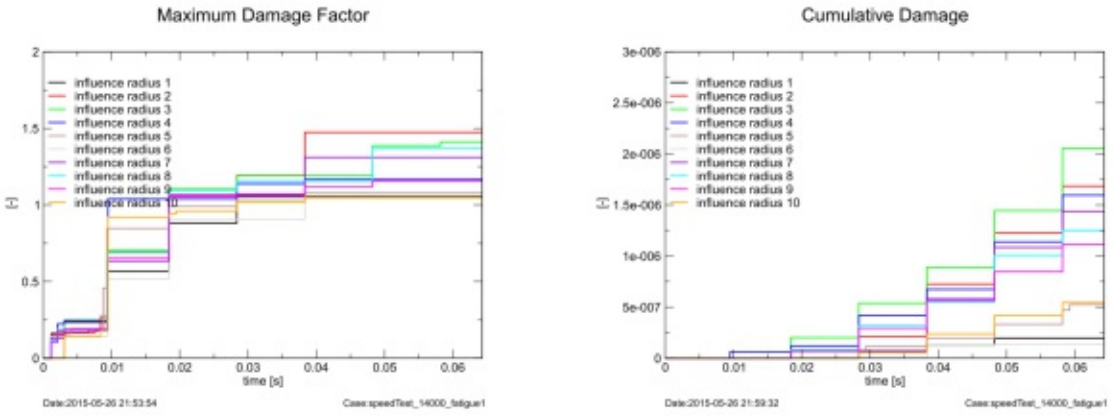

Figure 48: Main results for surface roughness 3,75 μm and residual stress 150 MPa in the cage pockets

In the next simulation, the residual stress was reduced to a value of 100 MPa. Here, equation (19) predicts a life time of the cage of 145904 s or 41 hours by using the values

presented in Figure 49, which are $t = 15 \cdot t_{rot} = 0.0643$ s and $d_{end} = 4.407e - 7$. In this case, influence radius 7 is the critical one.

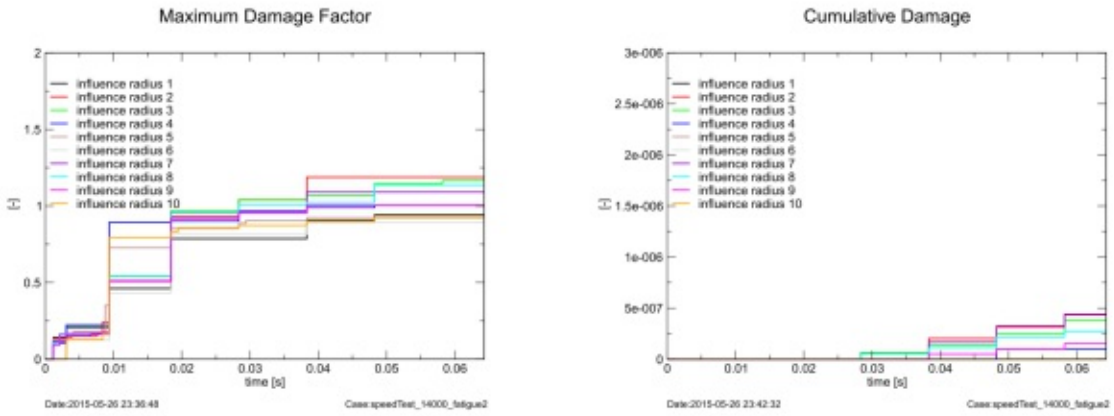

Figure 49: Main results for surface roughness 3.75 μm and residual stress 100 MPa in the cage pockets

In the following 3 simulations presented in the Figures 50-52 the surface roughness of the cage pocket surfaces is reduced to a value of 2.5 μm and the residual stress is 150 MPa, 100 MPa respectively 50 MPa.

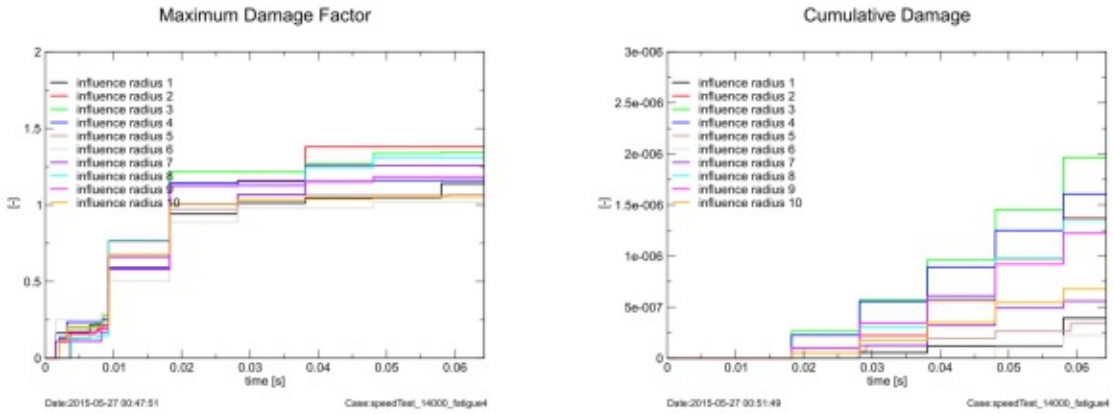

Figure 50: Main results for surface roughness 2.5 μm and residual stress 150 MPa in the cage pockets

According to Figure 50 the cumulative damage of the cage at influence radius 3 reaches

a value of $d_{end} = 1.963e - 6$ after simulation time and it will fail after a time period of 32756 s or 9 hours.

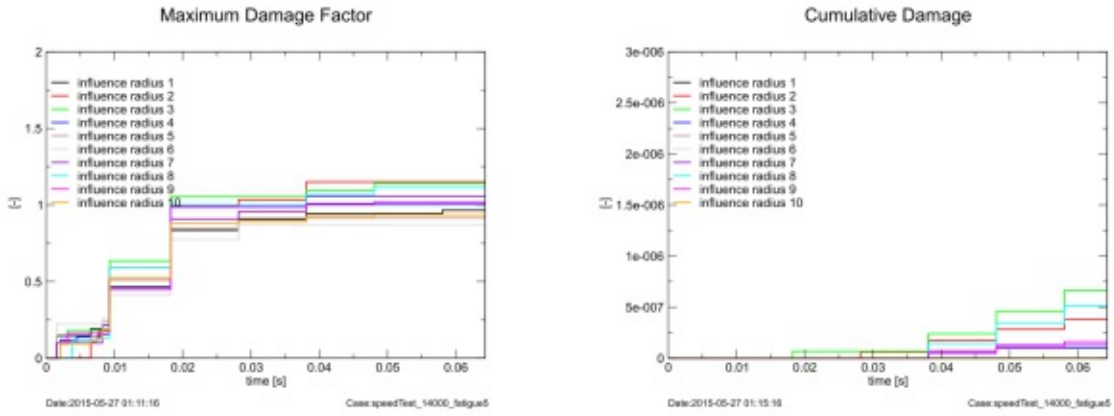

Figure 51: Main results for surface roughness 2.5 μm and residual stress 100 MPa in the cage pockets

According to Figure 51 the cumulative damage of the cage at influence radius 3 reaches a value of $d_{end} = 6.631e - 7$ after simulation time and it will fail after a time period of 96969 s or 27 hours.

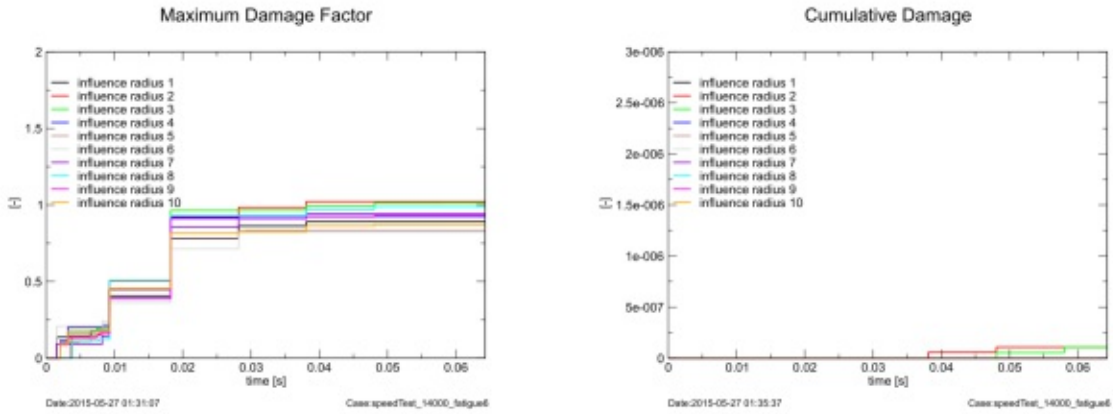

Figure 52: Main results for surface roughness 2.5 μm and residual stress 50 MPa in the cage pockets

According to Figure 52 the cumulative damage of the cage at influence radius 3 reaches a value of $d_{end} = 1.082e - 7$ after simulation time and it will fail after a time period of

594270 s or 165 hours.

The last three simulations were performed with a surface roughness of 1.25 μm. The results for the residual stresses 150 MPa, 100 MPa and 50 MPa are plotted in Figures 53-55.

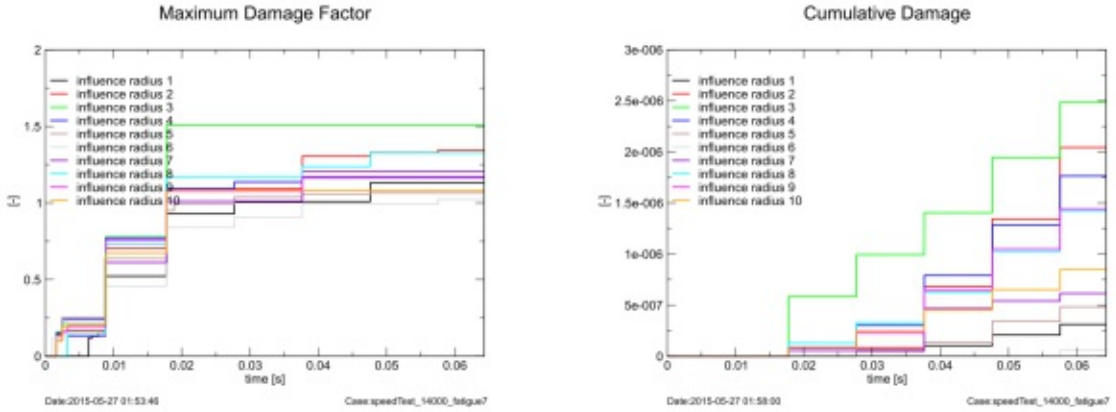

Figure 53: Main results for surface roughness 1.25 μm and residual stress 150 MPa in the cage pockets

According to Figure 53 the cumulative damage of the cage at influence radius 3 reaches a value of $d_{end} = 2.484e - 6$ after simulation time and it will fail after a time period of 25886 s or 7 hours.

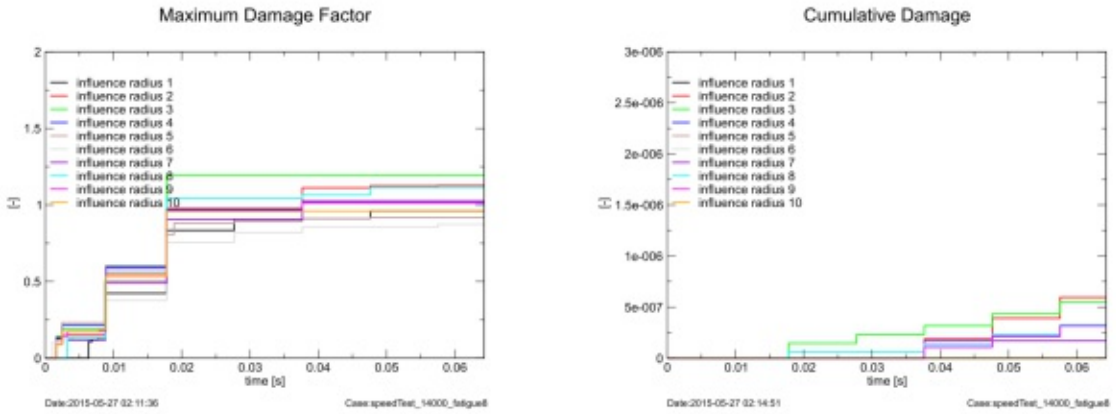

Figure 54: Main results for surface roughness 1.25 μm and residual stress 100 MPa in the cage pockets

According to Figure 54 the cumulative damage of the cage at influence radius 2 reaches a value of $d_{end} = 5.963e - 7$ after simulation time and it will fail after a time period of 107832 s or 30 hours.

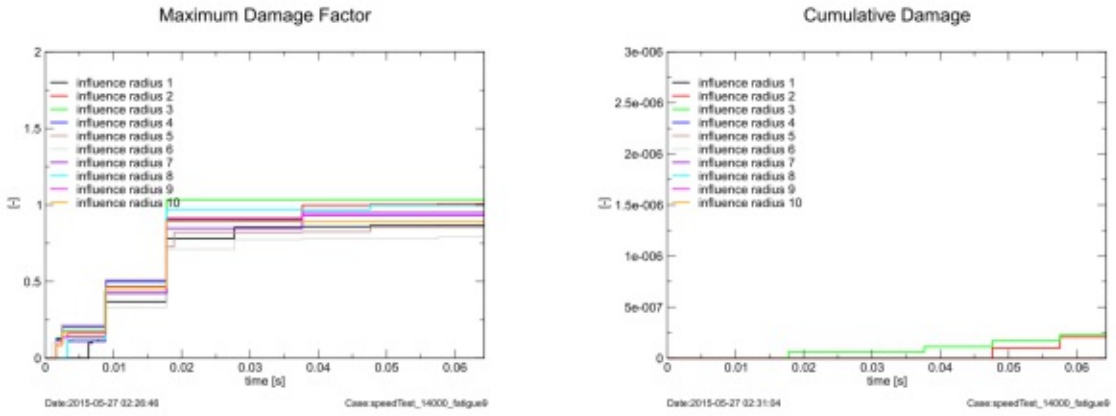

Figure 55: Main results for surface roughness 1.25 μm and residual stress 50 MPa in the cage pockets

According to Figure 55 the cumulative damage of the cage at influence radius 3 reaches a value of $d_{end} = 2.298e - 7$ after simulation time and it will fail after a time period of 279809 s or 78 hours.

In Table 8 and Figure 56 the results of the nine simulations are summarized. The influence of the residual stress is clearly identifiable. The life time of the cage increases with decreasing residual stress. On the other hand, the influence of the other varied parameter is not so clear to identify. The bandwidth of the calculated life time for different surface roughness is 126 hours for a residual stress of 50 MPa but only 14 hours for 100 MPa respectively 2 hours for 150 MPa.

	50MPa	100MPa	150MPa
1,25μm	78 h	30 h	7 h
2,5μm	165 h	27 h	9 h
3,75μm	39 h	41 h	9 h

Table 8: Life time of the cage for different parameters

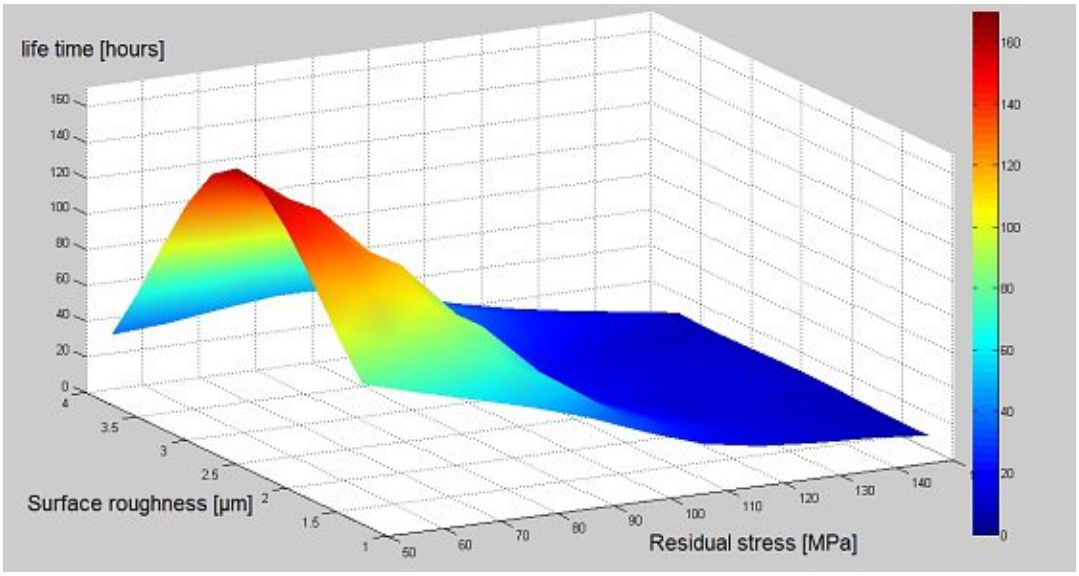

Figure 56: Influence of the residual stress and the surface roughness

The results of the parameter study presented in the previous section show, that the fatigue model is very sensitive with reference to the setting of the parameters.

5 ACBB - Dynamic Cage Robustness Test

Cages made of brass were tested in the SKF Global Testing laboratory in Steyr in bearing pairs 7313 BECBM in a specific arrangement similar to a real application. A critical operating condition with high speed and low load was simulated in the test [13]. The bearing pair was mounted in a face-to-face arrangement with a 0.127 mm shim between the outer rings. Figure 57 shows the cross-section of the testing arrangement for the dynamic cage robustness test.

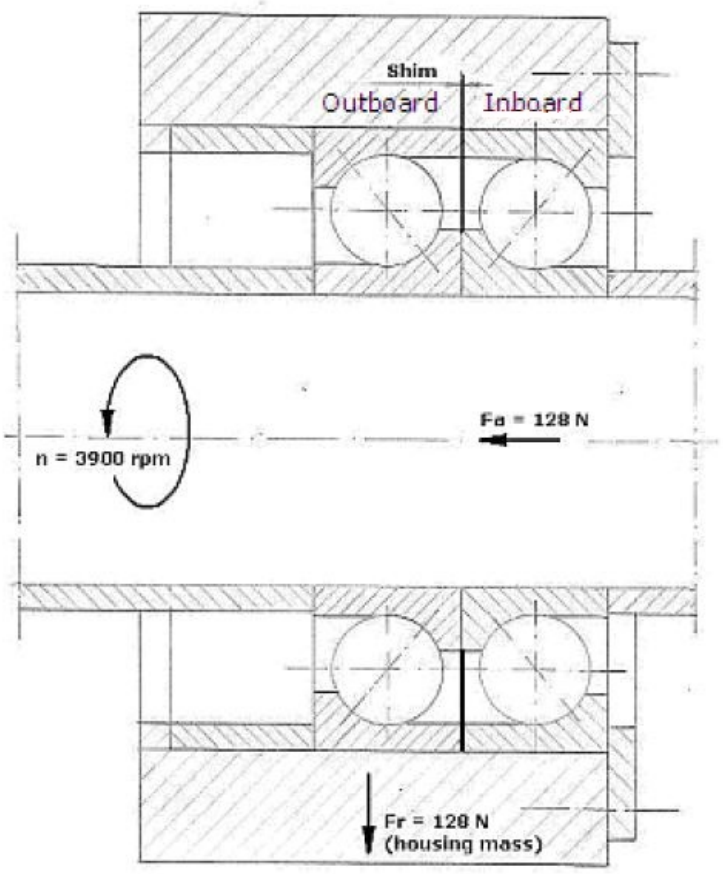

Figure 57: Cross-section of the testing arrangement [13]

5.1 Virtual Test [3],[10]

This section provides information about building a model of the Dynamic Cage Robustness Test in BEAST and the results of the simulation are presented.

5.1.1 Model building

A model of the testing arrangement presented in Figure 57 was built in the virtual test rig BEAST. The model (Figure 58) consists of 2x12 balls, two cages, one body which includes the two inner rings and one body which includes the two outer rings and the shim. Only the two cages are modeled as flexible bodies and all other parts of the arrangement are rigid bodies.

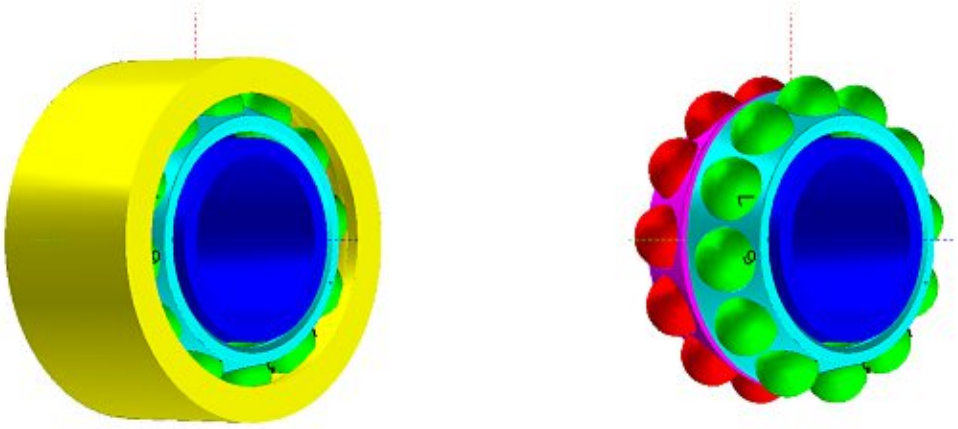

Figure 58: BEAST model with and without outer ring

5.1.2 Material parameters

The material parameters for the bearing elements are given in Table 4. The rings and the balls are made of steel and the cages are made of brass. The bearing arrangement is oil lubricated (Shell Turbo T68) and the lubricant parameters are given in Table 5.

5.1.3 Mesh parameters

In order to get results which are comparable, both of the two cages were discretized in the same way and with the same mesh parameters. The global mesh size was set to

4 mm and a deviation factor of 0.1 mm was chosen. To get more accurate results in the investigated cage pockets 1 and 2, respectively in the material between them, mesh refinement was carried out in these areas. The used flexible coordinate systems for mesh refinement are arranged at the front side of cage pocket 1 and at the back side of cage pocket 2.

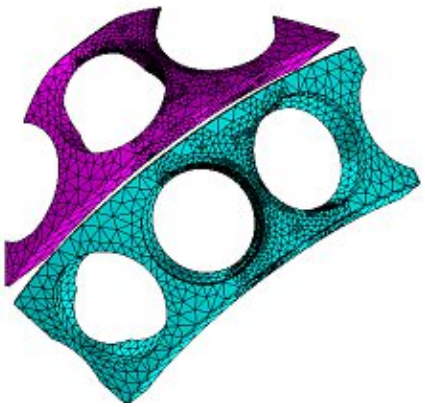

Figure 59: Meshed cages

Figure 59 shows the relevant parts of the meshed cages including the refined mesh and in Figure 60 the arrangement of the flexible coordinate systems used for mesh refinement are illustrated.

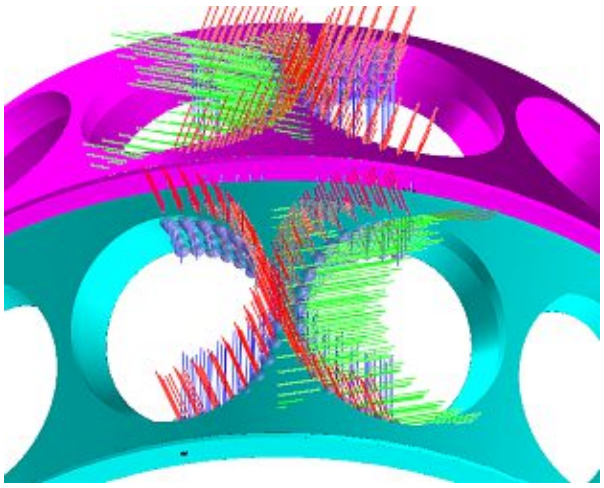

Figure 60: Arrangement of the flexible coordinate systems used for refinement

5.1.4 Model reduction

In the model the global parameters for the elastic shapes of the cages are set as follows:

- Cut off frequency is set to $1e10$ Hz. The frequencies above this limit are removed.
- Eigenmode shapes are activated. The type of constraints from active static mode shapes which is used in the eigenmodes computation is set to all constraints from static mode shapes.
- The maximum number of eigenmodes excluding the rigid body modes is set to 60.
- Centrifugal shapes with respect to the axes of inertia are included in the reduction.
- Static deformation and static load mode shapes are included in the reduction. The type of constraints from active mode shapes is set to: Free load modes and constrained deformation modes.

In the cage pocket segments where contact between the balls and the cages occur, static load mode shapes are used with an order of three for the u-direction and an order of two for the v-direction in the local coordinate systems (Figure 17) dedicated to cage pockets 1 and 2. In order to reduce computation time and disk space, the order of all other cage pocket segments is reduced to a value of one in the u-direction and v-direction.

5.1.5 Tribology

For the tribology model, the `BEAST` pre-defined parameters are used. The surface roughness of the cage pocket segments is 2.5 μm and the initial lubricant layer thickness is 1 μm. All other surfaces of the cages have a surface roughness of 5 μm. For the balls and the raceways of the rings, a value of 0.1 μm is used for surface roughness.

5.1.6 Boundary conditions

The boundary conditions are applied with the help of ties to the elements of the bearings. In the dynamic cage robustness test, the inner rings are mounted on a shaft which is rotating around its axis and the outer rings standing still. For this reason two coordinate systems were defined. The first one (ctIR) is used to define the rotation of the inner rings and the second one (ctOR) stands still and is dedicated to the outer rings.

The matrices for the tie parameters connecting the inner ring and the ctIR-coordinate system are defined as follows:

cB:bIR - SD-tie

- stiffness matrix - relative translation (in [N/m]):

$$\begin{bmatrix} -1e12 & 0 & 0 \\ 0 & -1e12 & 0 \\ 0 & 0 & -1e12 \end{bmatrix}$$

- damping matrix - relative translation (in [Ns/m]):

$$\begin{bmatrix} -1e10 & 0 & 0 \\ 0 & -1e10 & 0 \\ 0 & 0 & -1e10 \end{bmatrix}$$

- stiffness matrix - relative rotation (in [Nm]):

$$\begin{bmatrix} -1e10 & 0 & 0 \\ 0 & -1e10 & 0 \\ 0 & 0 & -1e10 \end{bmatrix}$$

- damping matrix - relative rotation (in [Nms]):

$$\begin{bmatrix} -1e8 & 0 & 0 \\ 0 & -1e8 & 0 \\ 0 & 0 & -1e8 \end{bmatrix}$$

With these parameters, the inner rings are forced to perform the movement predicted by the ctIR-coordinate system. The inner rings are therefore rotating around the global z-axis only and are fixed in all other two rotational and three translational degrees of freedom.

For the tie connecting the outer rings and the environment, following matrices are used to simulate the real boundary conditions:

cB:bOR - SD-tie

- stiffness matrix - relative translation (in [N/m]):

$$\begin{bmatrix} 0 & 0 & 0 \\ 0 & 0 & 0 \\ 0 & 0 & 0 \end{bmatrix}$$

- damping matrix - relative translation (in [Ns/m]):

$$\begin{bmatrix} 0 & 0 & 0 \\ 0 & 0 & 0 \\ 0 & 0 & 0 \end{bmatrix}$$

- stiffness matrix - relative rotation (in [Nm]):

$$\begin{bmatrix} -1e10 & 0 & 0 \\ 0 & -1e10 & 0 \\ 0 & 0 & -1e10 \end{bmatrix}$$

- damping matrix - relative rotation (in [Nms]):

$$\begin{bmatrix} -1e8 & 0 & 0 \\ 0 & -1e8 & 0 \\ 0 & 0 & -1e8 \end{bmatrix}$$

The tie between the outer rings and the environment forces the outer rings to stay free of rotation around all three axis. They are therefore only free to move translational in all three directions.

5.1.7 Time and Output

When we use the variable ω_{max} for the maximum angular velocity of the inner ring, we can calculate a characteristic time for the simulation, which represents the time of a single revolution of the inner rings:

$$t_{rot} = \frac{2\pi}{\omega_{max}}. \tag{20}$$

The chosen entire simulation time is as long as it takes the inner rings with maximum speed to perform 40 rotations

$$t_{sim} = 40 \cdot t_{rot} = 40 \frac{2\pi}{\omega_{max}}. \tag{21}$$

To realize a smooth start-up of the simulation, the forces and the speed of the inner rings are applied in form of a ramp function. The values of the forces and the speed started from zero and reach their final values after $t = 10 \cdot t_{rot}$. In order to reduce the needed disc space, only data from the steady-state is written out. The start time for writing out data is here defined as

$$t_{write} = 30 \cdot t_{rot} = 30 \frac{2\pi}{\omega_{max}}. \tag{22}$$

5.1.8 Solver settings

According to the guidelines provided from the BEAST-developer team, the SE-solver was used to perform the simulation.

5.1.9 Results of the simulation

A simulation with the operating conditions given in Table 9 was performed and the results are discussed in the following sections 5.1.10 - 5.1.13.

Speed	4 000 rpm
Axial load	128 N
Radial load	-128 N

Table 9: Operation conditions for the simulation

The forces are acting on the outer rings and the given values of the forces are relative to the global coordinate system. This means that the axial load acts in the positive z-direction and the radial load in the negative x-direction.

5.1.10 Kinematics of the bearing

Movement of the rings

In the BEAST-simulation of the Dynamic Cage Robustness Test, the bearing arrangement is modeled in a simplified way. The two inner rings are modeled as one body and also the two outer rings are modeled as a single body. Since the outer rings are mounted in the same housing and the inner rings are mounted on the same shaft, these simplification has been carried out to avoid to model the contact between the rings. But this means, that in this simulation, no relative movement between the inner rings respectively the outer rings is included. The movement of the geometric center of the outer ring is therefore equal to the movement of the housing.

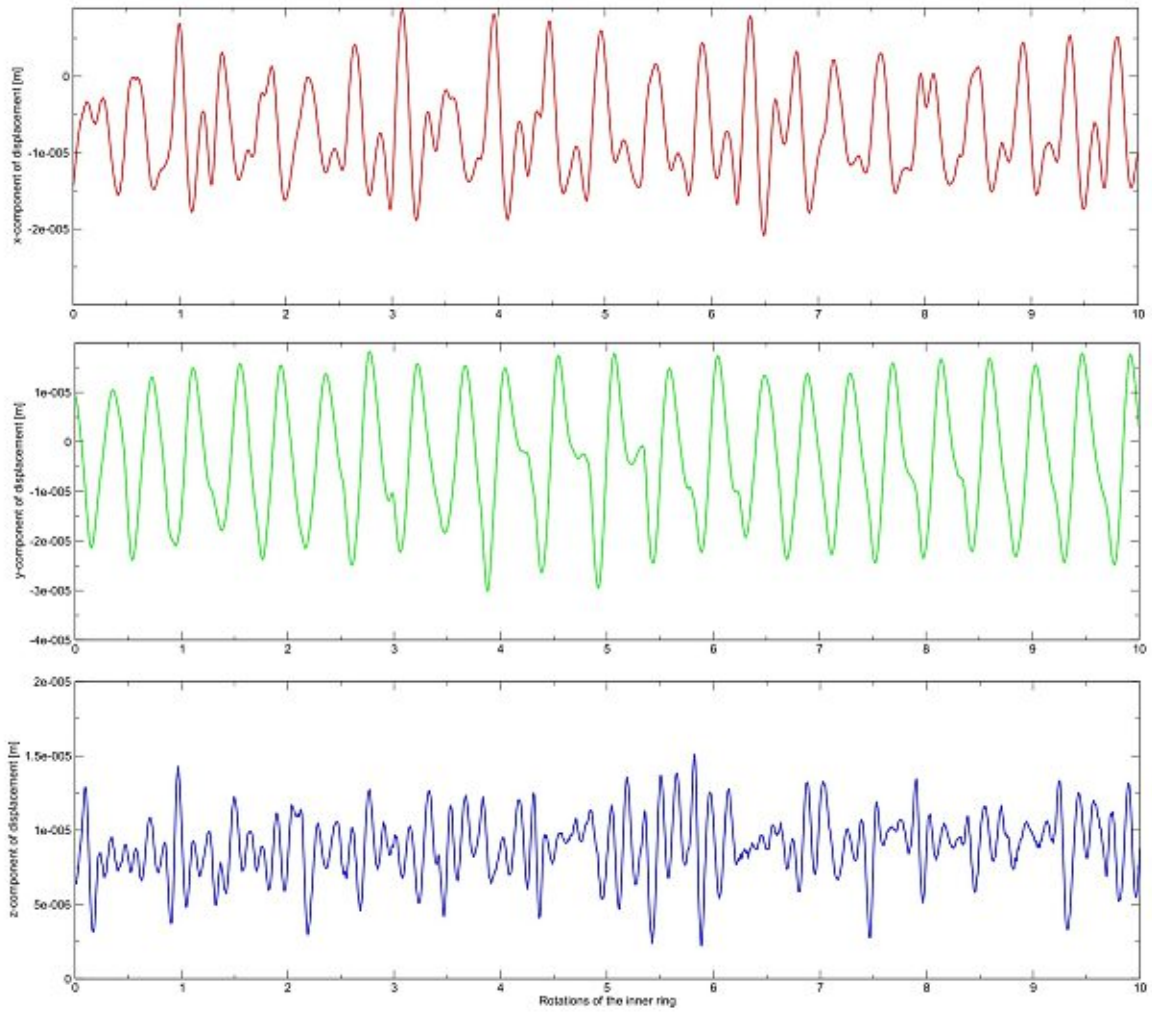

Figure 61: Movement of the outer ring

In Figure 61 the displacement of the geometrical center of the outer ring in the three directions of the global coordinate system as a function of the rotations of the inner ring (shaft) is shown. Since the outer ring is modeled as a single body and the two cages are running with slightly different speed, the resulting function is a superposition of two functions with different frequencies. The maximal occurring peak-to-peak value is 2.974e-5 m for the x-direction, 4.836e-5 m for the y-direction and 1.288e-5 m for the z-direction.

To identify the two fundamental frequencies for all directions, a Fourier transformation was performed for every component. According to these transformations we get the main frequencies (rotations of the inner ring) of 2.3 and 4.3 for the x-direction, 2.3 and 3.9 for the y-direction and 5.8 and 6.2 for the z-direction as shown in Figure 62.

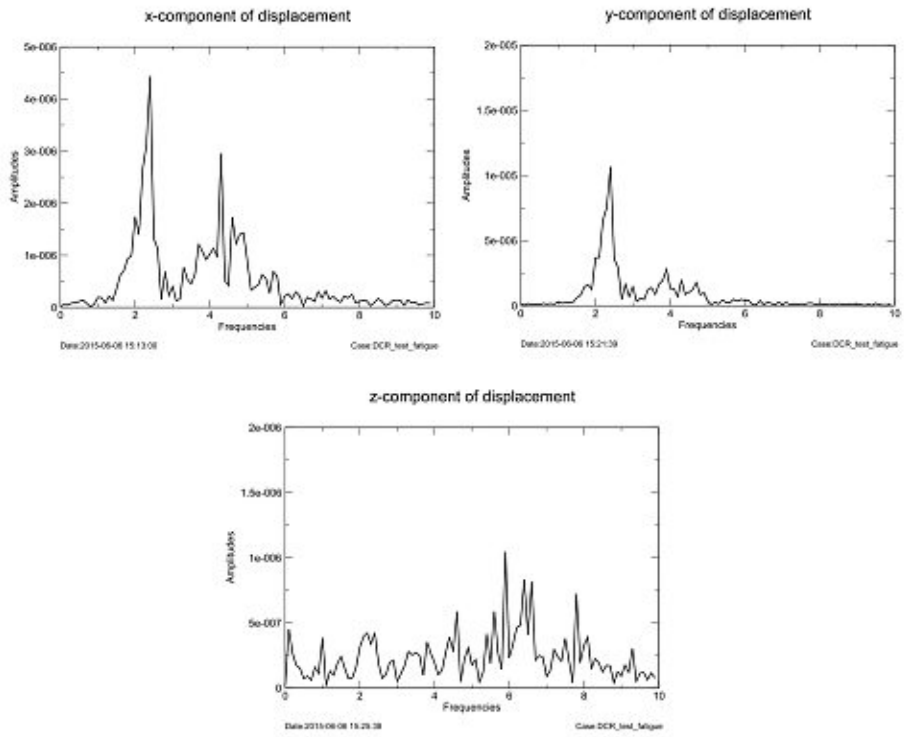

Figure 62: Amplitude spectrum of the movement of the outer ring

The translational velocity of the center of the outer ring with respect to the global coordinate system is plotted in Figure 63.

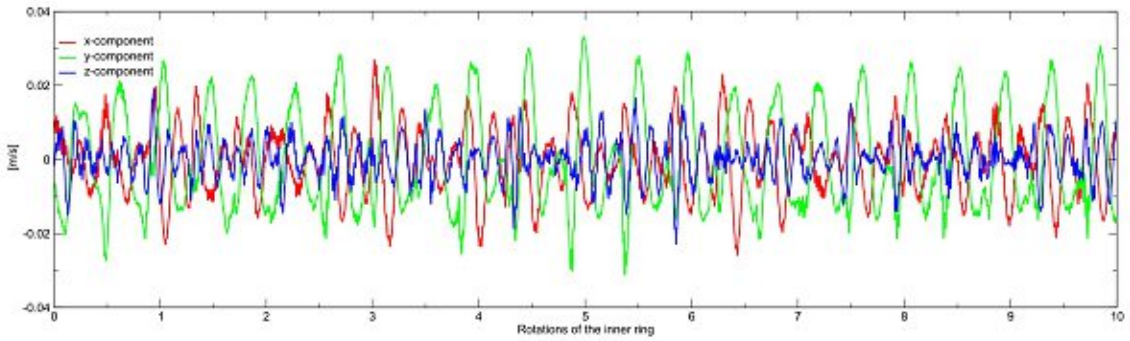

Figure 63: Translational velocity of the center of the outer ring

Also these functions show a periodicity. With the help of a Fourier transformation of every single function, one receives the two fundamental frequencies (rotations of the inner ring) of 2.3 and 4.3 for the x-direction, 2.3 and 3.9 for the y-direction and 5.9 plus 7.8 for the z-direction.

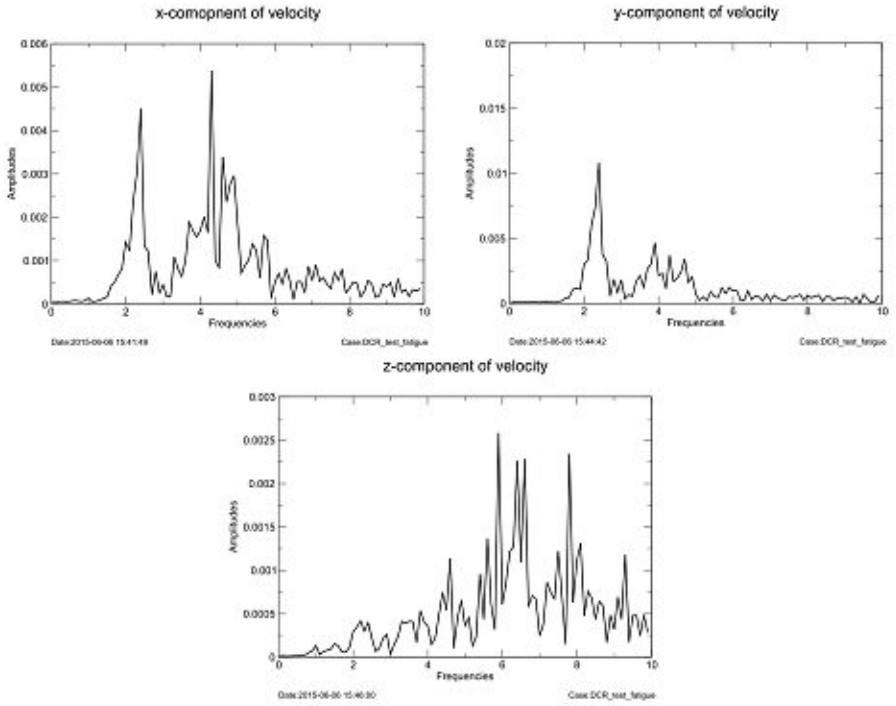

Figure 64: Amplitude spectrum of the velocity of the outer ring

Movement of the cages

Because of the face-to-face arrangement of the two Angular Contact Ball Bearings and the implemented shim between the outer rings, the axial load is not equally distributed to the two bearings. Because of this, also the velocity of the cages is different. In Figure 65 this situation is illustrated.

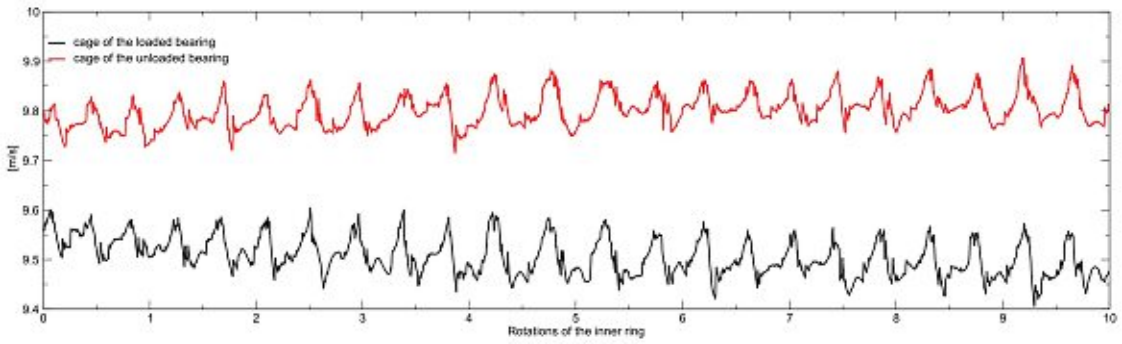

Figure 65: Circumferential speed of the cages

The cage of the unloaded bearing is rotating with a higher speed. The mean value of the rotational speed around the global z-axis of the unloaded bearing is 193.34 rad/s. The difference between the maximum speed and the minimum speed is 3.80 rad/s. The cage of the loaded bearing rotates with a mean speed of 187.52 rad/s and the peak-to-peak value of the rotational speed for this cage is 3.97 rad/s.

Since the angular velocity of the cage is mainly determined by the bearing kinematics and especially by the contact angles, the difference of the speeds of the cages can be explained by the different contact angles of the two bearings caused by the unequal loading conditions.

Because of the shim, the axial clearance of the unloaded bearing is increased. This means that the balls and the cages are able to move also in the axial direction. To investigate the consequence of this increased clearance, the rotations of the cages around the global y-axis are given in Figure 66. The cage of the loaded bearing is moving in a range of 0.0085 rad and the cage of the unloaded bearing moves in an increased range of 0.0091 rad.

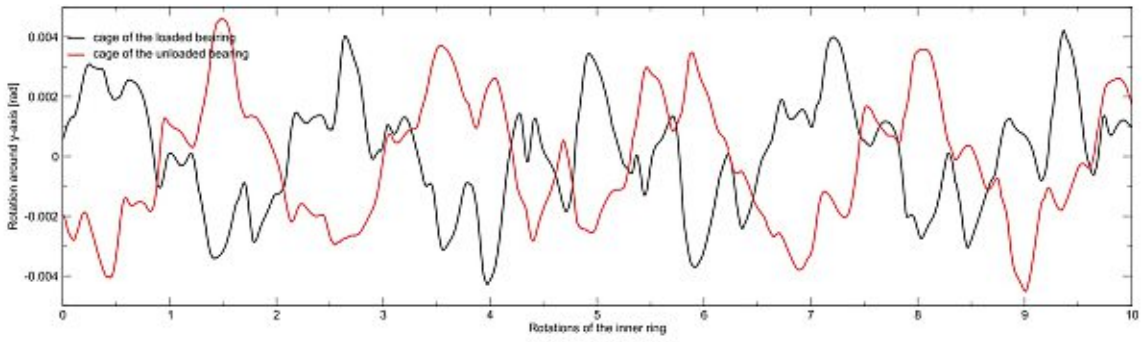

Figure 66: Rotation of the cages around the global y-axis

Movement of the balls

In this section the movement of the balls as a function of the rotation of the dedicated cage is investigated. The velocity of the geometric center of ball 1 in the loaded bearing is shown in Figure 67.

Three rotations are investigated here and the starting position of ball 1 is on the top position. The mean velocity is 9.62 m/s, but it is fluctuating between 9.42 m/s and 9.95 m/s which means a range of the velocity of 0.53 m/s.

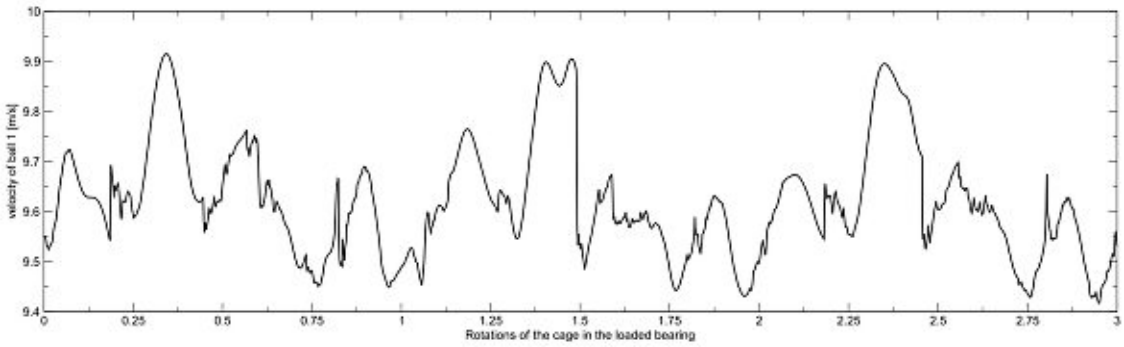

Figure 67: Velocity of the center of ball 1 in the loaded bearing

Figure 68 shows the kinematic situation of the cage and all 12 balls in the loaded bearing.

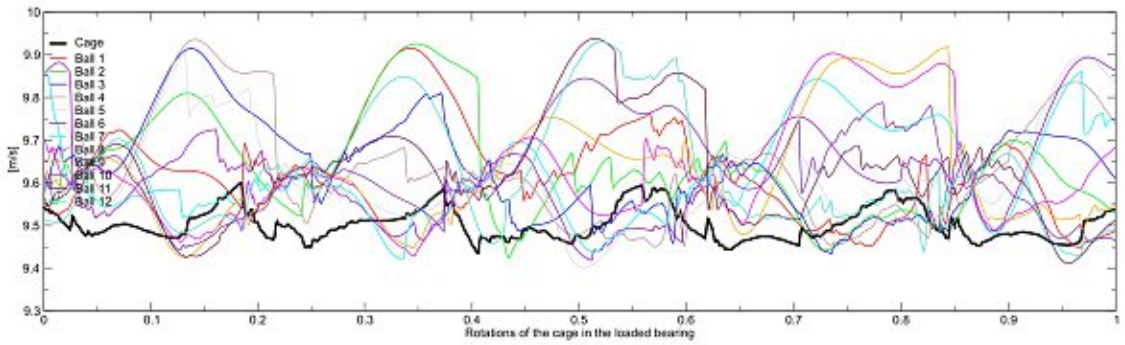

Figure 68: Relative kinematics of the cage vs. the balls in the loaded bearing

Also the velocity of the ball 1 as a function of the rotations of the cage in the unloaded bearing is investigated. According to Figure 69 the mean value of velocity is 9.93 m/s. The highest speed is 10.24 m/s and the lowest 9.73 m/s. The range of velocity is therefore 0.51 m/s. Compared to the results of the loaded bearing the mean value of the unloaded bearing is 0.62 m/s higher and the range of the value is 0.02 m/s lower.

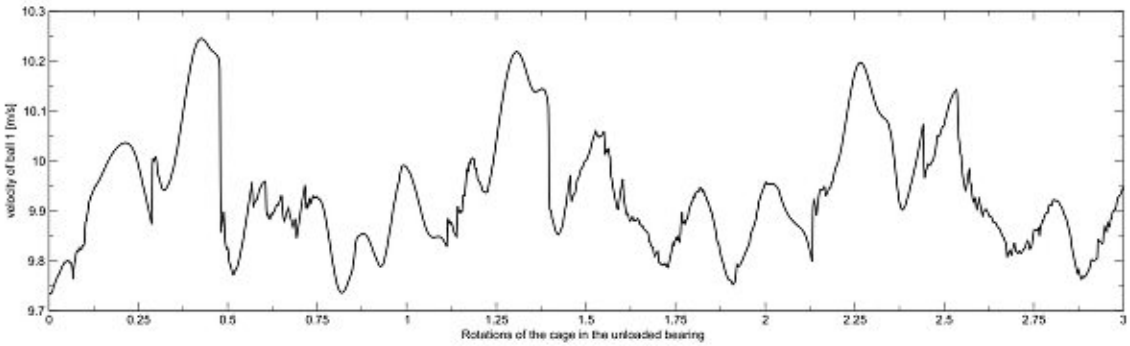

Figure 69: Velocity of the center of ball 1 in the unloaded bearing

Figure 70 shows the kinematic situation of the cage and all 12 balls in the unloaded bearing.

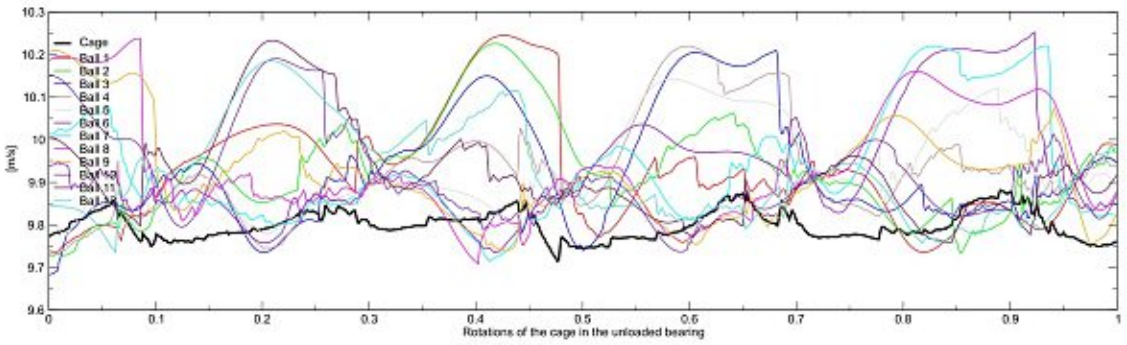

Figure 70: Relative kinematics of the cage vs. the balls in the unloaded bearing

5.1.11 Load distribution and contact forces

After the observation of the kinematic situation in the bearing arrangement, also the forces are investigated in this section. At first the load distribution of the loaded bearing is shown in Figure 71. The vector plot shows the direction of the forces acting between the balls and the inner ring respectively the outer ring in the start position.

The magnitude of the force acting between the inner ring and the ball 1 is fluctuating between 317.30 N maximum force and 31.04 N minimum force. Three significant fluctuations of the contact force occurring at a position of the cage of 0.2, 0.4 respectively 0.8 cage rotations. The fluctuations, especially at 0.2 and 0.8, seem to be connected to the changeover between the loaded and the unloaded zone.

According to Figure 71 the magnitude of the contact force acting between the ball 1 and the outer ring is fluctuating between a maximum value of 439.49 N and a minimum value of 100.57 N. Also in this case three significant fluctuations of the contact force are occurring, which are identical to the positions given above.

The load distribution in the unloaded bearing is given in Figure 72. On the top of the picture, the direction of the contact forces acting between the 12 balls and the inner ring respectively the outer ring is shown in form of vectors.

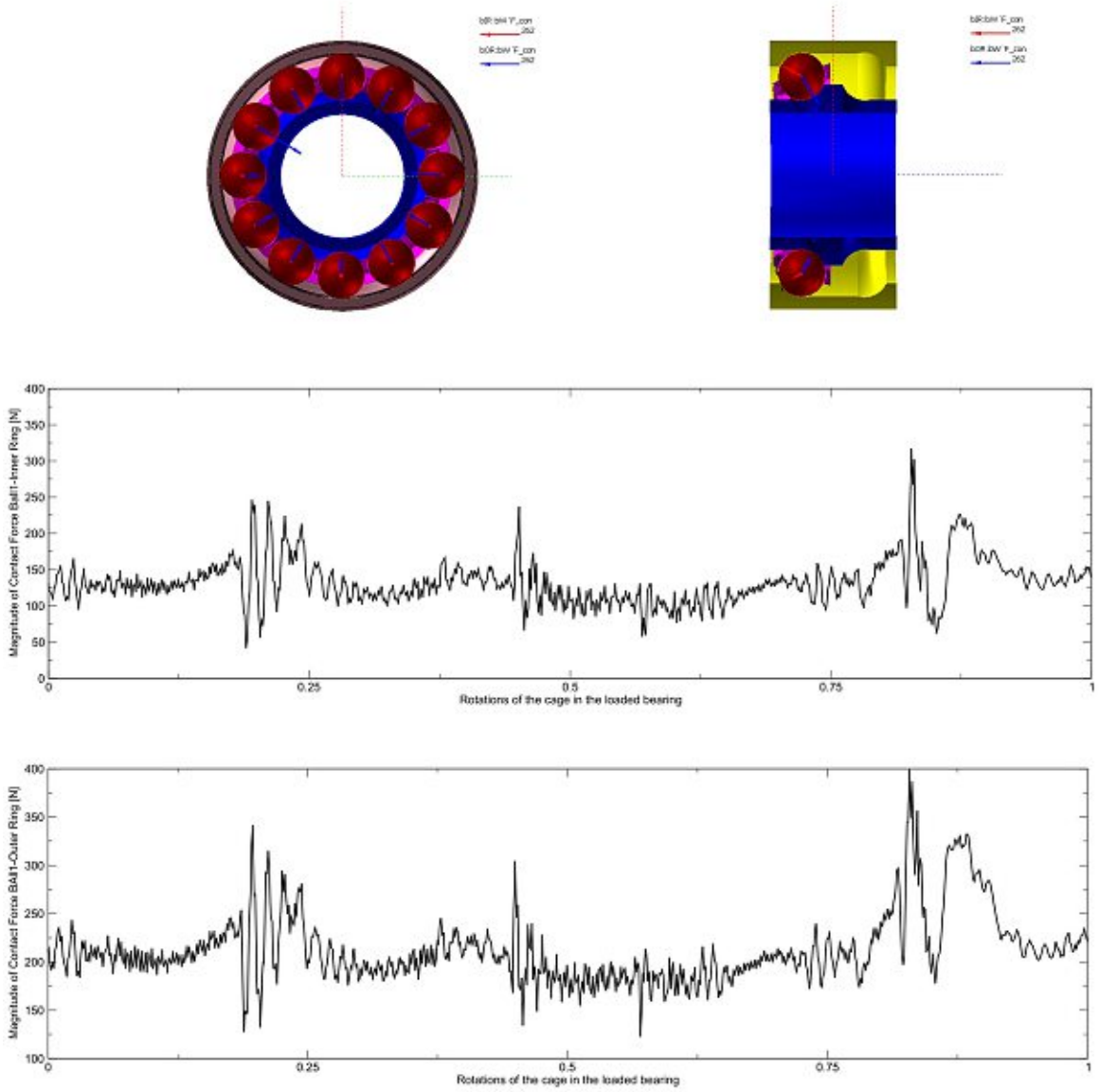

Figure 71: Load distribution in the loaded bearing

In contrast to the loaded bearing, the contact force acting between the inner ring and the ball 1 does not show such significant fluctuation as the loaded bearing does. The maximum value of the contact force is 261.55 N and the minimum value is 11.92 N.

Also the magnitude of the contact force acting between the ball 1 and the outer ring is more constant than the one acting in the loaded bearing. The maximum value of the

contact force is 367.39 N and the minimum force is 132.88 N. A comparison of Figure 71 and Figure 72 approves that the two bearings are loaded differently.

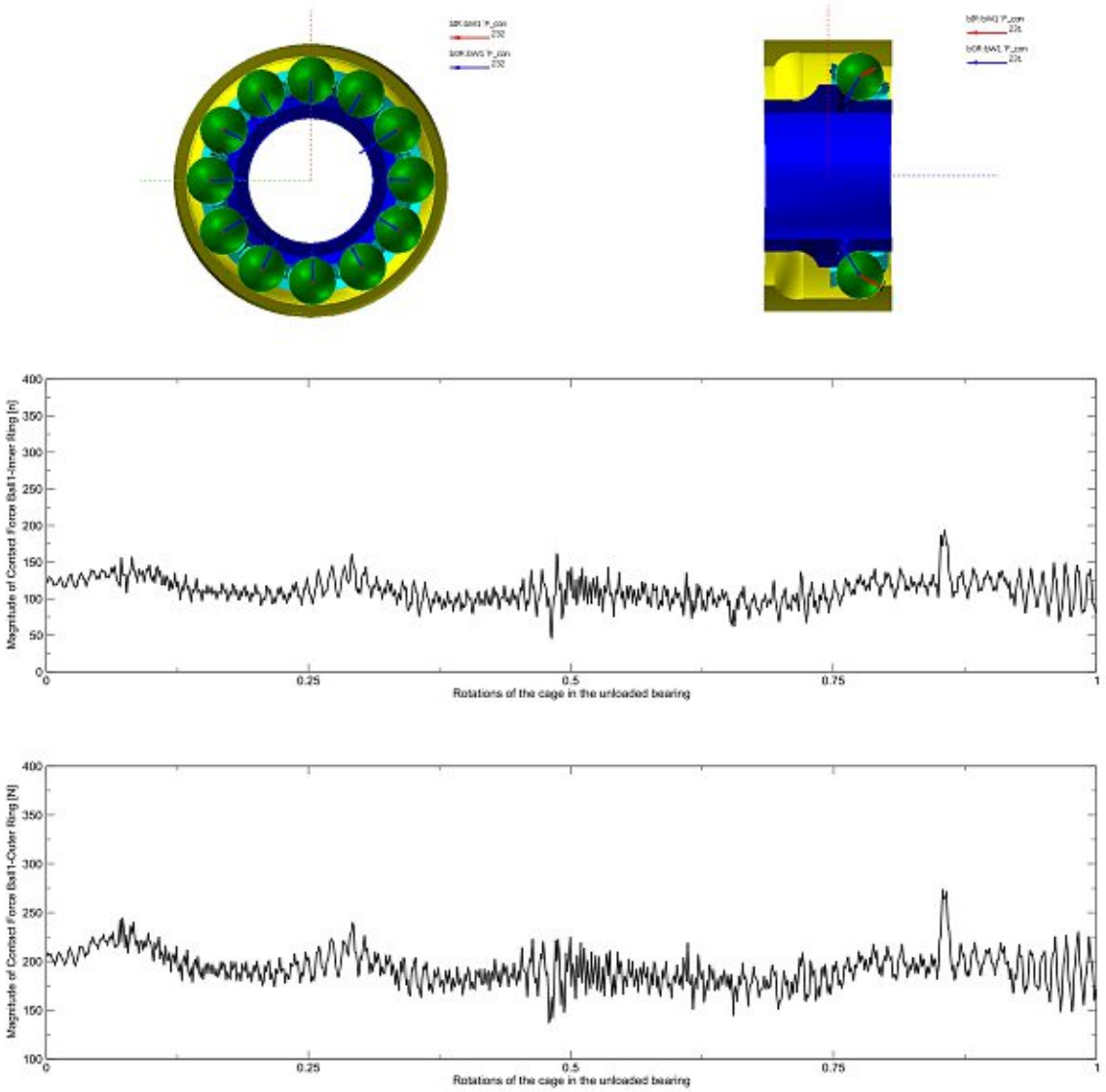

Figure 72: Load distribution in the unloaded bearing

Forces are also acting between the balls and the cage pockets. A period of three cage rotations was investigated in the simulation. According to Figure 73 shock loads appear in the contact zone of the cage pocket of the loaded bearing. The used coordinate system is the global coordinate system. The magnitude of the contact force reaches a maximum

value of 303.42 N and shows a periodic characteristic. During every rotation of the cage the forces appear at the same positions but with slightly different peak values. One can also identify positions in which no force is acting between the cage pocket and ball 1. These are the positions where the cage rotation is between 0.08 - 0.18, 0.26 - 0.44, 0.53 - 0.57 and 0.67 - 0.73.

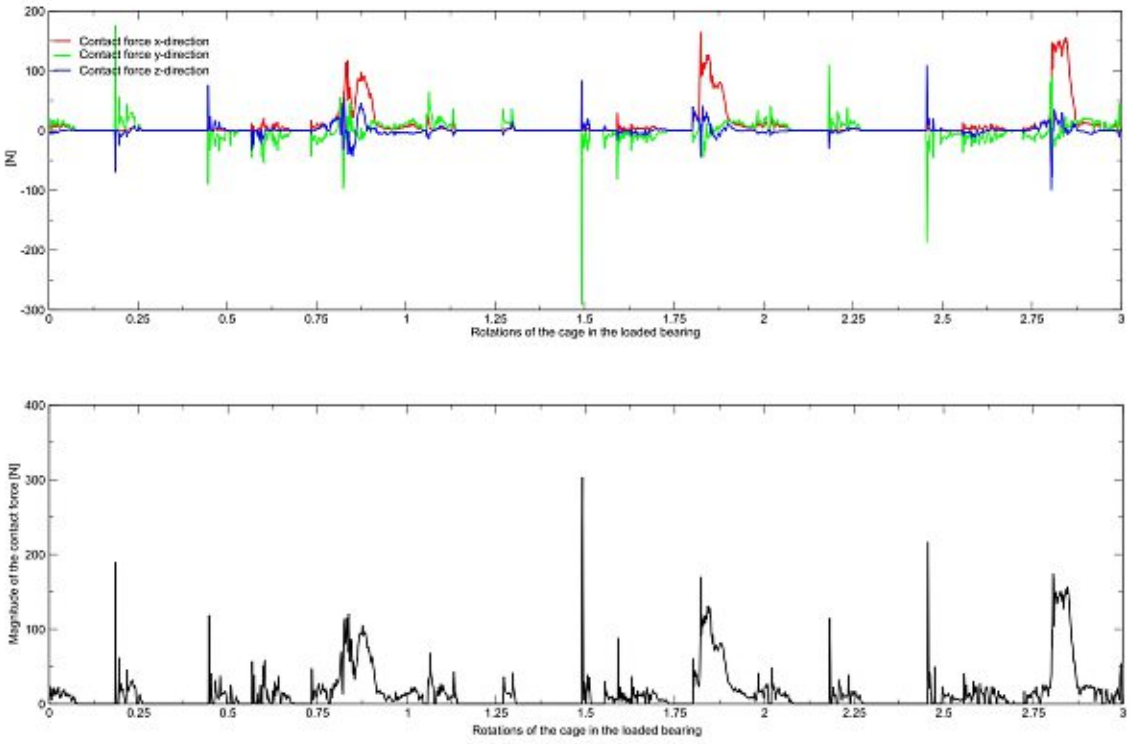

Figure 73: Contact forces in the loaded bearing

The contact forces acting in the cage pocket 1 and caused by the ball 1 in the unloaded bearing are plotted in Figure 74 for all three directions of the global coordinate system. In Figure 75 the magnitude of this contact force is shown. Also in this bearing, the contact force has a periodic characteristic. The maximum value of the magnitude of the contact force is 239.33 N. Cage positions in which no contact forces are acting are 0.14 - 0.28, 0.31 - 0.47, 0.53 - 0.57, 0.69 - 0.71, 0.76 - 0.85 and 0.87 - 0.98.

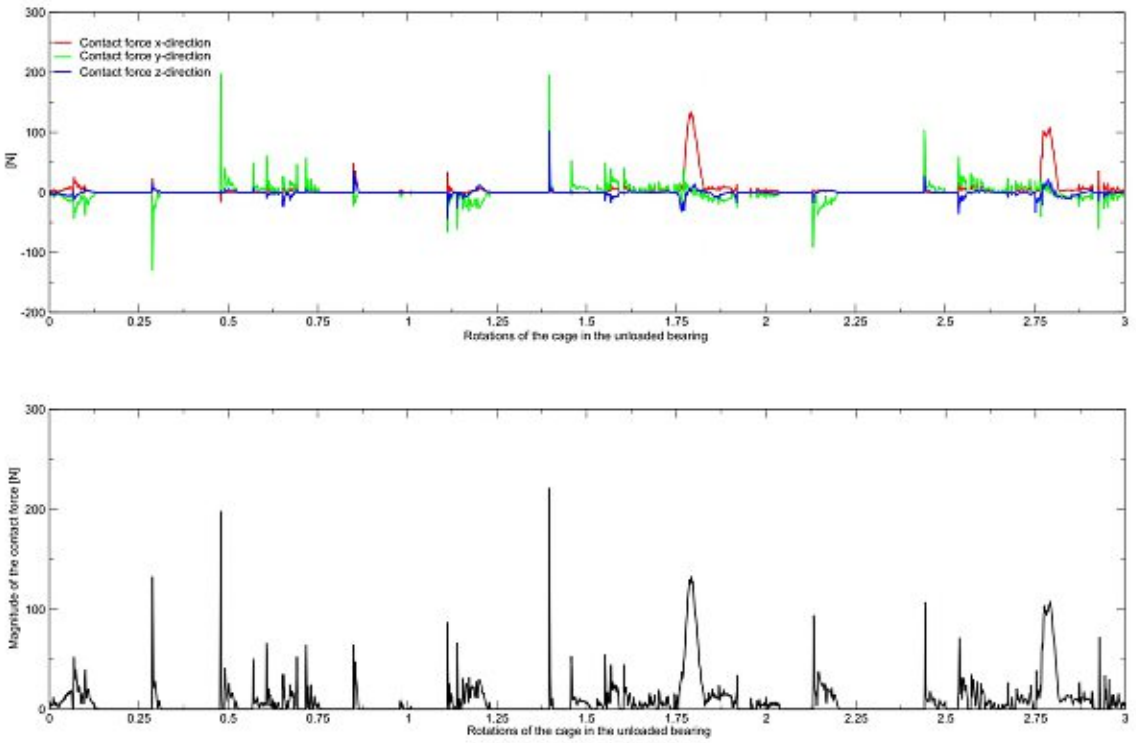

Figure 74: Contact forces in the unloaded bearing

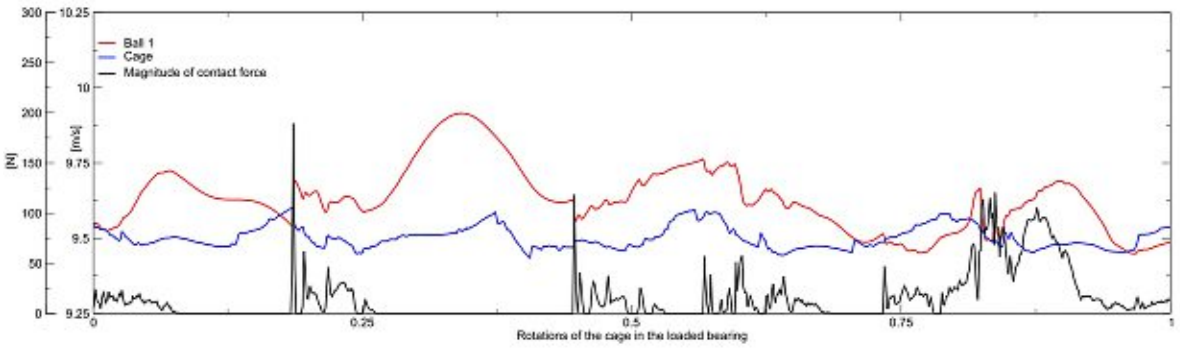

Figure 75: Dynamic situation for the bearing elements ball 1 and cage in the loaded bearing

Finally in Figures 75-76 the correlation of the kinematics and the kinetics of ball 1 and the cage are given. As can be seen, every abrupt change in velocity of the ball is linked with a significant peak of the contact force acting between the ball 1 and the cage pocket 1.

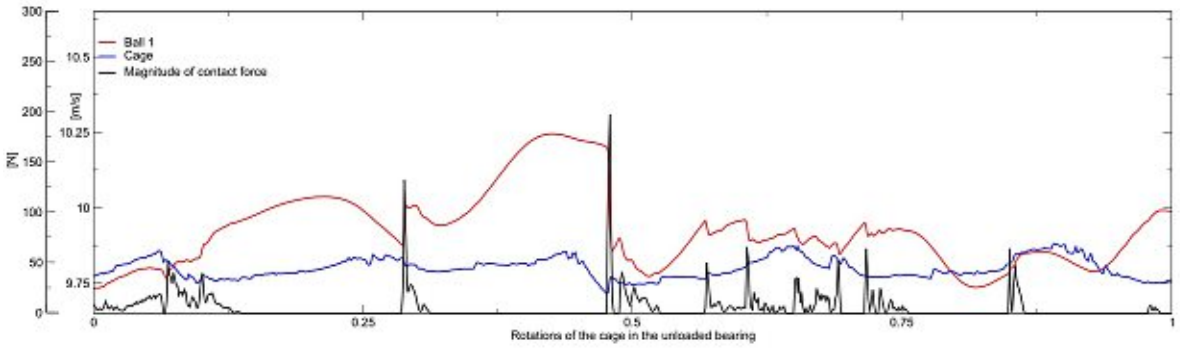

Figure 76: Dynamic situation for the bearing elements ball 1 and cage in the unloaded bearing

5.1.12 Contact pressure

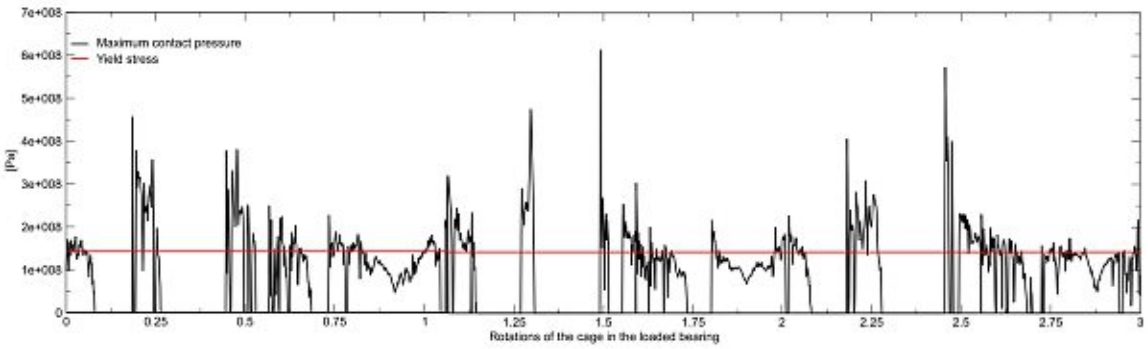

Figure 77: Maximum value of contact pressure due to Hertzian contact in the cage pocket in the loaded bearing

The contact forces cause local pressures in the cage pockets. The maximum magnitude of this contact pressure caused by Hertzian contact between the ball 1 and the cage pocket 1 for the loaded bearing is plotted in Figure 77 and for the unloaded bearing in Figure 78. These plots do not include information about the exact location of the maximum pressure due to Hertzian contact. To identify the location of the maximum pressure, we have to take a look at the structural stresses, which is done in the following section 5.1.13. The local maximum pressure reaches values of around 6e8 Pa in the loaded bearing and 6e8 Pa in the unloaded bearing, which is much higher than the yield stress of the cage material.

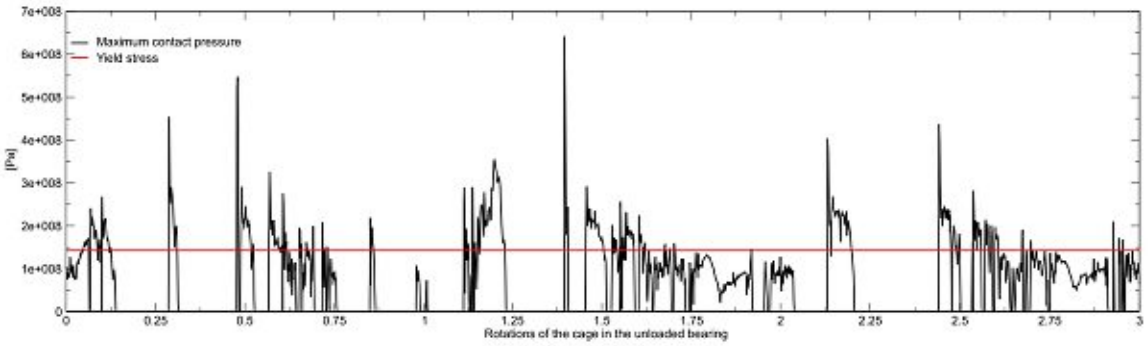

Figure 78: Maximum value of contact pressure due to Hertzian contact in the cage pocket in the unloaded bearing

5.1.13 Structural stresses

For each of the two bearings ten influence radii with a radius of 1 mm were defined to investigate the v. Mises stresses at these positions as a function of the cage rotation. The observation period is three cage rotations. Figure 79 shows the magnitude of the v. Mises stresses at the nodes included in the sphere and located at the surface of the cage for the five influence radii placed at the front side of the cage pocket 1 for the loaded bearing and Figure 80 illustrates the magnitude of the v. Mises stresses at the nodes included in the five influence radii at the back side of cage pocket 2 and located at the surface of the cage. The maximum v. Mises stresses occurring within the simulation at the front side of cage pocket 1 are 1.789e7 Pa at influence radius 1, 1.745e7 Pa at influence radius 2, 2.006e7 Pa at influence radius 3, 1.879e7 Pa at influence radius 4 and 1.438e7 Pa at influence radius 5.

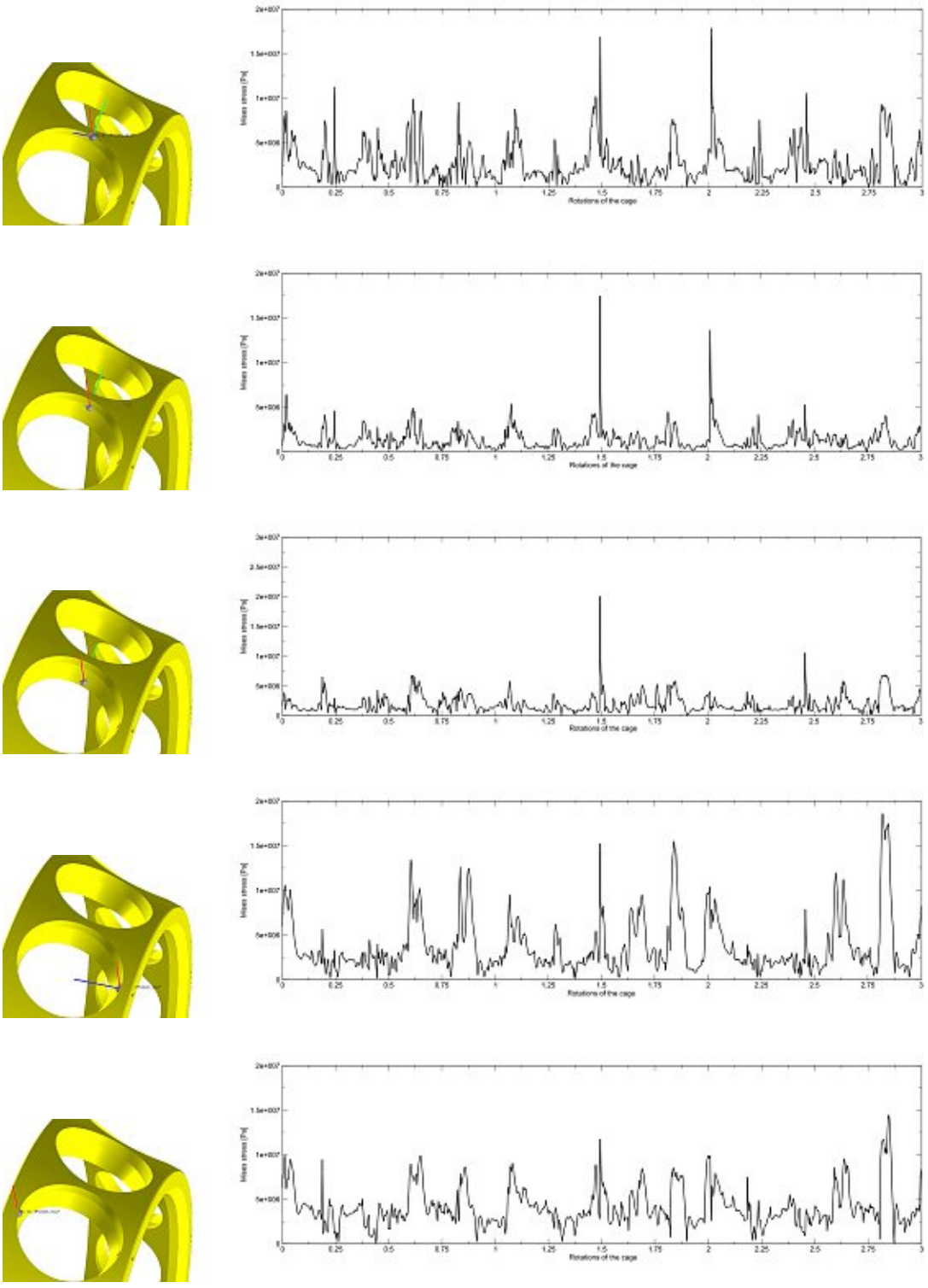

Figure 79: Flexible coordinate systems at the front side of the cage pocket and dedicated v. Mises stresses for the loaded bearing

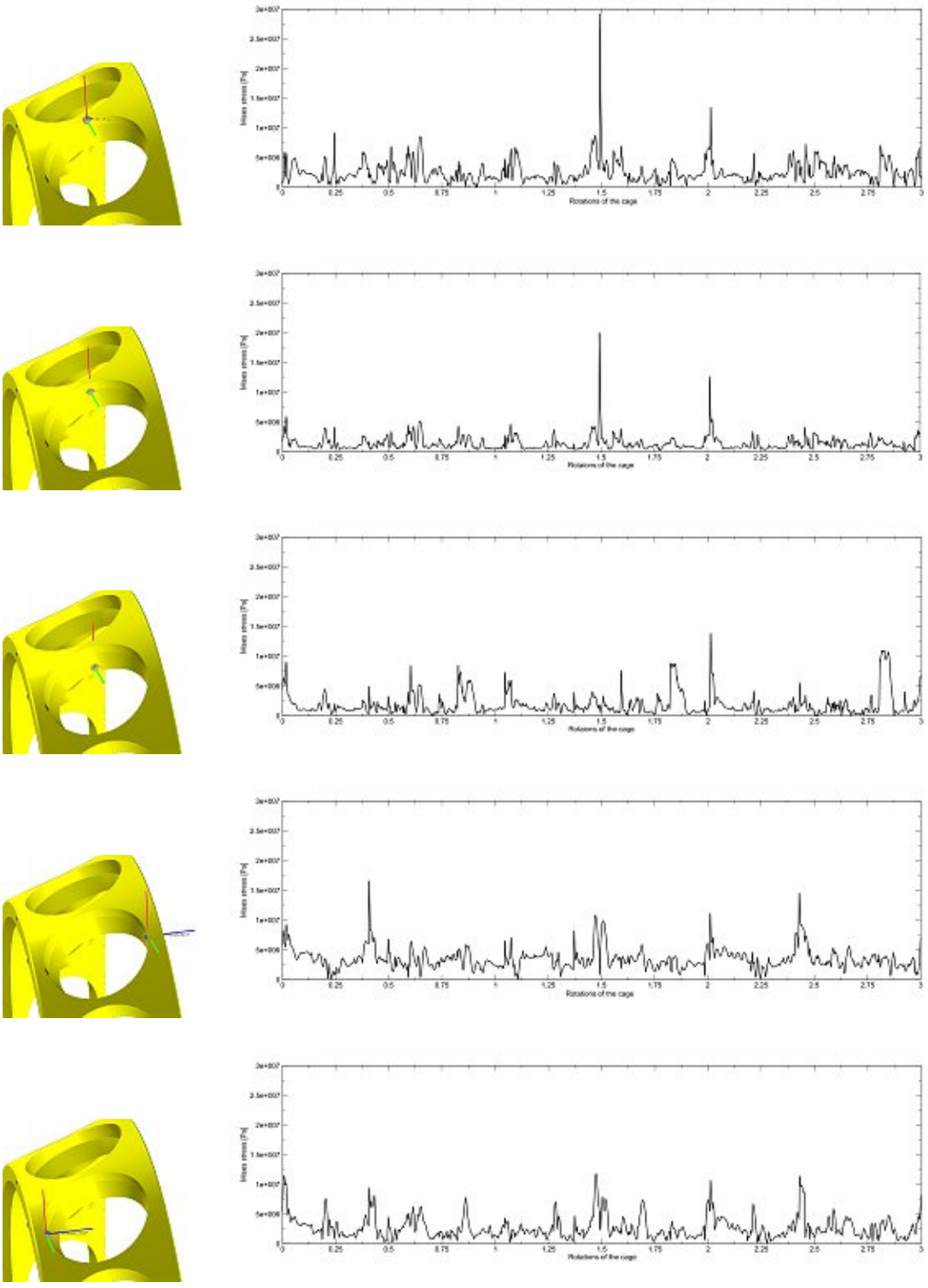

Figure 80: Flexible coordinate systems at the back side of the cage pocket and dedicated v. Mises stresses for the loaded bearing

At the back side of cage pocket 2, the maximum v. Mises stresses at the five investigated spheres are 2.924e7 Pa at influence radius 1, 1.999e7 Pa at influence radius 2, 1.386e7 Pa at influence radius 3, 1.659e7 Pa at influence radius 4 and 1.230e7 Pa at influence radius 5. This means that the overall maximum v. Mises stress occurs at the back side of cage pocket 2 at influence radius 1.

For the unloaded bearing, also five influence radii are placed at the front side of cage pocket 1 and five influence radii are located at the back side of cage pocket 2. Figure 81 shows the magnitude of the v. Mises stresses of the nodes included in the influence radii and located at the surface of the cage. In Figure 82 the magnitude of the v. Mises stresses of the nodes included in the influence radii and on the surface of the cage are shown. The radius used to define the influence radii for this cage is also 1 mm.

The maximum v. Mises stresses occurring within the simulation at the front side of cage pocket 1 are 1.429e7 Pa at influence radius 1, 1.102e7 Pa at influence radius 2, 1.199e7 Pa at influence radius 3, 1.464e7 Pa at influence radius 4 and 1.796e7 Pa at influence radius 5.

At the back side of cage pocket 2, the maximum v. Mises stresses at the five investigated spheres are 2.249e7 Pa at influence radius 1, 1.144e7 Pa at influence radius 2, 2.101e7 Pa at influence radius 3, 1.741e7 Pa at influence radius 4 and 1.687e7 Pa at influence radius 5. This means that the overall maximum v. Mises stress occurs at the back side of cage pocket 2 at influence radius 1.

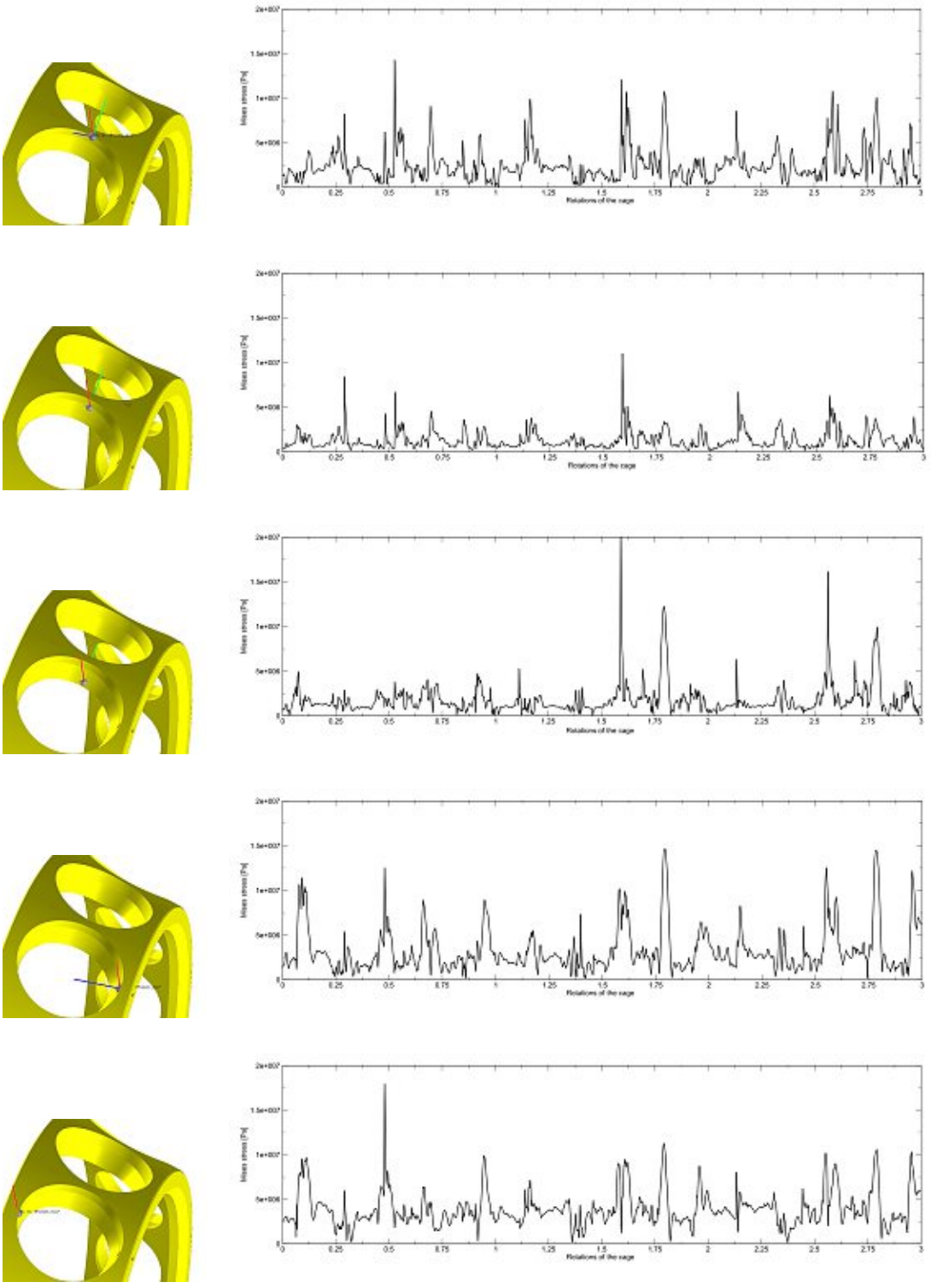

Figure 81: Flexible coordinate systems at the front side of the cage pocket and dedicated v. Mises stresses for the unloaded bearing

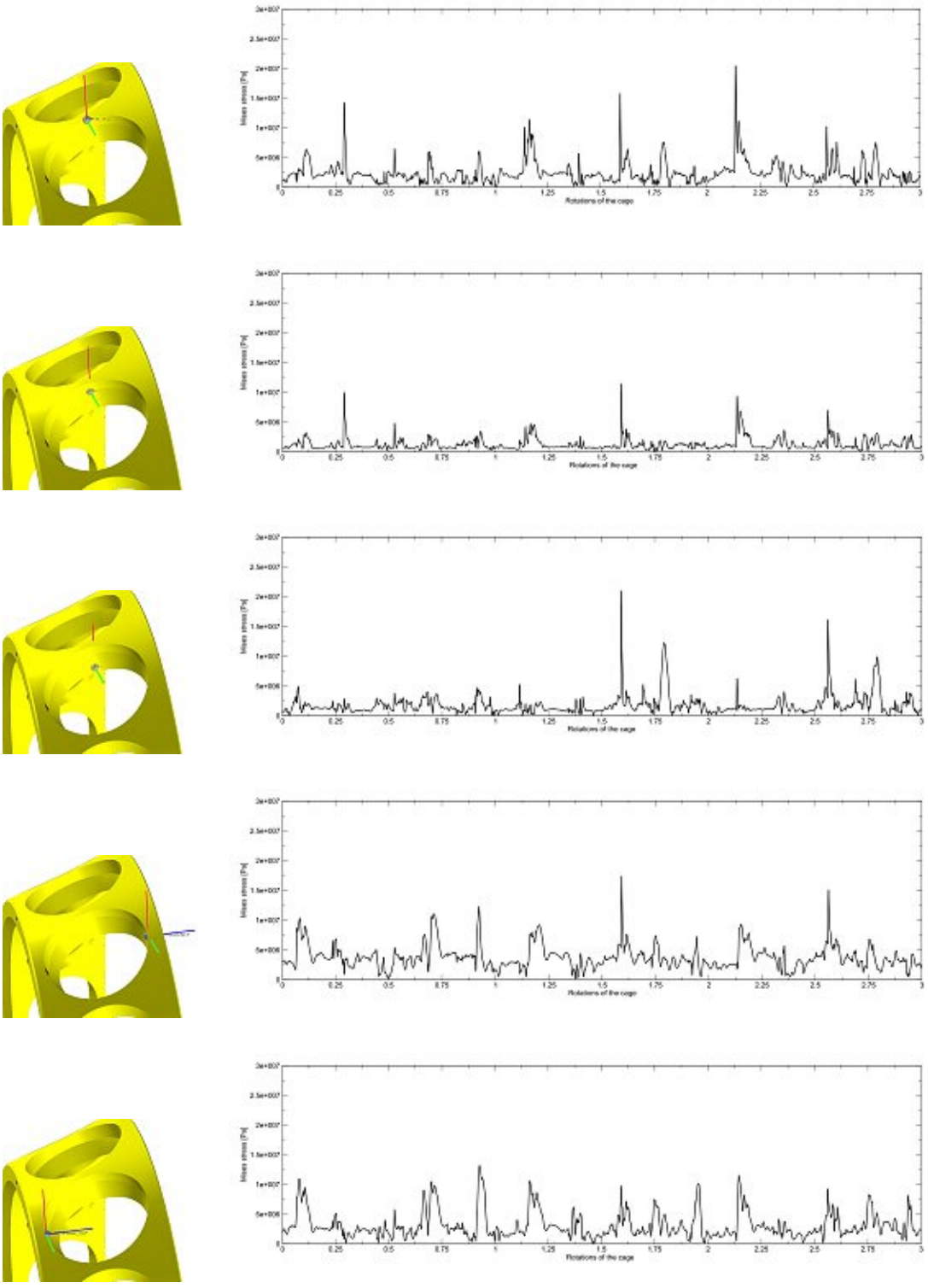

Figure 82: Flexible coordinate systems at the back side of the cage pocket and dedicated v. Mises stresses for the unloaded bearing

5.2 Structural fatigue

Also in this simulation, a fatigue calculation was performed. Five influence radii were placed at the front side of cage pocket 1 at every cage, as shown in Figure 83, since these areas are the critical one. Every influence radius is defined as a sphere with a radius of 0.3 mm.

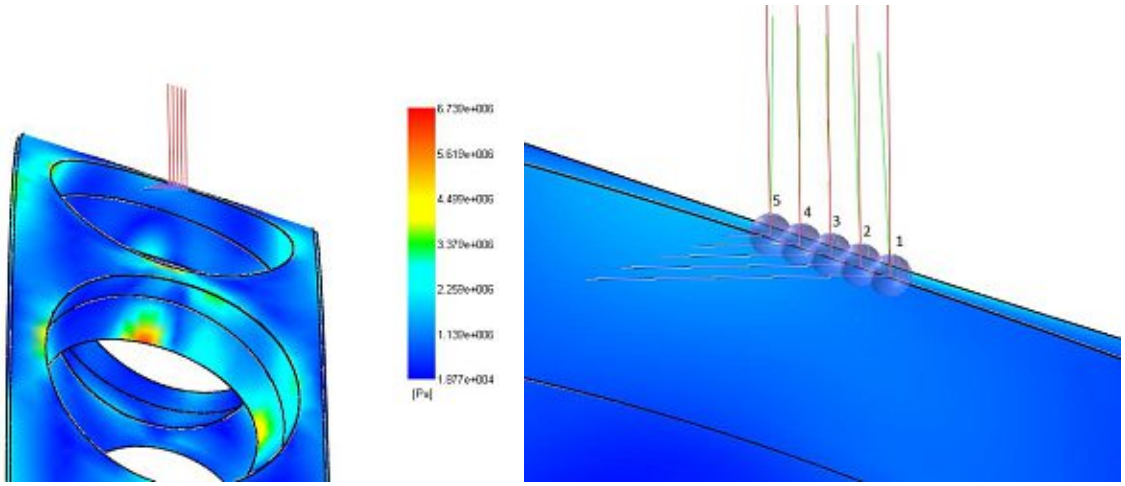

Figure 83: Location of the influence radii with fatigue calculation activated (cage in random position - not the position with extreme stresses)

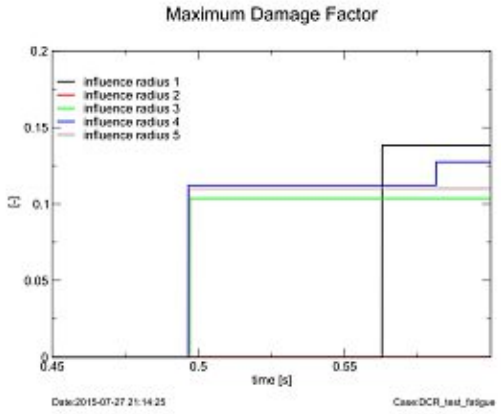

Figure 84: Calculated Maximum Damage Factors in the influence radii of the loaded bearing

The results of the uniaxial fatigue calculation for the cage of the loaded bearing are

given in Figure 84. The used fatigue model does not predict any damage of the cage in the chosen influence radii, since the maximum damage factor never reaches a value bigger than one during simulation time.

Also for the cage of the unloaded bearing, the uniaxial fatigue criteria is not able to predict damage, since the stresses in the influence radii are too low and so the maximum damage factor (Figure 85) also never reaches a value bigger than one, which is the threshold value for fatigue.

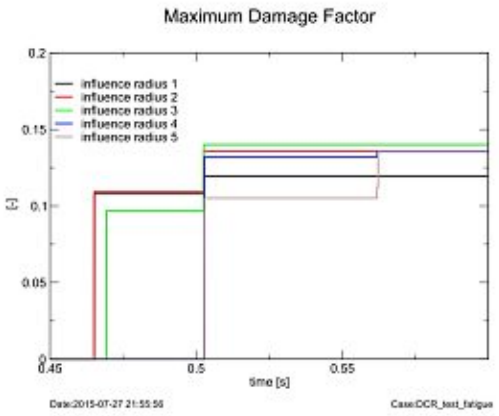

Figure 85: Calculated Maximum Damage Factors in the influence radii of the unloaded bearing

6 CRB - Investigation of a CRB under deceleration

In many cases, the bearing used in an application is not running under stationary conditions. For this reason, an investigation in form of a simulation of a Cylindrical Roller Bearing (CRB) with a simplified machined brass cage under deceleration was done in the virtual test rig BEAST.

6.1 Virtual Test [3]

This section provides information about building a model of the CRB in BEAST and the results of the simulation are presented.

6.1.1 Model building

A model of the SKF Cylindrical Roller Bearing NU 226ECM was built in the preprocessor BEAUTY. The model consists of 20 bodies which are all modeled in form of rigid bodies. The focus in this investigation is set to identify and quantify the occurring forces in the roller bearing, especially the contact forces acting between the rollers and the cage. Since the cage is not modeled as a flexible body, the structural stresses are not investigated in this simulation.

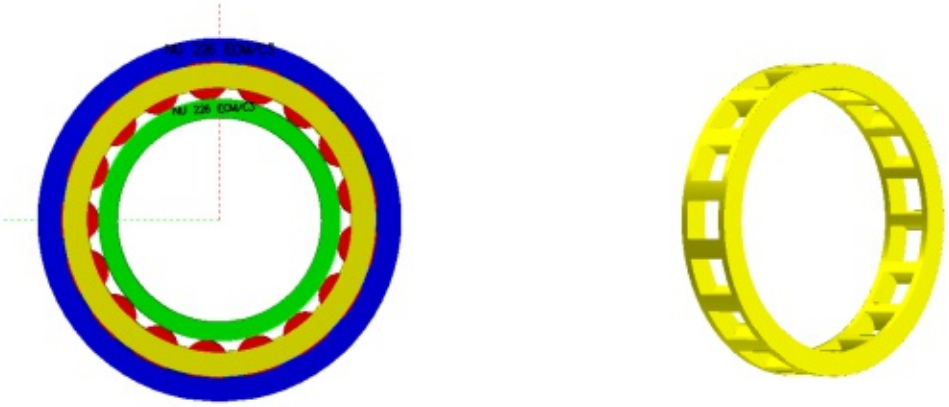

Figure 86: BEAST model of the NU226ECM and the simplified cage

Figure 86 shows the entire model and also the simplified cage used in the simulation. Since the original cage is not included in the BEAST-body library, a user defined cage

was built. The simplification affects the geometry of the cage, but the cage pockets are modeled with the geometry of the real cage. The results of the performed simulation are therefore not accurate but a good estimation of the forces occurring in the real bearing under deceleration.

6.1.2 Material parameters

The rolling elements and the rings are made of steel and the cage is made of brass. The used material parameters are given in Table 4.

6.1.3 Tribology

In this simulation, the pre-defined parameters for surface roughness are used. The surface of the cage pockets are modeled with a surface roughness of 0.1 μm and the initial lubricant layer thickness is 1 μm. All other surfaces of the cage have a surface roughness of also 0.1 μm. The surface of the cylindrical rolling elements and the raceways of the rings are also modeled with a surface roughness of 0.1 μm.

6.1.4 Boundary conditions

In this model, two user defined coordinate systems are included. Since the inner ring is rotating, the ctIR-coordinate system, which is connected with the inner ring is used to apply the rotation. The ctOR-coordinate system, which is connected with the outer ring is fixed in the environment and free of movement. The outer ring is fixed in the environment and therefore not able to move in any direction or rotate around any axis. The inner ring is fixed in the global z-direction and rotations around all three global axis are suppressed. The force acting in the negative x-direction is applied on the inner ring. The matrices describing the boundary conditions are therefore filled with the following stiffness respectively damping parameters:

cB:bIR - SD-tie

- stiffness matrix - relative translation (in [N/m]):

$$\begin{bmatrix} 0 & 0 & 0 \\ 0 & 0 & 0 \\ 0 & 0 & -1e12 \end{bmatrix}$$

- damping matrix - relative translation (in [Ns/m]):

$$\begin{bmatrix} 0 & 0 & 0 \\ 0 & 0 & 0 \\ 0 & 0 & -1e10 \end{bmatrix}$$

- stiffness matrix - relative rotation (in [Nm]):

$$\begin{bmatrix} -1e10 & 0 & 0 \\ 0 & -1e10 & 0 \\ 0 & 0 & -1e10 \end{bmatrix}$$

- damping matrix - relative rotation (in [Nms]):

$$\begin{bmatrix} -1e8 & 0 & 0 \\ 0 & -1e8 & 0 \\ 0 & 0 & -1e8 \end{bmatrix}$$

cB:bOR - SD-tie

- stiffness matrix - relative translation (in [N/m]):

$$\begin{bmatrix} -1e12 & 0 & 0 \\ 0 & -1e12 & 0 \\ 0 & 0 & -1e12 \end{bmatrix}$$

- damping matrix - relative translation (in [Ns/m]):

$$\begin{bmatrix} -1e10 & 0 & 0 \\ 0 & -1e10 & 0 \\ 0 & 0 & -1e10 \end{bmatrix}$$

- stiffness matrix - relative rotation (in [Nm]):

$$\begin{bmatrix} -1e10 & 0 & 0 \\ 0 & -1e10 & 0 \\ 0 & 0 & -1e10 \end{bmatrix}$$

- damping matrix - relative rotation (in [Nms]):

$$\begin{bmatrix} -1e8 & 0 & 0 \\ 0 & -1e8 & 0 \\ 0 & 0 & -1e8 \end{bmatrix}$$

6.1.5 Solver settings

According to the guidelines provided from the BEAST-developer team, the CVODE-solver was used to perform the simulation which only includes rigid bodies.

6.1.6 Results of the simulation

The results of the simulation of the deceleration of the CRB are presented in this section. The investigated time period is 0.074 s. In this period of time, the cage is performing three full rotations. The deceleration (-121.61 rad/s^2) is defined as a slow-down from 258 rad/s to 249 rad/s within 0.074 s (Figure 87).

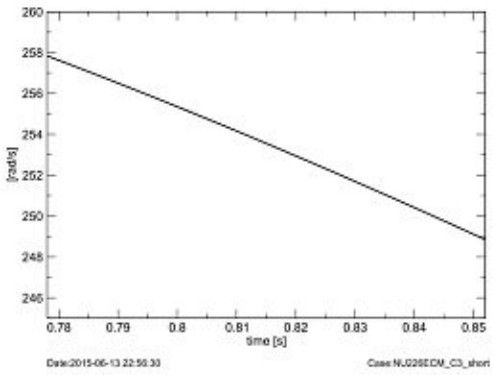

Figure 87: Rotational velocity of the inner ring

The operating conditions (with respect to the global coordinate system) are given in Table 10. The radial load is therefore acting in the negative global x-direction.

Speed	258 rad/s - 249 rad/s
Axial load	0 N
Radial load	-10 000 N

Table 10: Operation conditions for the simulation

6.1.7 Kinematics of the bearing

Movement of the rings

Figure 88 shows the displacement of the geometric center of the inner ring in all three directions of the global coordinate system. The investigated time period is 0.074 s in which the cage performs three full rotations around the global z-axis. In the x and y-directions, the peak to peak value is nearly equal (1.7e-5 m). In the z-direction, the displacement is very small because of the high stiffness in the z-direction of the used cB:bIR - SD-tie.

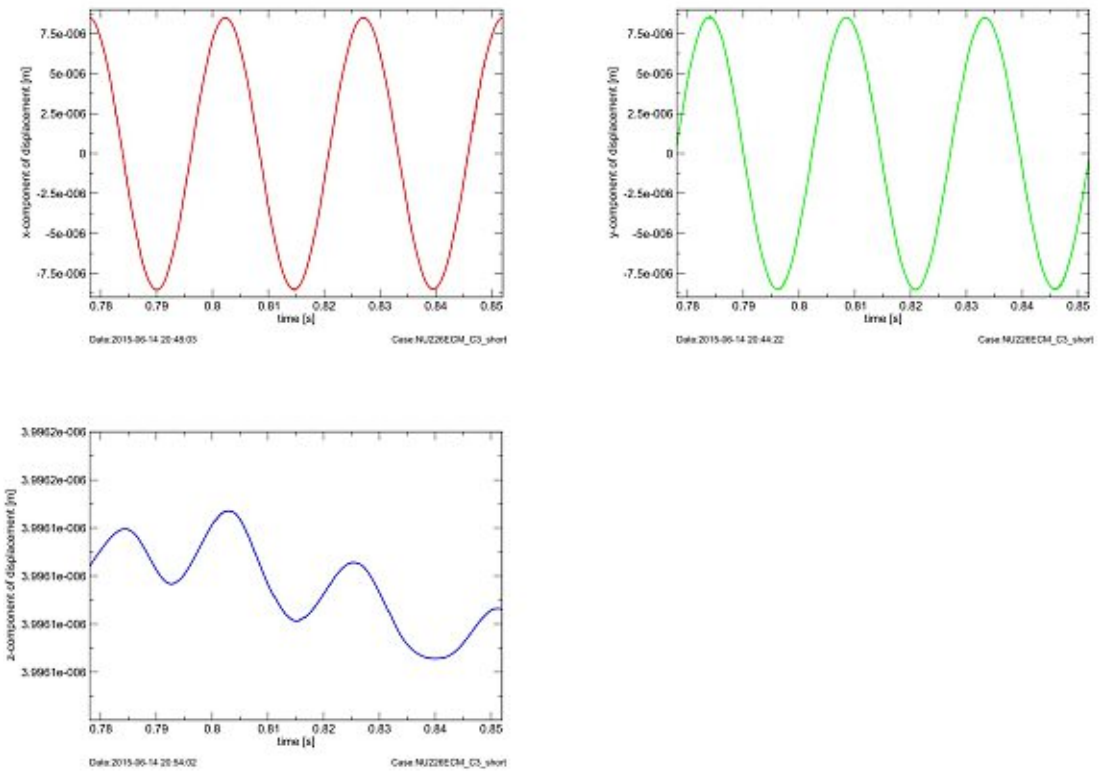

Figure 88: Movement of the geometric center of the inner ring

Movement of the cage

In Figure 89 the displacement of the geometric center of the cage during a time period of 0.074 s, in which the cage rotates three times around its axis, is shown. The displacement in x-direction and y-direction shows the same order of magnitude. In the z-direction, the displacement is very small because of the small relative movement between the inner ring and the outer ring.

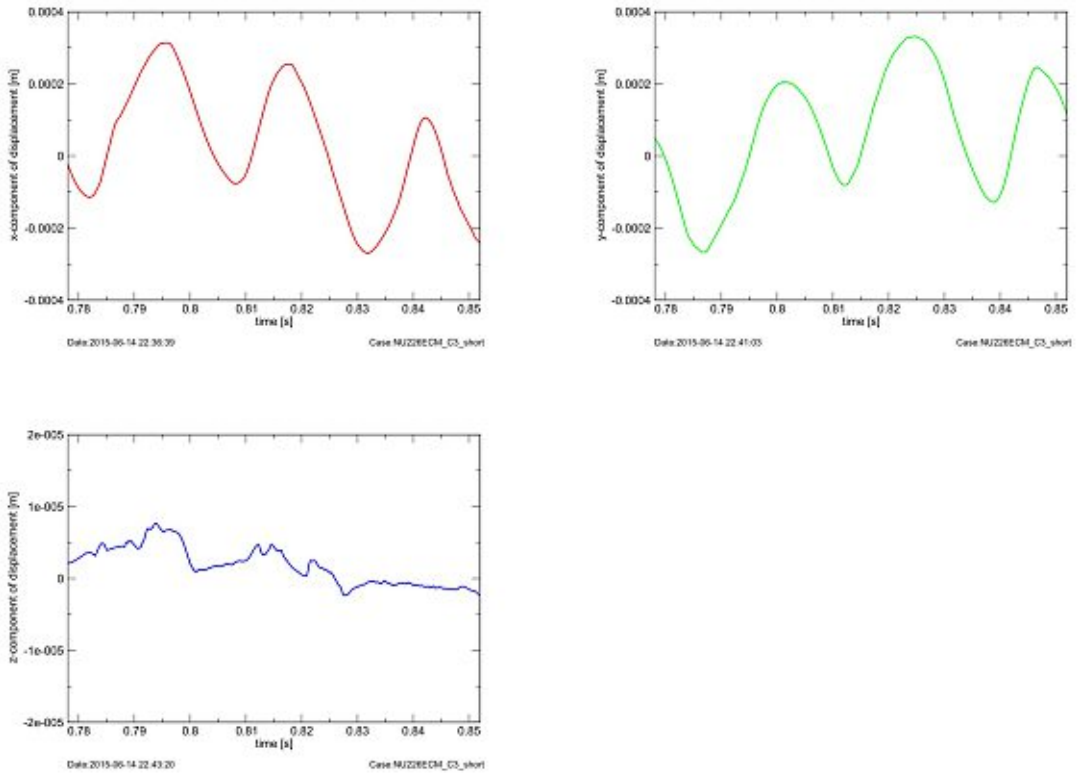

Figure 89: Movement of the geometric center of the cage

The rotational speed of the cage, with respect to the global coordinate system, is given in Figure 90 in form of all three components. One can see, that the rotational speed around the z-axis is decreasing with a deceleration of 44 rad/s^2. It also rotates around the x-axis with a peak-to-peak value of 0.126 rad/s and around the y-axis with a peak-to-peak value of 0.161 rad/s during simulation time.

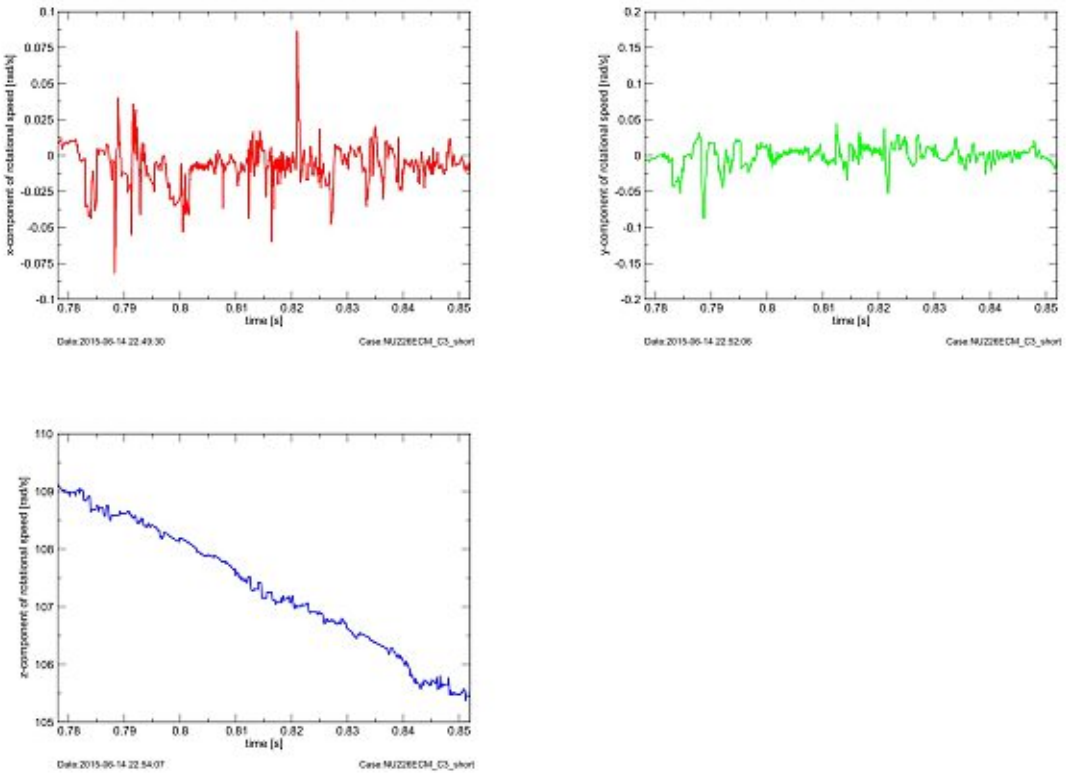

Figure 90: Rotational speed of the cage

Movement of the rolling elements

On the top left side of Figure 91, the velocity of the rolling element 1, which starts from the top position in the bearing, is shown. The deceleration shows constant sections but also abrupt deceleration. The origin of the abrupt chance of velocity is the occurring contact between the rolling element 1 and the cage. On the top right side of Figure 91 the velocity of rolling element 1 and the velocity of the cage is given and on the bottom left side, the velocity of all rolling elements and the cage is shown in one plot. The velocity of the cage is defined as the velocity of a point located at the cage with a radius of 90.75 mm, which is the nominal start position of the rolling elements. The velocity of all the elements is decreasing and within a bandwidth of 1.5 m/s. The abrupt change in velocity of the rolling elements causes the inhomogeneous character of the velocity of the cage.

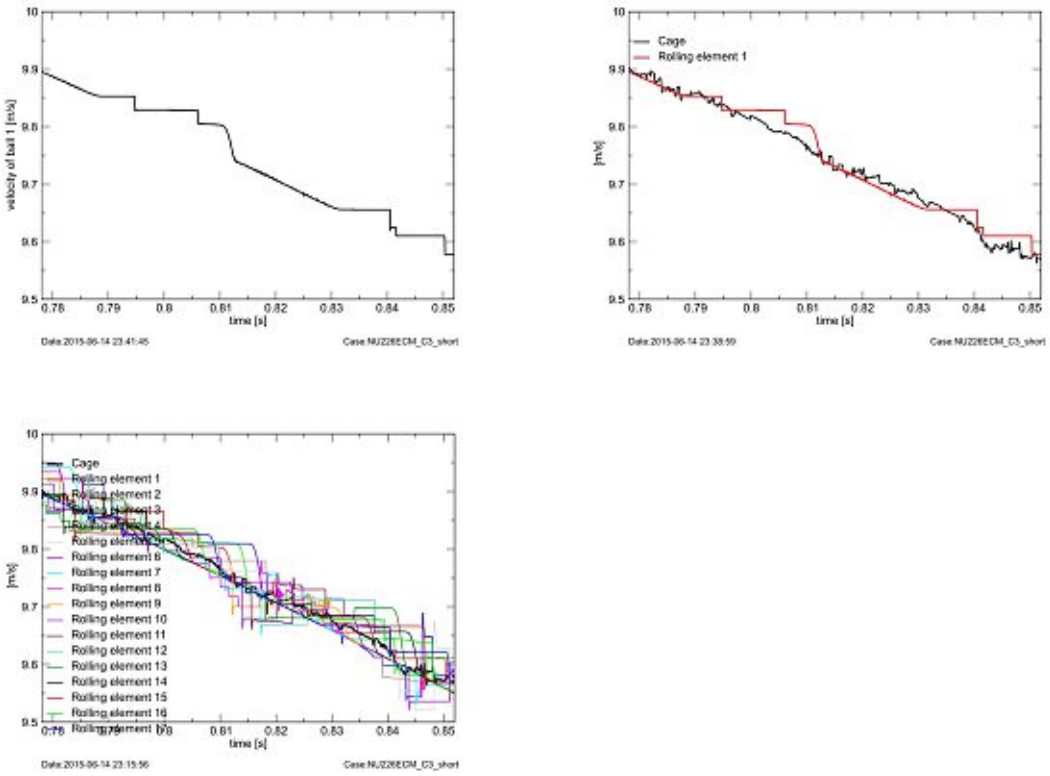

Figure 91: Velocity of the rolling element(s) and velocity of the cage

6.1.8 Contact forces

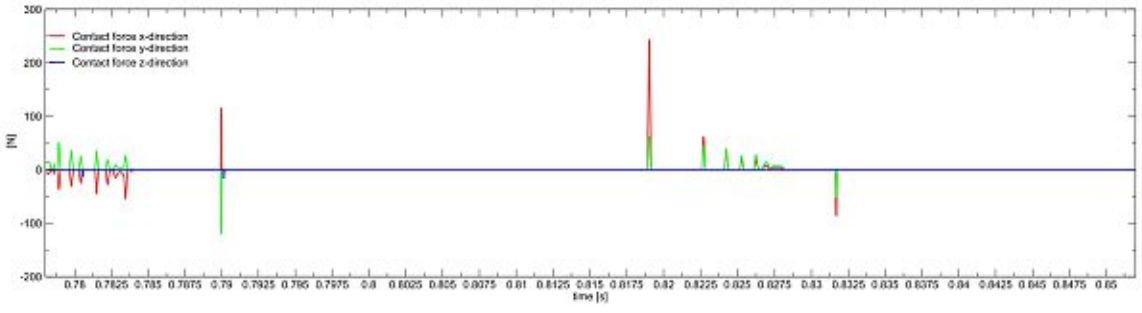

Figure 92: Components of the contact forces in the global coordinate system

The three components of the forces acting between the rolling element 3 and the cage pocket 3 are illustrated in Figure 92. The used coordinate system is the global coordinate system. The maximum value of the force components occurring during simulation time are 243 N in the x-direction, -120 N in the y-direction and -17 N in the z-direction.

Figure 93 shows the magnitude of the contact force acting between rolling element 3 and cage pocket 3. The maximum occurring force during simulation time is 251 N.

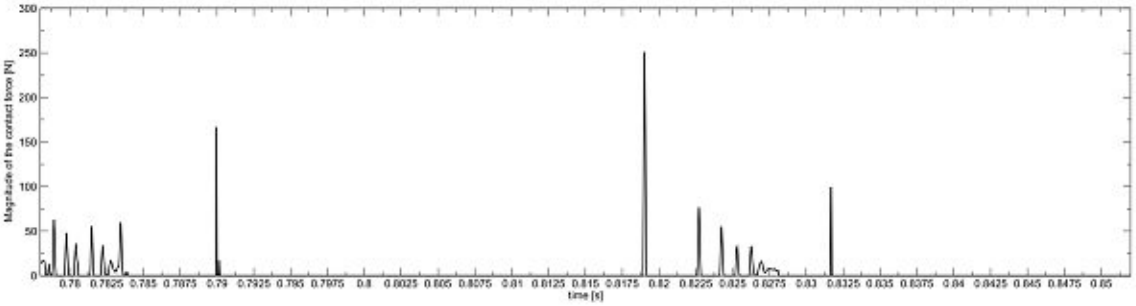

Figure 93: Magnitude of the contact forces in the global coordinate system

6.1.9 Contact pressure

In order to be able to calculate the contact forces given in section 6.1.8, BEAST first calculates the local pressure in the contact zone due to Hertzian contact in the cage pocket. Figure 94 shows the plot of the pressure between the front respectively the back surface of cage pocket 3 and the rolling element 3. It also illustrates the position of the rolling elements within the rolling bearing. At simulation time 0.778 s the rolling element 3 is in the top position.

At the start position at simulation time 0.778 s till 0.784 s, the rolling element 3 is in contact with the back surface of cage pocket 3. During this period of time, the rolling element is accelerated by the cage. At simulation time 0.79 s the rolling element 3 gets in contact with the front side of the cage pocket 3. At this time, the rolling element 3 is at an angular position of 1.43 rad. The next contact occurs at simulation time 0.819 s at an angular position of rolling element 3 of 4.54 rad. At this position, the rolling element 3 gets in contact with the back side of cage pocket 3. Till simulation time 0.828 s, where the rolling element 3 is in an angular position of 5.50 rad, five more peaks of Hertzian pressure occur between the rolling element 3 and the back side of cage pocket 3. The

last contact of the full rotation of the cage occurs at simulation time 0.832 s at an angular position of 5.93 rad of rolling element 3. At this position, the contact is located between the rolling element and the front surface of cage pocket 3. The rolling element is therefore decelerated by the cage.

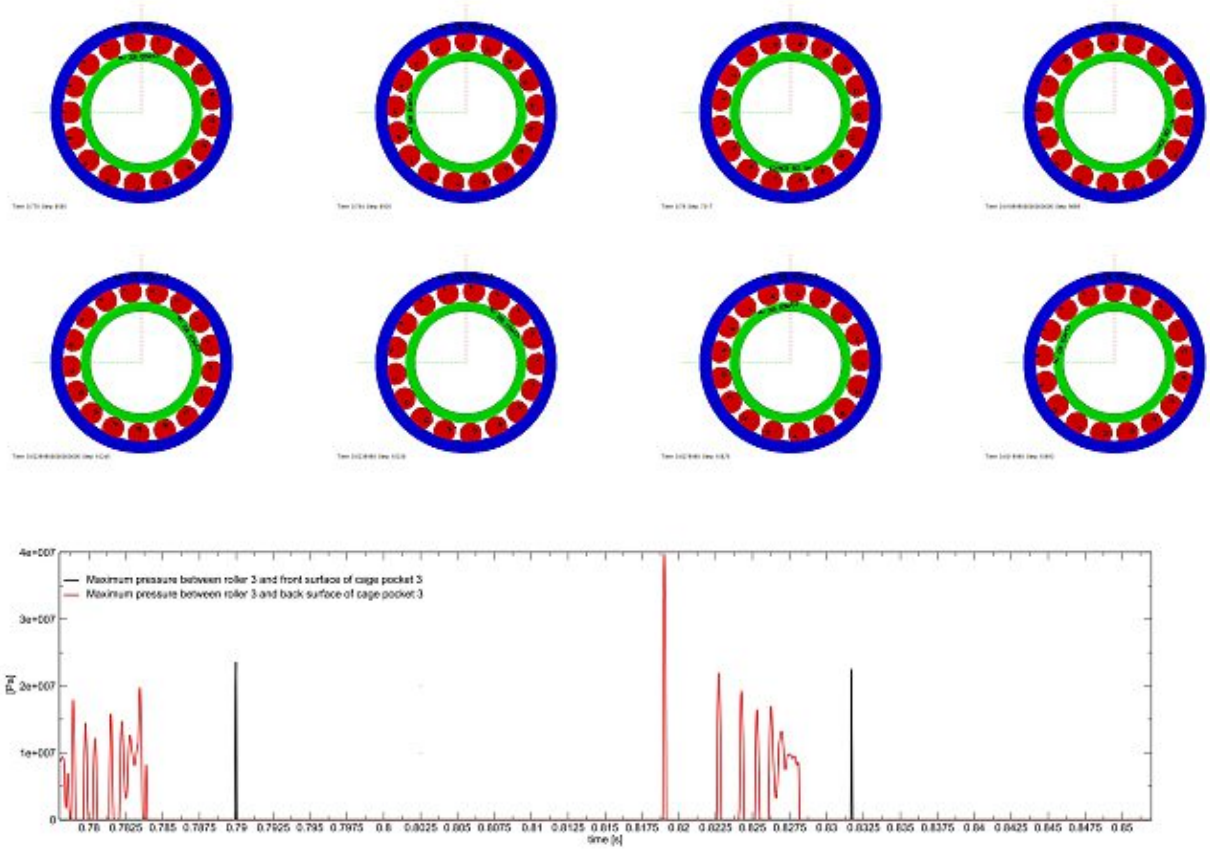

Figure 94: Maximum value of contact pressure due to Hertzian contact in the cage pocket

7 Conclusion

The main goal of this work is to evaluate the practicability of the multi-body-software tool BEAST for daily use by rolling bearings development engineers. The results of the evaluation depends, amongst others, on the complexity of the considered problem and the used model, respectively. The results of the simulations, done in this work, make clear that the used software provides useful results referring to forces (contact forces, forces of inertia, etc..). If elastic bodies are included and these bodies are modeled in a proper way, stresses and deformations are also calculated correctly.

Especially for cages, which are normally not accessible for measuring sensors, dynamic simulations are an obvious method to gather information about the loading of this element of a rolling bearing. In addition to this fact, a simple multi-body-simulation with rigid bodies (section 6) can provide information of occurring forces and the development of them during the revolution of the cage to generate knowledge, which can be used in subsequent FE-calculations.

The virtual test rig BEAST also allows to include flexible calculations (section 3, 5) within the simulation. This kind of simulation requires, of course, the knowledge of more information. Material parameters, surface roughness, residual stresses etc. affect the results, and these input parameters have to be modeled in a proper way to ensure a sufficient accuracy of the results. With the included post-processors the results can be presented either in a simulation video or in form of plots.

Since the calculation is performed using a model of the real system, it is clear, that there are many potential sources of possible model inaccuracies. Ascertained simplification is, for example, that a real mounted bearing is affected by a housing (press fit) and that it is very hard to model this fact in BEAST. An absolute statement has, therefore, to be considered with respect to this, but the tool is suitable for relative comparisons between different designs.

With the simulation of the ACBB - High Speed Test (section 3), the kinematics and dynamics of the bearing are investigated. The vibration of the outer ring and also the vibration of the cage show a periodicity corresponding to the rolling elements within the bearing. The contact forces between the cage pocket and the rolling element also show a periodicity with a maximum contact force of around 600 N and the structural v. Mises stresses in the cage reach a value of 80 MPa.
In the simulation of the ACBB - Dynamic Cage Robustness Test (section 5) the consequence of the different loading conditions of the two bearings is investigated. The cage of the unloaded bearing is rotating slightly faster than the cage of the loaded bearing, as a result of the different contact angles. The contact forces acting between the cage

pocket and the rolling element reach a value of 300 N in the loaded bearing and 230 N in the unloaded bearing. The maximum v. Mises stress in the cage of the loaded bearing, occurring in the simulation, is 29 MPa and 22 MPa in the cage of the unloaded bearing. The simulation of the CRB - Investigation of a CRB under deceleration (section 6) gives an insight in the contact forces acting between a rolling element and a cage pocket, which reach a maximum value of about 250 N. The deceleration of the cage is also identified.

The tested structural fatigue model implemented in BEAST, the uni-axial fatigue model, requires on the one hand a good model of the investigated rolling element bearing and on the other hand also knowledge about the tribology, lubrication method, surface roughness, residual stress and the location of the occurring fatigue, since fatigue can only be calculated in user-defined and small areas (section 4). The results of this work clarify, that the calculated life time of the cage is very sensitive with respect to the input parameters. A parameter study can identify the positive or negative influence of the varied input parameters.

Therefore, the software tool BEAST is a useful tool to gain information about the kinematics and kinetics of the cage and the rolling elements within a rolling element bearing and can help to complement real tests. On the other hand, only short simulation times can be handled, since the data output is very high.

References

[1] DIN ISO 281 Wälzlager - Dynamische Tragzahlen und nominelle Lebensdauer (ISO 281:2007)

[2] Rolling bearings, PUB BU/P1 10000/2 EN, SKF Group, August 2013

[3] Steven E. Boer (editor): BEAST, BEAring Simulation Tool, 12.0, Users Manual, December 18, 2014

[4] Albert Mathias, Köttritsch Hubert: Wälzlager - Theorie und Praxis. Springer-Verlag, Wien, 1987

[5] Iakov Nakhimovski, Dag Fritzson: Modeling and Simulation of Contacting Flexible Bodies in Multibody Systems, Report GE02F058, SKF Group Manufacturing Development Centre, November 19, 2002

[6] Dag Fritzson, Mikael Holgerson: The new RunEHL BEAST contact model, Report GE01F021, SKF Group Manufacturing Development Centre, 2001-11-29

[7] Lars-Erik Stacke, Dag Fritzson: Forces in Lubricated Contacts - Model and Cage Pocket Verification, Report NL92D017, SKF Engineering Research Centre B.V., December 17, 1992

[8] Harold Elshof, Lars-Erik Stacke: EHL calculations for BEAST, Report NL96D006, SKF Engineering Research Centre B.V., July 30, 1996

[9] C.H. Venner: Multilevel Solution of the EHL Line and Point Contact Problems. PhD thesis, Universiteit Twente, The Netherlands, 1987

[10] Marcus Edstorp: BEAST Structural Stress Modeling and Verification, Report NL12D002, SKF Engineering Research Centre, Gothenburg, 2013

[11] Kersten Hahn: Dynamik Simulation von Wälzlagerkäfigen, Shaker Verlag GmbH, Aachen 2005

[12] Iakov Nakhimovski, Pietro Tesini: Cage Fatigue Indicators in BEAST - Phase II, Report NL11D003, SKF Engineering Research Centre, 2011-6-29

[13] CS-7313 EM Brass material performance evaluation, Test Report, SKF Test Centre Steyr, July 3, 2013

[14] Roman Teutsch: Kontaktmodelle und Strategien zur Simulation von Wälzlagern und Wälzführungen, Maschinenelemente und Getriebetechnik Berichte, Band 01/2005, Herausgeber: Prof. Dr.-Ing. Bernd Sauer, Technische Universität Kaiserlautern

[15] Raymond A. Guyer, Jr.:Rolling Bearings Handbook and Troubleshooting Guide, Chilton Book Company, 1996

[16] Eschmann, Hasbargen, Weigand: Die Wälzlagerpraxis - Handbuch für die Berechnung und Gestaltung von Lagerungen, R. Oldenbourg Verlag München Wien, 1978